

Hydrogen particle and plasma interactions with heterogeneous structures

Alexey Kuznetsov

PhD committee

Chair:

prof.dr. G. van der Steenhoven

University of Twente, TNW

Secretary:

prof.dr. G. van der Steenhoven

University of Twente, TNW

Promoter:

prof.dr. F. Bijkerk

University of Twente, TNW
FOM Institute DIFFER

Referee:

prof.dr. V.Y. Banine

ASML
Technical University of Eindhoven

Committee members:

prof.dr.ir. J.W.M. Hilgenkamp

University of Twente, TNW

prof.dr.ir. H.J.W. Zandvliet

University of Twente, TNW

prof.dr.ing. A.J.H.M. Rijnders

University of Twente, TNW

prof.dr. R.E.I. Schropp

ECN
Technical University of Eindhoven

The work described in this thesis is a part of the FOM Industrial Partnership Programmes I10 ('XMO') and I23 ('CP3E') which have been carried out under contract with Carl Zeiss SMT GmbH, Oberkochen, and ASML, Veldhoven, and the 'Stichting voor Fundamenteel Onderzoek der Materie (FOM)', the latter being financially supported by the 'Nederlandse Organisatie voor Wetenschappelijk Onderzoek (NWO)'. Agentchap NL is acknowledged for the support of EXEPT programme in the frame of the 'Internationale Samenwerkingsprogramma's'.



Cover: SEM image of hydrogen-induced blisters on Mo/Si multilayer mirror

Printed by Ipskamp Drukkers, 2013

**HYDROGEN PARTICLE AND PLASMA INTERACTIONS WITH
HETEROGENEOUS STRUCTURES**

PROEFSCHRIFT

ter verkrijging van
de graad van doctor aan de Universiteit Twente,
op gezag van de rector magnificus,
prof. dr. H. Brinksma
volgens besluit van het College voor Promoties
in het openbaar te verdedigen
op vrijdag 18 oktober, om 12:45 uur

door

Alexey Sergeevich Kuznetsov

Geboren op 23 augustus 1985

te Moskou, Rusland

Dit proefschrift is goedgekeurd door de promotor:
Prof. Dr. F. Bijkerk

ISBN: 978-90-9027806-3
© Alexey Kuznetsov, 2013

Contents

1. Introduction.....	7
1.1 Hydrogen interaction with materials.....	7
1.2 Motivation.....	8
1.3 Processes of blister formation	12
1.4 Hydrogen-induced effects in composite structures	15
1.4.1 Noble gas ion exposures of ML structures	17
1.4.2 Hydrogen ion exposures of ML structures	17
1.4.3 Hydrogen incorporation in ML structures during sample deposition.....	17
1.4.4 Annealing of H-containing ML and multicomponent structures.....	18
1.4.5 H-induced modification of ML magnetic properties.....	18
1.5 Laser plasma-wall interactions	19
1.6 The contribution of this thesis.....	20
2. Experimental	23
2.1 ML sample deposition.....	23
2.2 Hydrogen exposures of ML samples.....	23
2.3 Analysis of hydrogen content	26
2.3.1 Elastic Recoil Detection.....	26
2.3.2 Nuclear Reaction Analysis.....	26
2.3.3 Rutherford Backscattering Spectroscopy	28
2.4 Analysis of blisters by microscopy techniques.....	28
3. Initial studies of hydrogen interaction with thin film multilayered structures... 31	
3.1 Introduction.....	32
3.2 Experimental	33
3.3 Results and discussion	34
3.3.1 Exposures to low-energy plasma.....	34
3.3.2 Initial observations of blistering.....	37
3.3.3 Influence of substrate temperature	37
3.3.4 Deuterium exposures.....	39
3.3.5 Influence of total fluence	40
3.4 Conclusions.....	43
4. Hydrogen-induced blistering mechanisms in thin film coatings..... 45	
4.1 Introduction.....	46
4.2 Experimental	47
4.3 Results.....	47
4.4 Discussion.....	53
4.5 Conclusions.....	55
5. Hydrogen-induced blistering in Mo/Si multilayers: uptake and distribution 57	
5.1 Introduction.....	58
5.2 Experimental	59
5.3 Results.....	60
5.4 Discussion.....	67
5.4.1 Native hydrogen in MLs	67
5.4.2 Hydrogen uptake and distribution	68
5.4.3 Blister development	71

5.4.4 Blistering mechanisms	72
5.4.5 Effect of extended exposure.....	73
5.5 Conclusions.....	74
6. Ion effects in hydrogen-induced blistering of Mo/Si multilayers.....	77
6.1 Introduction	78
6.2 Experimental.....	81
6.3 Results.....	82
6.3.1 Ion flux profiles	82
6.3.2 Blister formation during ion+neutral exposures	83
6.3.3 “Ion+neutral” versus “neutral only” exposures	87
6.3.4 H-content and depth profile	90
6.4 Discussion	91
5.5 Conclusions.....	98
7. Temperature dependence of hydrogen-induced blistering of multilayer thin films.....	99
7.1 Introduction	100
7.2 Experimental.....	100
7.3 Results.....	101
7.3.1 Exposures to H radicals and mixture of radicals and ions at different temperatures	101
7.3.2 Effects of pre- and post-exposure annealing.....	106
7.4 Discussion	107
7.4.1 Influence of ions on blister formation.....	108
7.4.2 Thermally-induced effects	110
7.4.3 Processes of blister formation.....	112
7.5 Conclusions.....	115
8. Spectral and spatial structure of XUV radiation in a laser plasma-wall interaction.....	117
8.1 Introduction	118
8.2 Experimental.....	119
8.3 Results and Discussion.....	121
8.4 Conclusions.....	127
9. Valorization.....	129
9.1 Scientific environment.....	129
9.2 Suppression of blistering in multilayered structures.....	130
9.3 Enhanced H retention properties in multilayered structures	132
9.4 Laser plasma-wall interactions.....	133
9.5 Outlook	134
10. Summary	137
11. Samenvatting.....	139
12. List of publications	141
12. Bibliography.....	143
13. Acknowledgments.....	155
14. Curriculum Vitae.....	157

1. Introduction

1.1 Hydrogen interaction with materials.

Hydrogen is the most abundant element in the known universe. In a sense, life on the Earth is also based on hydrogen, being one of the components of protein molecules. Conversely, hydrogen is able to destroy any life when it is placed in the heart of a thermonuclear bomb. This dual nature of hydrogen can be also seen in it being the first element and the lightest in the periodic table, studied for many years, but still triggering numerous scientific questions.

Processes of hydrogen interaction with solids draw attention of researchers in many fields of investigation. ITER, the International Thermonuclear Experimental Reactor, serves as an example of a complicated experimental device where interaction of hydrogen isotopes (deuterium, tritium) with the wall materials is of paramount importance. In ITER and other fusion devices plasma interaction with the walls has negative consequences as it causes their degradation due to, for instance, physical and chemical sputtering [1-6], blistering (formation of voids beneath the material surface) [7-10], melting and cracking [11-14] and other types of surface modifications.

As a consequence of plasma-wall interaction, wall materials can reach the core of the hot fusion plasma thereby leading to a drop in plasma temperature [15] by means of energy losses via radiation. Another issue is fuel trapping in the first wall materials [16-20] and the formation of redeposited films [21-23]. As radioactive species (tritium) are used as a reaction material, their retention in the wall affects fuel requirements and imposes safety issues [24] which limit the lifetime of a thermonuclear reactor.

At present, there is still a lack of comprehensive understanding of the hydrogen-induced processes of surface modification and material deterioration in fusion devices, and this complicates the choice and development of first wall materials suitable for a thermonuclear reactor.

The newest areas of studies of hydrogen interaction with materials are related to hydrogen interacting with novel, predominantly micro- and nanoscale materials and structures. In this case, pre-existing knowledge (e.g. from fusion research) which is based on bulk material properties might be inadequate to describe the processes governing hydrogen behaviour in those materials. Development of solid state hydrogen storage and (photo-) catalytical nanomaterials and

structures [25-31] indicates that the behaviour of hydrogen can be influenced by material properties on the nano-level.

A novel approach to produce thin silicon wafers by means of slicing the Si by hydrogen localization at depth, a layer splitting process for Si-on-insulator technology, was developed involving the control of crack formation by nanometer thick strained layers [32, 33]. Studies and implementation of thin film-based switchable mirrors [34-36] which change their optical properties due to hydrogen uptake and development of solar cell components [37-39] are among the other examples where hydrogen interaction with materials at micro- and nanoscale is of high importance. As those examples represent new, emerging and dynamic research fields, more insights is needed to understand interaction of hydrogen with nanoscale materials. Mechanisms of hydrogen interaction with heterogeneous nanostructured materials at the atomic scale, role of the materials properties at nano-level, (synergetic) effects of various hydrogen species (atoms, molecules, ions of different energies) are examples where there is still a lack of knowledge of fundamental processes and, as a consequence, uncertainty in the ability to control them in case of applications of such systems in hydrogen-containing media.

1.2. Motivation

The main contribution of this thesis is in the new insights it provides on how hydrogen interacts with thin film multilayered (ML) structures and the consequences of such interaction. The initial motivation of the investigation came from the fact that Mo/Si MLs are used as reflective optical elements for Extreme Ultraviolet (EUV) lithography tools with a wavelength of 13.5 nm [40]. This technique is the most promising form of photolithography for production of integrated circuits (IC) [41]. An element of such multilayer optics typically consists of about 50 Mo/Si bilayers, with nanometer thickness of the individual layers. It works on the principle of constructive interference. A cross-sectional transmission electron microscopy (TEM) image of a representative EUV mirror is presented in figure 1.1.

High demands on the quality of mirrors can be routinely fulfilled [42, 43] nowadays, and there are already first production EUV machines developed by ASML, producer of semiconductor manufacturing equipment. The EUV optics used in such apparatus, has been developed by Carl Zeiss SMT GmbH, a renowned expert in the production of various optical systems and elements. The most advanced up-to-date EUV lithography machines of ASML are being prepared to be shipped to customers who are planning to start actual use of EUV as early as 2013 in pre-production schemes [44].

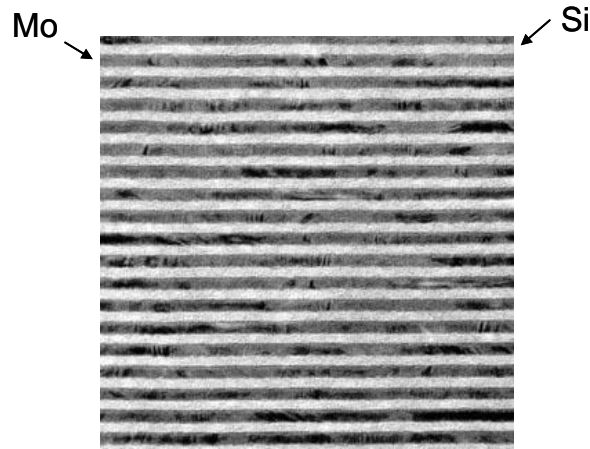


Figure 1.1: Cross-sectional TEM image of a Mo/Si EUV mirror.

However, a great deal of effort is being expended to further increasing the performance of such tools, for instance by providing extended lifetime of multilayer optics. The enormous interest of semiconductor industry in ensuring that EUV lithography tools achieve even higher levels of performance, is evident from recent investments by Intel, TSMC and Samsung in ASML's research and development program [45].

The goal of EUV lithography usage for mass manufacturing puts high demands on the source of EUV irradiation used in the tool in terms of the EUV source power [46]. From the spectrum of solutions available [47, 48], a most promising candidate for commercial production tools is a tin-based laser produced plasma (LPP) EUV source, for which power values as high as ~50 W of EUV power in the intermediate focus have been reported [49]. A principle scheme of such source is presented in figure 2. EUV irradiation (among other wavelengths) is emitted by the LPP created from tin droplets irradiated by a high-power CO₂ laser [50].

The usage of tin LPPs may have side effects. Tin particles with energies starting from thermal and up to the keV range can be emitted from the source [51, 52] and, as a consequence, may potentially damage or contaminate the surface of the EUV collecting optics. The collector optic is the first mirror in the EUV lithography equipment which serves for collecting the EUV light from the source and transporting it further. Damage by energetic and thermal particles can lead to deterioration of the optical performance of the collector mirror [53, 54]. In order to mitigate those negative effects, a scheme was proposed where hydrogen can be used as a buffer gas to stop Sn debris from reaching the collector optics [55].

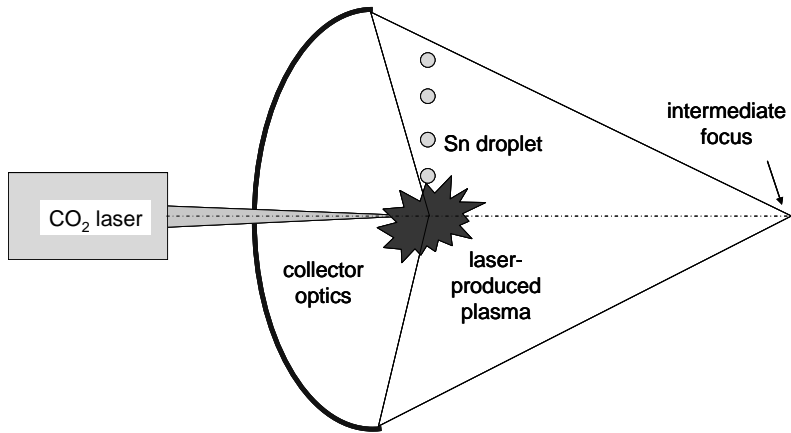


Figure 1.2: Scheme of an LPP-based EUV source.

However, experience with other mitigation schemes proposed, based on noble gas, suggests that hydrogen can be ionized by EUV photons and a parasitic, low-energy ‘secondary’ plasma might be formed near the collector surface [56-58]. Sputtering and blistering by plasma ions was observed during exposures of Mo/Si ML mirrors to high-energy noble gas ions [59, 60]. It is necessary to study what kind of effects might occur under exposure to EUV-induced hydrogen plasma.

EUV-induced photochemistry leading to processes of carbon contamination growth [61-64], top layer oxidation [65, 66]; diffusion, interlayer formation, crystallite growth and intermixing caused by thermal loads [67-70] are among the critical processes which might occur at the surface of EUV optics during exposures to high-power EUV sources. Advanced EUV mirrors may have a capping layer to protect the top surface [71-73] or barrier layers serving to mitigate temperature-induced changes in the ML structure [74-76]. However, those protective layers and barriers might also be influenced or damaged by hydrogen species. Such processes are schematically illustrated in figure 1.3. This applied research area contains much fundamental science. For example, apart from the interaction of hydrogen with multilayered structures itself, there is still a lack of understanding about sputtering of relevant materials in the low-energy (near threshold) regime [77] or about the fundamental details of the interlayer formation in thin film ML structures [78].

On the other hand, the use of hydrogen could be beneficial. Hydrogen radicals and plasmas were proposed as cleaning agents to remove EUV-induced carbon

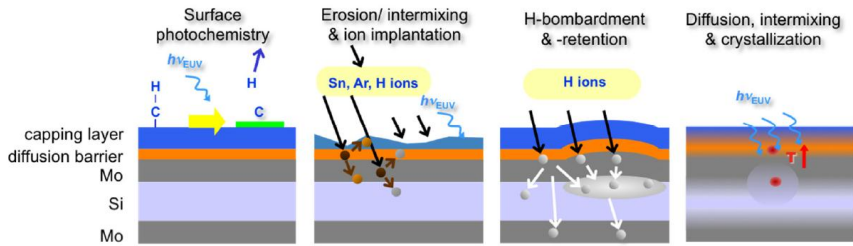


Figure 1.3: Processes that might occur at the surface of EUV optics due to exposures to high-power EUV sources.

layers as well as tin contamination from the source media [79-81] and to reverse oxidation processes on protective layers [82, 83].

When our work was initiated, there was limited pre-existing knowledge in open literature on how hydrogen exposure or the presence of hydrogen in the structure in general can modify the properties of such ML structures (see section 1.4 for more details). In this thesis, we summarize the first exposures done on Mo/Si ML samples using a low energy hydrogen plasma [84]. During that study we have found that surface damage in terms of sputtering and blistering can occur on the surface of such mirrors.

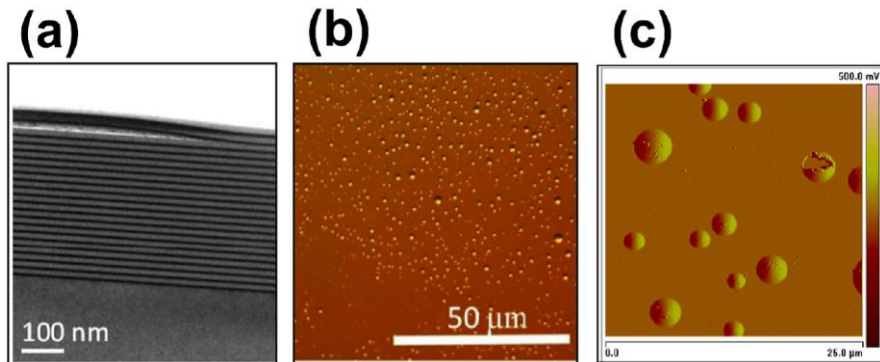


Figure 1.4: Examples of hydrogen-induced blister formation in ML structures. (a) Mo/Si ML after exposure to hydrogen ions [87] (b) hydrogenated Co/Pd ML [88] (c) hydrogenated Si/Ge ML after annealing [89].

The processes of blister formation were investigated in detail and showed a complex behaviour which was strongly dependent on exposure conditions [85,

86] and sample preparation methods. In parallel to our most recent investigations on this topic, hydrogen-induced blistering has now also been observed on ML X-ray optics intended for solar research instrumentation [87], on Co/Pd ML structures studied in context of data storage applications [88] and annealed Si/Ge MLs which can be applicable as solar cells elements [89, 90].

Some examples of blister formation in various ML structures, as explored in this thesis, are shown in figure 1.4. These examples emphasize the importance of work on hydrogen interaction with ML structures and show its multidisciplinary nature. The insights on blister formation in ML structures gained in our research should help in development of mitigation strategies which are necessary to protect various ML samples from aggressive H-containing environments. We have demonstrated that by applying various changes to the design of a ML sample, a significant improvement of the blistering resistivity can be achieved.

1.3. Processes of blister formation.

Blistering is a process of subsurface void formation in bulk materials or thin film coatings.

The main focus for our work lies in the field of blistering induced by exposure to energetic (100's of eV) ions and thermal atomic species. Initial studies of ion-induced blister formation (starting from 1960s) were mainly related to damage of metals (materials for fusion devices or space applications), silicon or oxides, introduced by gaseous ions (hydrogen, helium) [91-93]. Those gases have low solubility in the materials of interest e.g. W or Mo and a build-up of their concentration in near-surface region leads to surface modification in terms of blistering.

Early findings on the processes of ion-induced blister formation were summarized in [94]. There were two concepts of blister formation explored. First was related to blister growth due to high pressure of implanted gas in a cavity. Alternatively, blister growth due to bending of a blister cap was related to high values of compressive stress in the near-surface layer due to a high concentration of implanted gaseous species, whereas cavity was supposed to be empty. However, both of the initial models required the presence of a crack or a cavity in the structure which should precede the growth of a macroscopic blister and the exact mechanism of such blister precursor formation could not be explained.

A later model of blistering describes the surface transformation as a result of a phase transition in the system 'target material – implanted gas'. This process is depicted in figure 1.5. Microscopic gas bubbles are formed as a result of a

Introduction

fluctuation in the density of the implanted gas. These exhibit further growth due to diffusion of trapped gas atoms from the surroundings. This process leads to formation of compressive stress in the near-surface region and material tearing. The layer of the materials above the crack bends due to the influence of the compressive stress.

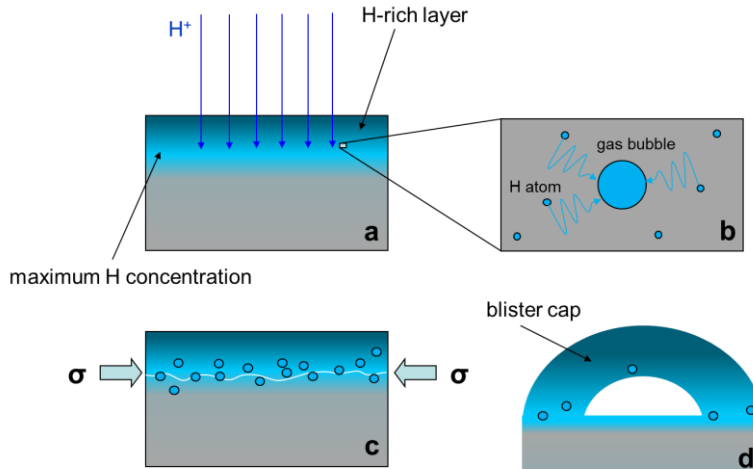


Figure 1.5: Model of blister formation in bulk solid material. (a) H penetration into the sample; (b) formation of H bubbles; (c) crack formation and development of a blister cap, where σ is the maximum value of compressive stress (d) resultant blister.

In the case of thin film coatings blistering and other types of surface damage can occur without any ion exposure. Deposited films can exhibit high values of in-plane stress. As a result of stress relaxation, surface damage in terms of circular blistering, cracking or 'wrinkles' and 'telephone-cord' structures might appear [95-101]. Examples of thin film stress-induced damage are shown in figure 1.6.

Blistering induced by hydrogen loading of metals has been extensively studied as it might seriously influence properties of materials used in various applications. An overview of those studies is presented in [102]. Three main mechanisms have been proposed for hydrogen-induced blistering.

The first mechanism is a general plastic deformation. It is related to hydrogen build-up in the near-surface region at a very high rate. That rate should be higher than that required for hydrogen dissolution into the bulk or discharge from the surface. This can be achieved by a short high-dose hydrogen ion implantation, thermally-induced rapid hydride decomposition of a hydride, or by reactions with water or cathodic charging.

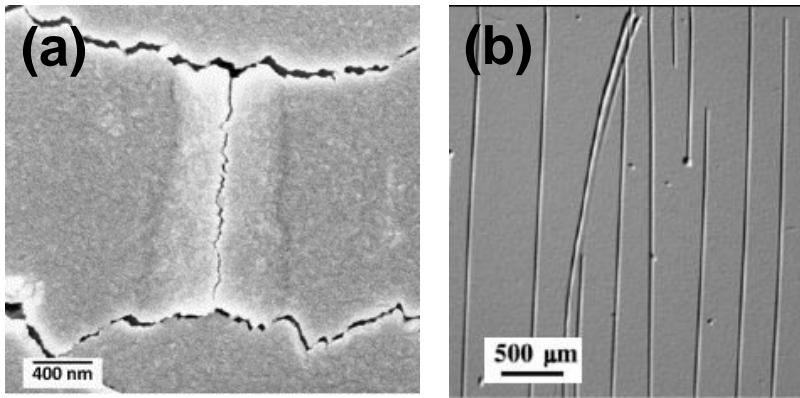


Figure 1.6: examples of stress-induced thin film damage. (a) cracks, Cr thin film on polyamide [97]. (b) ‘wrinkles’, Ni film on polycarbonate substrate [100].

During the process, small bubbles of hydrogen nucleate in the near-surface region and the growth of these bubbles leads to the mechanical deformation of the surface in the form of blistering. The second mechanism of blister formation refers to the formation of blisters in the bulk of materials due to creation and movement of a dislocation loop. This mechanism is called in literature ‘dislocation loop punching’. First, atomic hydrogen accumulates at a nucleation site. Then a hydrogen bubble forms at that site and grows due to continuous adsorption of hydrogen. When the pressure in a bubble reaches a critical value (varies for different metals but in general it is ~ 5 GPa) dislocation loops are created, resulting in matter transport away from the bubble thus enhancing the size of the void.

The third mechanism is active when there is high concentration of vacancies in the metallic sample, e.g. as a result of ion treatment. Hydrogen can combine with a vacancy and form a hydrogen-vacancy complex, here denoted as HV. This complex can further react with other complexes forming H_xV_x clusters and can eventually form a void or migrate to an existing void thus forming a site for hydrogen trapping and blister growth. Additionally, multi-hydrogen vacancy complexes can form and create a high hydrogen pressure in a generated cavity thus inducing blistering by previously mentioned dislocation loop punching mechanism.

Another type of hydrogen-induced blistering is related to wafer splitting methods for Si-on-insulator technology. In that case splitting should be induced uniformly at the same depth to ensure proper layer splitting by means of controlled crack formation on required depth. Early works in this area were predominantly related to high-energy H exposure of silicon. An overview of those studies can be found in [103]. The most advanced and the most relevant to

Introduction

the topic of this thesis is the example usage of a buried stressed layer to produce a precise localized delamination in Si-SiGe structure. As it was shown in [32] a compressively-stressed layer acts as a sink for vacancies during the process of exposure to low energy H plasma. Later, the vacancy-rich layer becomes a trapping site for hydrogen and micro-cracks (platelets) are formed as a consequence. This example shows that a detailed knowledge of the behaviour of hydrogen atoms and vacancies is important for understanding of the processes of hydrogen-induced blistering in composite thin film coatings.

1.4 Hydrogen-induced effects in composite structures.

At the time when the current work was initiated, there were only few (pre-)existing examples of EUV multilayer-relevant studies. In this subsection an attempt is made to summarize the earlier results on blistering in ML samples and to identify areas where additional research, like described in this thesis, is desirable.

Table 1 summarizes the earlier findings on blistering/hydrogen-induced effects in ML or complex structures available in the beginning of the author's research project (2008). It also indicates what information is missing, incomplete or not covered in those investigations with respect to the current contribution. After the table, a more detailed description of relevant pre-existing experiments is presented.

Knowledge was especially limited on hydrogen-induced changes in ML structures as a result of energetic ion (100-1000 eV range) or thermal atom exposure. Information about the role of the incoming particles (ions, neutrals, synergetic effects) on the structural changes in ML samples as well as role of exposure parameters (sample temperature, ion/neutral flux and fluence, origin of irradiation species) was missing. There was no model established on how hydrogen-induced blistering can be initiated and further develop in multilayered structures, in particular, in case of Mo/Si MLs with few nm thickness of the individual layers. As a result, no information was available that could facilitate the development of mitigation strategies to suppress or minimize undesirable formation of hydrogen-induced blisters in multilayered structures when necessary for their application in harsh environments. These facts have been motivating the work presented in this thesis.

Table 1. Summary of experiments on hydrogen-induced effects in ML or complex samples. The categories refer to the corresponding parts of section 1.4, indicated between brackets.

<i>Noble gas ion exposures of ML structures (1.4.1)</i>			
experimental procedure	references	observed phenomena	missing information
exposure to high-energy noble gas ions; computer simulation of such exposure	59, 104, 107-109	top surface etching, blistering, blister localization at interfaces	no exposures to hydrogen ions/radicals conducted, only high-energy ion exposures (keV)
<i>Hydrogen ion exposures of ML structures (1.4.2)</i>			
exposure to high energy hydrogen ions	114	no damage to ML structure observed	only high-energy exposure (MeV), no reporting of blistering
<i>Hydrogen incorporation in ML structures during sample deposition (1.4.3)</i>			
exposure of growing ML structure to hydrogen: additional H ions from an ion gun or H ₂ in the sputter gas	105,106	high H content in Si layers (30 at.%), swelling of Si layer, no damage observed	treatment during deposition, no reporting of blistering
<i>Annealing of H-containing ML and composite structures (1.4.4)</i>			
annealing of pre-loaded (during deposition) ML structures, H ₂ adsorption by ML from gas phase, alloy annealing in H ₂ environment	89,90,110 111	blistering or sample degradation observed for ML structures, enhanced segregation observed for alloys	no exposures to hydrogen ions or radicals conducted
<i>Hydrogen-induced modification of ML magnetic properties (1.4.5)</i>			
H ₂ adsorption from gas phase	112,113	no damage to ML structure observed	no exposure to hydrogen ions/radical conducted, no blistering observed

Introduction

1.4.1 Noble gas ion exposures of ML structures.

Formation of blisters was reported as a consequence of interaction of high-energy (keV range) noble gas ions with Mo/Si ML samples [59]. This experiment was conducted as a model study of potential damage to the EUV lithography mirrors from the ions impinging from Discharge Produced Plasma (DPP)-based EUV sources. However, the phenomenon of blistering was not reported in detail. Later theoretical work, serving to create a mathematical model of noble gas-induced blistering on EUV optics-relevant samples, has confirmed the possibility of blister formation [104] and showed formation of blisters at interfaces between Mo and Si layers.

Another example of an area where noble-gas induced blistering in ML structures has been explored is related to the development of coatings with high resistivity to high-energy helium ion impact. This might be of relevance, for instance, to the development of fusion or nuclear reactor wall materials. Cu/Nb and in later works Cu/V multilayers have been studied in this context [105-107]. Cu/Nb MLs have shown high resistivity to helium impact in terms of radiation damage, including blistering. This was attributed to a high density of He sinks at the Cu-Nb interface.

1.4.2. Hydrogen ion exposures of ML structures.

The only known example of hydrogen ion exposures of MLs relates to high-energy (MeV range) proton exposures of various ML samples (including Mo/Si) as a procedure in development of X-ray mirrors for solar research [108]. In that case no significant changes in the samples due to hydrogen exposure were mentioned.

1.4.3. Hydrogen incorporation in ML structures during sample deposition.

Usage of hydrogen during the deposition process of ML samples has been mentioned in the context of mirrors for EUV lithography. For instance, exposure to low energy ions was used as a step in Si layer deposition in a Mo/Si ML structure, as it was considered to enhance the reflectivity of the ML [109]. A H content of about 20-30 at.% has been reported. Hydrogen-induced swelling of the Si layer has been observed, however the results were not fully conclusive. Similar ML samples were also deposited by changing the sputter gas from Ar to an Ar/H₂ mixture [110]. In this case a H content of up to ~ 30 at.% was reported for Si layers whereas the Mo layers were not modified by the presence of H in the sputter gas. No cases of substantial hydrogen-induced deterioration of ML structure were reported in that context.

1.4.4. Annealing of H-containing ML and multicomponent structures.

Preceding to our work, hydrogen-induced blistering has been found as a result of annealing of hydrogenated Si/Ge ML structures [90]. Further analysis of this phenomenon has been done in parallel with our investigation [89]. However, in that case sample hydrogenation was done during the deposition process of the ML structure by adding hydrogen in the deposition chamber rather than by doing an exposure to H-containing environment.

Hydrogen interaction with MLs has been studied in terms of development of new materials for hydrogen storage. For instance, MgNi/Pd multilayers have been studied in this context [111]. They have exhibited degradation after several cycles of hydrogen loading-unloading. It was attributed to volume changes related to hydrogen uptake and consequent annealing. As a consequence, the Pd layer peeled off from the MgNi layer thus causing deterioration of the performance. More recently, similar effects have been observed for Mg/FeTi nanolayered composite films [112]. One should note that in the context of hydrogen storage, the hydrogen impacts the ML structure only in form of H₂ molecules. Thus those effects are most likely less severe than in cases of exposures to thermal hydrogen atoms or energetic ions.

Another type of hydrogen-induced modification of composite structures was reported for Pd-Pt alloys, where Pd surface segregation upon annealing was significantly influenced by presence of hydrogen.

1.4.5. H-induced modification of ML magnetic properties.

Hydrogen is also known to be able to change magnetic properties of several types of ML structures [113, 114]. However, prior to the start of the work described in this thesis, cases of hydrogen-induced deterioration of such systems were reported.

1.5. Laser plasma-wall interactions.

The previous sections covered cases of particle interaction with surfaces that were related to interaction of single-charged hydrogen ions, thermal radicals and molecules with surfaces. Another example of plasma-wall interaction is the exposure of a solid surface to dense plasmas containing highly-charged ions.

The contribution of this thesis to this field is an approach to simulate high power and particle loads in fusion devices [115]. Extreme events in tokamaks, for instance Edge Localized Modes (ELMs) produce high heat and particle loads which can cause severe damage of wall materials in terms of melting and cracking due to thermal shocks [116-118]. It is quite difficult to study those processes directly in a tokamak due to complexity of the plasma-wall interaction and inability to isolate the parameters influencing such interaction.

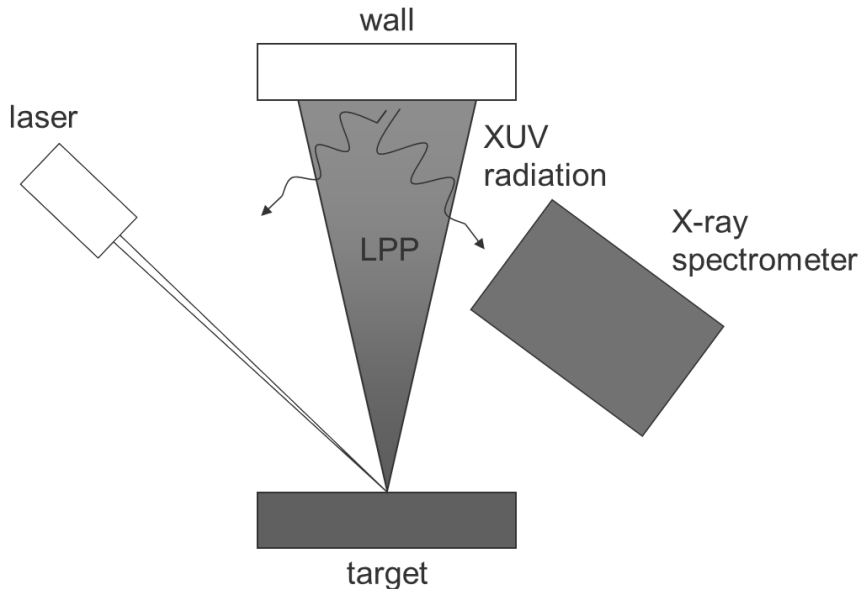


Figure 1.7: Scheme of a laser plasma –wall interaction experiment.

Laboratory experiments dedicated for such studies usually require complex installations and experimental procedures. In this thesis, usage of a laser plasma-wall interaction (LPWI) process is used as a complimentary technique to existing experimental facilities [119-121]. LPWI processes are processes of interaction of a laser produced plasma (LPP) with a solid wall placed in its pathway. A schematic of a LPWI experiment is shown in figure 1.7.

The LPWI phenomenon was observed and described for the first time in [122] and further investigated in [123-125]. It was shown that x-ray emission in the

VUV and XUV ranges is observed as a result of LPP interaction with a wall. That is why well established in-situ diagnostics (x-ray and extreme ultraviolet (XUV) spectroscopy) can be used to study the processes of plasma-wall interaction in LPWI experiments.

Despite the existence of previous contributions exploring the idea of LPWI usage for simulation of high power and flux events in tokamaks [126], in our work the comparison was made between the tokamak and LPWI conditions and the consequences of the parameter mismatch were discussed.

1.6 The contribution of this thesis.

Further enhancing the lifetime of EUV optics is one of the most important goals in public research programs in support of EUV photolithography. The underlying physics questions were at the basis of the comprehensive research program CP3E ('Controlling photon and plasma induced processes at EUV optical surfaces') carried out as an Industrial Partnership Programme (IPP) at FOM in collaboration with ASML and Carl Zeiss SMT GmbH. The research described in this thesis was executed in the framework of XMO ('eXtreme Multilayer Optics', an IPP with Carl Zeiss SMT), a pioneering activity for CP3E project.

As an example of work relevant to understanding the key processes at the surface of EUV optics, chapter 3 of this thesis describes a first experiment on the interaction of low-energy hydrogen plasma and thermal species with representative samples (Mo/Si multilayered structures). We have found that hydrogen accumulation, top Si layer etching and blister formation can occur as a result of such interaction [84, 86]. Blistering of the samples is due to delamination of one or two outermost bilayers of the Mo/Si ML structure. In the latter chapters the effect of blister formation was investigated in more detail.

Chapter 4 of this thesis further explores the studies of blister formation in ML structures by showing the presence of two pathways to blister formation: -one induced by thermal hydrogen species, facilitated by low-energy ions ('thermal neutral process'), and a second based on exposure to energetic (100's of eV) ions ('ion-induced process'). In the first case blisters were formed on pre-existing nucleation sites in the structure, whereas the 'ion-induced' process leads to creation of new sites for blistering due to ion-induced damage to the ML structure. Blistering is a result of interaction of hydrogen with pre-existing or new vacancies in the sample introduced by formation of hydrogen-vacancy complexes. These findings show that knowledge of the exposure conditions is important to understand the nature of hydrogen-induced changes in ML samples.

Introduction

Chapter 5 shows the dependence of blister formation on the accumulated hydrogen in the structure (retained fluence) and the formation of blisters. It also reports high-resolution (nm range) depth profiles of hydrogen in Mo/Si ML samples. A remarkably high H concentration (~ 19 at. %) was found in the outermost Mo layer.

In chapter 6 the influence of the irradiating species composition on the processes of blister formation is further explored. Energetic ions were found not only responsible for ‘ion-induced’ process of blister formation but also for having a strong influence on the ‘thermal neutral’ process. That influence was found to be related to competing processes of ion-enhanced trapping of neutral hydrogen species and dilution of trapped hydrogen among new ion-induced blistering sites. Accordingly, processes lead to enhanced or reduced blister growth. Another influence that was found is enhanced in-depth transport of hydrogen species.

In chapter 7 the influence of exposure temperature on the formation of blisters is discussed. It shows that blistering has a strong temperature dependence. It leads to fewer but larger blisters formed on the samples exposed at elevated temperature. Events of ‘burst’ blisters with full removal of one or two outermost bilayers and etching of the underlying Si layer were observed. The main influence of the exposure temperature is in modifying the behaviour of hydrogen in the system rather than in changing the Mo/Si structure itself.

Chapter 8 describes the work on LPWI experiments implementation to study high power and particle loads in fusion devices. For the first time a detailed analysis of low ionization stages ($Z\sim 5$) LPP interaction with a solid wall has been performed. Electron temperatures as low as 1 eV can be achieved by controlling the parameters of the interaction thus confirming validity of LPWI approach to tokamak plasmas. Possible influences of the remaining discrepancy of the interaction parameters and ways of its elimination were discussed.

Chapter 9 describes how the findings reported in chapters 3 to 8 can be used in practical applications. Development and testing of successful mitigation strategies, which dramatically enhance the durability of ML samples for incident atomic and ionized hydrogen species, is described. In addition, recommendations are given on possible methods to enhance hydrogen storage properties of ML structures by interface engineering and for usage of LPWI for selected applications. Examples of the industrial partners’ direct interest to the work presented in this thesis are given.

2. Experimental

2.1 Multilayer sample deposition.

The ML samples that are studied in chapters 3-6 were deposited on Si substrates by magnetron sputtering. The depositions were performed at the Advanced Deposition Coating facility (ADC) at FOM Institute DIFFER. The main principle of magnetron sputtering is physical sputtering of a negatively biased target by impinging positive gaseous ions. A plasma is created by electron impact ionization of a gas by electrons emitted from a cathode.

In addition, an ion polishing step was used during the deposition of Si layers in order to minimize the interface roughness [127, 128]. Low-energy noble gas ions (150 eV) emitted from a Kaufman ion gun were used for that purpose. Some samples described in chapter 8 were deposited by e-beam deposition at the Multilayer Coating facility (MUCO) at the FOM Institute DIFFER. The idea of the method is in evaporation of a target material by electron beam heating. As a result, the emitted atoms have low energies (< 1 eV) and the resulting thin film typically has lower density than in case of magnetron sputtering [41].

2.2 Hydrogen exposures of ML samples.

The majority of the samples studied in chapters 3-6 were exposed in Hydrogen Treatment Chamber (HTC) set-up at the FOM Institute DIFFER. The basis of the experimental set-up is an UHV-compatible vacuum chamber with a turbomolecular pump. It allowed a typical background pressure (without bake-out) for all experiments of $\sim 10^{-8}$ mbar. The set-up has three hydrogen sources that were used for the experiments described in the thesis. A photograph of HTC and a schematic of the set-up are shown in figure 2.1. A Retarding Field Analyzed (RFA) on a movable XY stage was attached to the system in order to measure ion energy/spatial distribution from the capillary cracker source. Figure 2.2 shows close-up images of the various irradiation sources during operation.

The first exposure tool is a thermal capillary gas cracker TC-50 produced by Oxford Applied Research (figure 2.2(a)). The working principle of the cracker is in dissociation of hydrogen molecules on hot walls of a heated capillary. The capillary is heated by electrons emitted from a hot filament, which are accelerated by a bias of +1000 V applied to the capillary.

This type of hydrogen source typically provides a sharp profile of atomic species; however the exact shape of the neutral peak is pressure-dependent [129-131]. As will be discussed later, the non-uniformity in neutral profile

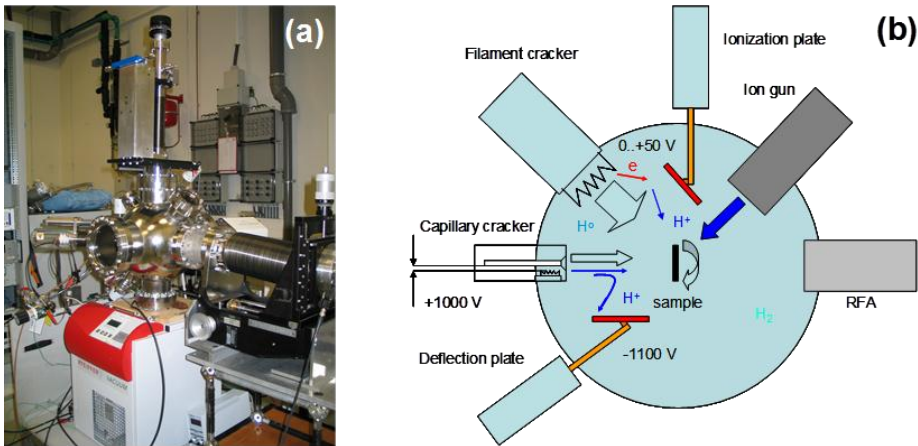


Figure 2.1: Hydrogen Treatment Chamber set-up: (a) photo of the set-up. (b) scheme of the set-up during the operation.

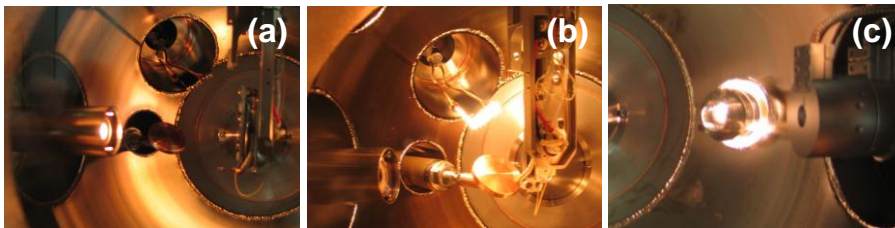


Figure 2.2: hydrogen irradiation sources under operation. (a) capillary cracker; (b) filament cracker; (c) ion gun.

might be a factor resulting in differences in blister growth at different locations on the sample.

The capillary cracker was operated with hydrogen flows of 0.2 – 2.0 SCCM, provided via a flow controller, resulting in operating pressure in the chamber from 1×10^{-5} mbar to 1×10^{-4} mbar respectively. Resultant fluxes of atomic and molecular hydrogen can be estimated based on the quoted cracking efficiency (which is 50% for hydrogen). For example, at 1.0 SCCM gas flow (used for the majority of the exposures in chapters 3-6) the flows of atomic hydrogen (H_0) and molecular hydrogen (H_2) were estimated as $\sim 4 \times 10^{17}$ $\text{cm}^{-2} \text{sec}^{-1}$ and 2×10^{17} $\text{cm}^{-2} \text{sec}^{-1}$ correspondingly. In addition to atomic and molecular species the cracker also produced an ion flux on the order of 5×10^{11} $\text{cm}^{-2} \text{sec}^{-1}$. The ion energy (as measured by the retarding field analyzer) spanned the range between 0 and 1000 eV with two distinct maxima at ~ 860 eV and at 1000 eV.

Experimental

The second hydrogen source is a filament hydrogen cracker provided by Nederlandse Organisatie voor Toegepast Natuurwetenschappelijk Onderzoek (TNO), see figure 2.2(b). In this case cracking of hydrogen happens at a hot filament (~ 2000 °C). This type of the source is similar to hydrogen sources proposed for removal of EUV-induced carbon or tin contamination from optical surfaces [81, 132]. The main feature of this source is that it can operate at high H_2 pressures. Hydrogen was supplied via a flow controller. In this thesis, the hydrogen flow was 30 SCCM and the corresponding working pressure was $\sim 2 \times 10^{-2}$ mbar. The hydrogen flux was estimated by means of exposure of a defined carbon film on glass substrate with post-exposure measurement of the residual film thickness. Knowing the sputtering yield and the density of the film, one can estimate the flux of incoming particles as:

$$f = \frac{\Delta h \rho}{MYt} \quad (1)$$

where f is the incoming flux of hydrogen, Δh is the change of film thickness, ρ is the density of the carbon film, M is the mass of a C atom, Y is the sputtering yield of this particular C film under atomic hydrogen bombardment and t is the exposure time. As a result of such measurement and analysis procedure, the H_0 flux from the filament source was estimated to be $\sim 1 \times 10^{17}$ $\text{cm}^{-2} \text{sec}^{-1}$. In this case, the flux profile is relatively uniform, as determined by ellipsometry after etching of a carbon sample. The flux of molecular hydrogen was estimated as $\sim 2 \times 10^{19}$ $\text{cm}^{-2} \text{sec}^{-1}$.

The third exposure tool used is an ion sputter gun with a heated cathode (Riber CI-10, figure 2.2 (c)). It provides ion fluxes with high energies (typically starting from 500 eV). In this thesis an ion energy of 650 eV was used. The ion gun was fed with hydrogen via a leak valve and the operating pressure in the chamber was $\sim 5 \times 10^{-5}$ mbar. In this case the ion flux was $\sim 2 \times 10^{13}$ $\text{cm}^{-2} \text{sec}^{-1}$, as derived from measuring ion current on the sample during exposure. The corresponding flux of molecular hydrogen was $\sim 5 \times 10^{16}$ $\text{cm}^{-2} \text{sec}^{-1}$.

To control the processes of ionization/ion transport two biased plates were used. The first plate ('deflection plate', see fig. 2.1) which was placed in proximity to the sample served to eliminate ions from the beam of the capillary cracker. By applying a -1100 V bias to the plate a near-zero net current was measured on the sample. The second plate ('ionization plate', see fig. 2.1.) was placed in the proximity of the filament cracker. Applying a positive bias to that plate created an ionization pathway in the vicinity of the sample during exposure. By that means hydrogen ions with low energies (+50 V bias was applied to the plate) were created, some of them impinged on the sample surface in addition to a flux of atomic and molecular hydrogen. The ion currents on the sample were in sub-nA range.

The sample under exposure ($\sim 12 \times 12$ mm) was positioned in a sample holder with controllable heating (e-beam heating stage mounted behind the sample, temperature controlled by a K-type thermocouple). The sample holder was mounted on a Tranzax manipulator allowing changing of the sample position vertically as well as rotation around the manipulator axis.

2.3 Analysis of hydrogen content.

One of the main challenges in the work described in this thesis was to track the content and the depth distributions of hydrogen in ML samples. The techniques that were used for that purpose are described below.

2.3.1 Elastic Recoil Detection (ERD)

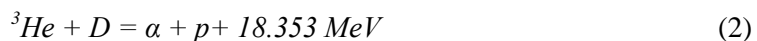
The principle of Elastic Recoil Detection technique lies in detection of sample atoms knocked out (recoiled) in a forward direction due to interaction with an incoming ion beam [133]. For that purpose, a He ion beam with energy in the MeV range is typically used. The beam impinges on the sample at a grazing angle. Scattered He and recoiled H particles moving in a forward direction enter the detector via a foil that stops He ions and only H particles are detected.

ERD analysis was performed by AccTec BV (Eindhoven, the Netherlands). A 3,5 MV particle accelerator (singeltron type) was used for acceleration of He ions. The depth resolution of the analysis was ~ 20 nm i.e. in our case it was used for the determination of total H content in the samples as this resolution is not enough to probe H retention in the layered structure (nm thickness of individual layers). The accuracy in determining H content was 10%. In some cases, samples were exposed to deuterium instead of hydrogen (see chapter 6). In those cases the uptake of D could be clearly distinguished from the influence of background hydrogen in the chamber pre-/post-exposure as well as initial H content of the samples could be disregarded.

2.3.2 Nuclear Reaction Analysis (NRA)

There are two kinds of hydrogen analysis methods based on nuclear reaction events of hydrogen with incoming high-energy ions [134].

The first type of Nuclear Reaction Analysis (NRA) technique is used for samples irradiated with deuterium and is typically used in fusion research for analysis of samples exposed under first-wall relevant conditions (see for instance [135] as an example). It is based on the following nuclear reaction:



Experimental

The proton produced in such a reaction is detected. The energy of the proton depends on the depth at which the reaction occurs since the particle loses energy while reaching the sample surface. Thus, by measuring the energy of the proton, one can determine the depth profile of hydrogen in the sample. The depth resolution of this method is limited for light material by the detector geometry and for heavy materials due to multiple small-angle scattering. This method is typically used for probing samples on large depth scales (μm range) with depth resolution $\sim 0.1 \mu\text{m}$. For ML system described in this thesis this method is applicable for obtaining total hydrogen (deuterium) content of the sample. For that purpose, samples were analyzed at Max-Planck Institute for Plasma Physics (Garching, Germany). The accuracy in determining D content was in the order of 5%.

Another type of NRA measurements represents a very useful technique for analysis of H content in ML structures. In this case, a resonant nuclear reaction is the basis for the analysis:



A scheme of the reaction is presented in figure 2.3.

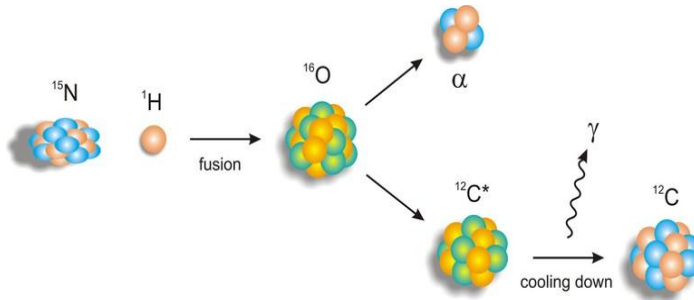


Figure 2.3: scheme of resonant nuclear reaction between ^{15}N and ^1H [136].

The resultant γ radiation is detected and the amount of hydrogen is determined based on the count of photons. This reaction takes place if the energy of the incoming N ion is in a very narrow range with maximum at 6,385 MeV. By altering the energy of the incoming beam, it is possible to control the depth at which the reaction occurs. Depth resolution of $\sim 1\text{nm}$ has been reported for that technique [137]. Based on the stopping power of N ions in the materials of interest, the depth of measurement points can be derived. The error in determination of the analysis points is related to uncertainties in the values of stopping power and was 5%.

Samples investigated in this dissertation were analyzed using 6 MV tandeltron accelerator at Institute of Ion Beam Physics and Materials Research HZDR (Helmholtz-Zentrum Dresden-Rossendorf).

2.3.3 Rutherford Backscattering Spectroscopy (RBS)

To obtain better visualization of the NRA data, in order to present it on a depth scale in length units with an accompanying representation of the ML structure, Rutherford Backscattering Spectroscopy (RBS) was used to determine the thicknesses of individual layers.

This method involves the detection of backscattered atoms (typically with initial energy in MeV range) after their collision with a sample in question [138]. Backscattered atoms are detected by an energy-sensitive detector. The energy of a backscattered atom can be written as [139]:

$$E_1 = E_0 \frac{M_1^2}{(M_1 + M_2)^2} \left\{ \cos \theta \pm \left[\left(\frac{M_2}{M_1} \right)^2 - \sin^2 \theta \right]^{\frac{1}{2}} \right\}^2 \quad (4)$$

where E_0 and E_1 are energies of the incoming particle before and after scattering, M_1 and M_2 are masses of incoming and target atom, respectively, and θ is the scattering angle. Knowing the scattering angle and measuring the energy of the scattered particles, in-depth information on the elemental content of a sample can be determined taking into account energy losses of backscattered particles originating from the depth of the sample.

The procedure of determining the layer structure implemented in this thesis was the following. Total amounts of Mo and Si were determined from RBS measurements in units of at/cm^2 . Knowing the exact number of layers and their density (for simplicity bulk densities were used) thicknesses of individual layers were derived. Note that in this approach layers were assumed to be uniform and no correction was made for interface mixing/compound formation. The analysis was performed at Acctec BV (3,5 MV singeltron accelerator).

2.4. Analysis of blisters by microscopy techniques.

Initially, samples were analyzed by optical microscopy. A Nikon Eclipse ME600 microscope equipped with a digital camera DS-Fi1 was used to take all optical microscopy images presented in this thesis. This allowed for pictures with a magnification of up to 100x. The software used to acquire images from

Experimental

the digital camera was also used for quantitative analysis of the images. Number density, area and radius of blisters were determined.

Selected samples (see Chapter 3) were analyzed by Scanning Electron Microscope (SEM) at MESA+ Institute of Nanotechnology, University of Twente, the Netherlands.

Atomic Force Microscopy (AFM) was used for taking 3D images of the exposed samples and for qualitative analysis of blister dimensions (radius, Z-height). Samples were analyzed at MiPlaza laboratory, Eindhoven, the Netherlands as well as using in-house AFM equipment (Bruker Dimension Edge AFM). Analysis of AFM images was done using the SPIP (Scanning Probe Image Processor) software package.

Information on the exact delamination points of the blisters was derived from cross-sectional Transmission electron Microscopy (TEM) measurements. This method consists of imaging an ultrathin slice of a sample by a high-energy electron beam (typically 100's of keV). The image is magnified and focused onto an imaging system (e.g. a fluorescent screen) and is further guided to a CCD (charge-coupled device) camera. TEM images were obtained using a Philips CM300ST-FEG TEM at the MESA+ Institute of Nanotechnology at the University of Twente.

As an example, comparison of optical microscopy (100x), SEM and AFM images of a ML sample exposed to capillary cracker source for 5 hours at 100 °C using 1.0 SCCM gas flow is shown in figure 2.4. A representative TEM image of Mo/Si ML sample exhibited blister formation is presented in figure 2.5.

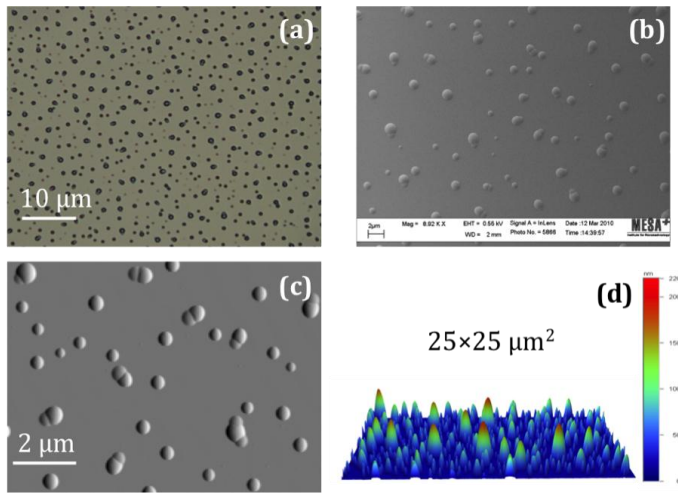


Figure 2.4: Examples of microscopy analysis of blistering on ML samples. (a) optical microscopy, (b) SEM, (c) AFM - 2D, (d) AFM - 3D.

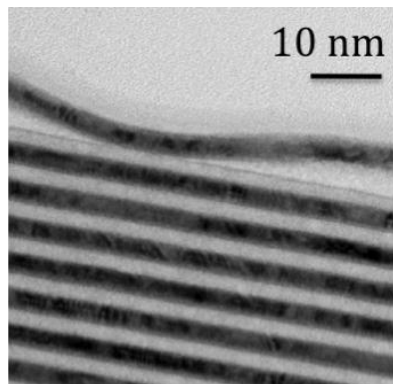


Figure 2.5: Example of a TEM image of blisters formed in a Mo/Si ML sample. Mo layers appear dark and Si layers light.

3. Initial studies of hydrogen interaction with thin film multilayered structures.

Abstract.

Mo/Si multilayer mirrors were exposed to deuterium ions with well-defined energies in order to gain insight into the effects of Extreme UV light driven plasma generation on reflective elements in commercial lithography equipment. Post-irradiation analysis by Rutherford Backscattering Spectrometry (RBS) showed erosion of both Mo and Si layers for the highest energy (50 eV/D) and exposure time (5.4×10^4 s). Nuclear Reaction Analysis (NRA) revealed detectable deuterium retention for energies ≥ 25 eV/D. Surface analysis by X-ray Photoelectron spectroscopy (XPS) showed erosion of the first Si layer for energies ≥ 25 eV/D. Inferences on the spatial distribution of trapped deuterium are made on the basis of available data regarding deuterium retention in the materials in question. In addition, surface modification in terms of blister formation have been observed. Additional exposures to a capillary cracker hydrogen source were done in the order to understand the peculiarities of blister formation, showing strong dependence of blistering on exposure conditions such as hydrogen fluence, surface temperature and origin of irradiating species (H,D).

3.1 Introduction.

Production of multilayer mirrors for Extreme UV lithography (EUVL) requires understanding and control of the physical processes inside and at the surface of the EUV optics. Such optics consists of multilayer coatings designed to reflect the wavelength of interest. They are required to be fabricated with an accuracy on the picometer level. Progress in the development of deposition equipment and procedures has ensured that multilayers fulfilling all optical requirements can be routinely deposited [140, 141]. However, for application in a commercial EUVL environment, there still remains the challenge of possible degradation of optics under the intense power loads and/or repetitive cleaning cycles based on the use of hydrogen. Under these conditions there are a variety of processes that can jeopardize the lifetime of the optics, including photo-chemistry induced contamination, thermally induced inter-diffusion of the multilayer structure, and the interaction of radiation-driven plasma with mirrors.

The chemical composition of the ambient environment is an important factor in determining the lifetime of the optical components. Hydrogen is currently under consideration as a buffer gas in lithography machines in order to suppress tin contamination from the EUVL source [55]. It may also have beneficial effects by, for instance, inducing a self-cleaning process at the optical surfaces and reversing oxidation processes at the surfaces [83]. However, its usage also has potential drawbacks. Among the negative consequences that may arise, hydrogen treatment of the optics may result in retention in the multilayer structure, resulting in swelling and changes to the inter-layer spacing, thus altering the optical properties of the structure. Other processes that may occur include erosion due to energetic (plasma-sheath accelerated) hydrogen ions, enhanced inter-layer mixing and inter-diffusion, acceleration of chemical processes at interfaces due to presence of hydrogen. Some of these processes have been observed in various two-component structures. For example, enhanced diffusion was observed in Pd-Pt or Ni-Cu alloys during annealing in hydrogen atmosphere [142, 143].

The aim of our on-going research is to study the interaction of hydrogen (atoms and ions) with materials that are optically relevant for EUVL, including associated processes such as interactions involving oxygen and nitrogen. The overall goal is to establish a model and obtain the required understanding of (photo-)induced processes involving hydrogen, oxygen and nitrogen at EUVL-relevant surfaces, such as multilayer materials (e.g. Mo and Si) as well as capping layer materials. In this paper we focus on the interaction of energetic deuterium ions with standard, uncapped multilayer mirror surfaces. Blister formation was one of the results of deuterium plasma interaction with the samples. In order to understand the dependences of blister formation on the exposure parameters, such as hydrogen fluence, exposure temperature and

origin of irradiation species (H,D), additional exposures to a capillary cracker hydrogen source have been performed.

3.2 Experimental.

Mo/Si ML samples were prepared, based on magnetron sputtering technique, at the in-house deposition facilities at FOM DIFFER. The samples studied consisted of 50 bilayers of molybdenum and silicon with thicknesses of 3 and 4 nm respectively. The outermost layer was Si.

Irradiation of these samples and post-exposure analytical procedures were conducted at the Max-Planck Institut für Plasmaphysik in Garching, Germany. The sample irradiations were performed in the 'PLAQ' set-up, which uses an electron-cyclotron resonance plasma. A detailed description of the set-up and associated analysis facilities can be found elsewhere [135, 144]. The samples were irradiated with low-energy deuterium (D_3^+) ions (5, 25 and 50 eV/D), with a flux of typically 1×10^{15} D/cm²s. Total exposure fluences of up to $\sim 3 \times 10^{20}$ D/cm² were used. Post-irradiation Rutherford Backscattering Spectrometry (RBS) and Nuclear Reaction Analysis (NRA) measurements were performed to track changes in the samples. Subsequent X-ray Photoelectron Spectroscopy (XPS) analysis was done at FOM DIFFER.

Additional exposures of the samples prepared within identical experimental scheme were conducted at FOM DIFFER. The samples were irradiated with the hydrogen flux generated by a thermal gas cracker (TC-50, Oxford Applied Research). Cracking occurs at the walls of an e-beam heated thin metal capillary (see Chapter 2 for more details). The cracker was attached to a UHV chamber operated at a base pressure of $\sim 2 \times 10^{-8}$ mbar. It was connected to a gas line via a flow controller that allowed a maximum H₂ gas flow of 2 standard cubic centimeters per minute (sccm). The reported cracking efficiency for hydrogen is $\sim 50\%$, which leads to an estimated production of $\sim 8 \times 10^{17}$ H⁰ at./cm²sec at the maximum flow. The cracker is nominally a source of neutral species. However, in actuality it also produced a small ion fraction that was evident as a net positive drain current (in the order of 150 nA at the highest flow) on the sample. Samples were mounted on a sample holder with a heating option. The surface temperature during the exposures shown in this paper ranged from 100 to 150 °C. During exposures with the capillary cracker the hydrogen pressure in the chamber was $\sim 1 \times 10^{-5}$ mbar for the lowest flow investigated (0.2 sccm) and $\sim 1 \times 10^{-4}$ mbar for the highest (2 sccm). The exposed samples were analyzed by means of optical microscopy and Scanning Electron Microscopy (SEM).

3.3 Results and discussion.

3.3.1 Exposures to low-energy plasma.

Let us start with the description of the modification to the samples exposed to low-energy deuterium plasma. With the exception of the sample exposed to the highest energy for the longest time (50 eV/D ions for 5.4×10^4 s), no significant changes in the RBS spectra were observed for the irradiated samples. A comparison of the RBS spectra from the un-irradiated sample and the sample exposed to 50 eV/D ions for 5.4×10^4 s is shown in figure 3.1. The changes observed in the RBS spectra in this case are most likely related to the presence of low levels of impurities in the beam, due to the fact that both Mo and Si layers were eroded even though the energy used is below the sputtering threshold of molybdenum by deuterium. The features in the spectra (going from the right side) represent Mo layers, Si layers and the wafer respectively. Erosion is evident from the shift of the spectrum to the right.

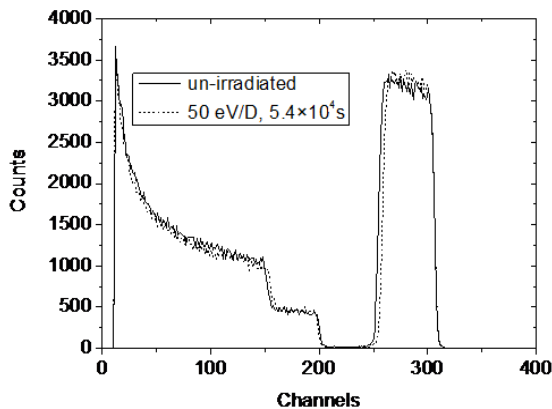


Figure 3.1: RBS analysis of an un-irradiated sample (solid line) and a sample with the highest exposure time at 50 eV/D (dotted line).

Results of the post-irradiation NRA analysis are shown in figure 3.2.

For the 5 eV/D exposures (not shown) there was a slight increase in the NRA signal as compared with the un-irradiated samples. However, this was at the limit of detection (10^{12} D/cm²). Thus, no firm conclusion can be made regarding D retention at this energy. In cases of 25 eV/D and 50 eV/D irradiations (see figure 3.2) deuterium retention is on the order of 1×10^{16} D/cm² for all exposed samples. There is no obvious substantial change in the overall level of D retention on either the energy or the exposure time. The surface region appears to have already saturated after 6000 s exposure and there is no significant difference between irradiation at 25 and 50 eV/D.

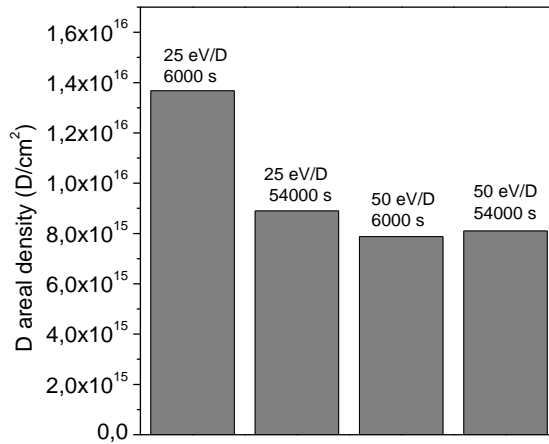


Figure 3.2: Deuterium retention in the multilayer structure for different exposure doses and ion-energies, measured via NRA.

To confirm the state of the surface after irradiation, analysis of surface composition was conducted via XPS. Comparison of a survey XPS spectra from an un-irradiated sample and from a sample exposed to 5 eV/D ions are shown in figure 3.3.

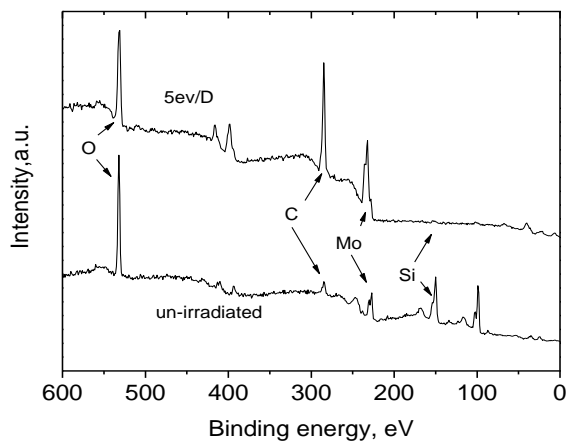


Figure 3.3: Survey XPS spectra of an un-irradiated sample and a sample irradiated with 5 eV/D.

One can see major changes in intensities of Mo 3d and Si 2p peaks after irradiation. It was found that even after irradiation with 5 eV/D ions the first silicon layer was severely damaged as illustrated by the increased molybdenum content at the surface. Quantification of the main surface elements based on XPS measurements are shown in figure 3.4. The left-most (0 eV) data-points are obtained from an un-irradiated sample. The silicon concentration on the surface decreased from 50% to ~3% while the molybdenum concentration increased from 3% to ~15%. This illustrates the silicon depletion from the surface irrespective of the particle energy. Since the sputtering threshold for deuterium bombardment of silicon is approximately 30 eV [145], the results suggest that chemical erosion is an important mechanism for silicon removal in the case of H irradiation.

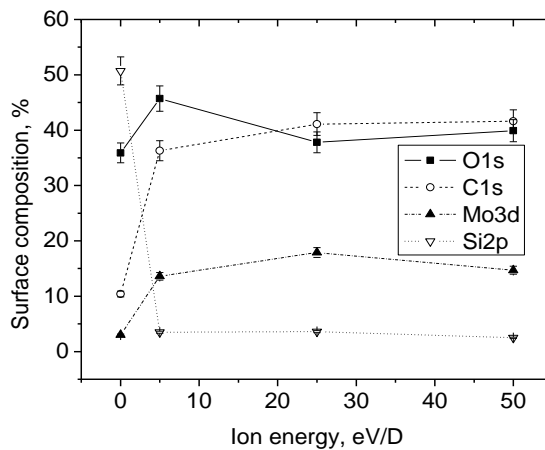


Figure 3.4: Surface composition as a function of incident ion-energy, based on XPS measurements.

The question arises as to where the trapped deuterium is located. We simulated the bombardment process using TRIM, accounting for the erosion of the first silicon layer, in order to estimate the approximate penetration depth of the D ions. The calculations indicated that 25 eV/D and 50 eV/D atoms can only penetrate into the first molybdenum layer. Based on the NRA profiles of deuterium retention from [135], where polycrystalline Mo films were irradiated with deuterium ions, one can make an estimate of the amount of D that can be retained by this layer. From [135], the highest atomic concentration of D measured in polycrystalline Mo was ~6%. Assuming that this value represents the upper limit for D retention in Mo, it gives a value of $\sim 10^{15}$ D/cm² for the 3 nm layer. Note that in [135] 200 eV/D ions were used, so this data might not be representative of the D retention as a result of 25 and 50 eV exposures.

Initial studies of hydrogen interaction with thin film multilayered structures

The samples irradiated with energies 25 and 50 eV/D contain $\sim 10^{16}$ D/cm² based on the NRA data. Hence, retention by an outermost Mo layer is insufficient to explain the results obtained (on the assumption that 6% does indeed represent the saturation value). In this case it is necessary to infer a diffusion processes and that the majority of deuterium is trapped in the second silicon layer or deeper. If we assume all the D indicated in figure 2 is trapped in a single Si layer, then the resultant deuterium to silicon atomic ratio in that layer is approximately 0.4. This value is consistent with the highest hydrogen content obtain by Schlattmann et al. [109]. Hence, such a D content is at least physically possibly. Considering the data from [109], where Mo/Si multilayers were grown with each Si layer being bombarded by hydrogen ions, this deuterium content represents a $\sim 70\%$ density decrease relative to the density of crystalline Si. This leads to the possibility that, as was experimentally reported in [109], the Si layer was swollen. If this is the case, low-energy hydrogen ion irradiation of multilayers will result in a reflectivity drop due to the changed inter-layer spacing. This possibility requires further investigation.

Besides the first layer erosion, blister formation was observed on some of the exposed samples (25 eV/D and 50 eV/D exposed). It was initially evident as whitish discoloration of initially reflective surface. Exposures to the capillary cracker hydrogen source were conducted to understand the dependence of blister formation on the exposure parameters under well-defined exposure conditions. Let us describe the results of those exposures.

3.3.2 Initial observations of blistering.

Damage, which was subsequently correlated with the formation of blister-like features, was first evident to the naked eye as an apparent discoloration of the normally highly-reflective multilayer surface. Analysis by SEM revealed the damage to be due to the creation of μm -sized blisters on the surface (see Fig. 3.5). The appearance of blisters on multilayer samples after exposure to high-energy noble gas (Xe; keV energies) ions has been noted previously [59]. In the current case the energy of the ions involved is much lower and cannot exceed 1 keV (the bias voltage applied to the capillary of the cracker) Thus we report the first observation of Mo/Si multilayer blistering in case of a neutral hydrogen exposure with a fraction of low energy ions present in the beam.

3.3.3 Influence of substrate temperature.

We compared the damage induced after exposure of two identical samples, held at constant temperatures of 100 °C and 150 °C respectively, to the capillary cracker for 5 hours with a H₂ flow of 1 sccm. Note that blistering has been observed for sample temperatures as low as 40 °C. Figures 3.5(a) and (b) show

a comparison of SEM images from the two samples. A clear influence of substrate temperature is evident:

- At the higher sample temperature, the area number density of blisters is lower, but larger blisters are formed.
- At 100 °C the sample appears to have a greater tendency to form “double”-blister structures. When such structures are present on the sample held at 150 °C there is a much larger mismatch in the size of the two blisters.
- Several blister footprints, suggestive of burst/collapsed blisters, are evident on the sample held at 150 °C but not on the sample held at 100 °C.

TEM images (to be published) have revealed the “double”-blister structures to be the result of overlapping delaminations of the first and second bilayers from the top of the MLM structure. The results point to a competition between nucleation of blister sites and blister growth, with higher temperatures favoring the latter. This may be the result of enhanced diffusivity of blister precursors (H(D), vacancies and interstitial defects). Enhanced diffusion results in longer migration distances and will increase the probability of encountering a pre-existing blister relative to the probability of initiating a new blister nucleus. Since transverse diffusion across the bilayer structure is required for the formation of the “double”-blisters, the larger size disparity in the “double”-blisters formed at 150 °C suggests that diffusion in this direction is enhanced to a lesser degree, or not at all, as compared with lateral (within a single deposited layer) diffusion.

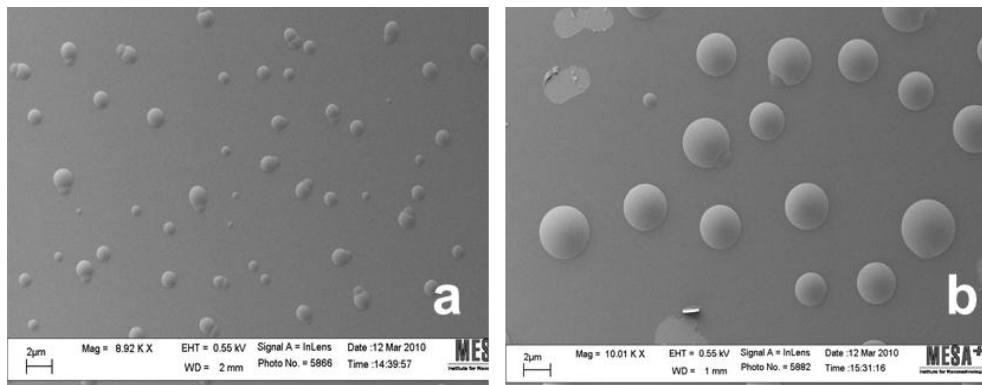


Figure 3.5: SEM images of the samples exposed for 5 hours at different substrate temperatures: (a) 100 °C; (b) 150 °C. The H₂ flow rate through the thermal cracker was 1 sccm.

Figure 3.6 (a) and (b) shows close-up SEM images of blister footprints collected from the sample irradiated at 150 °C. These images show layer fragments and

clear removal of material indicating that the blisters have burst rather than collapsed or cracked. This suggests that pressure build-up (gas incorporation) may have preceded rupture.

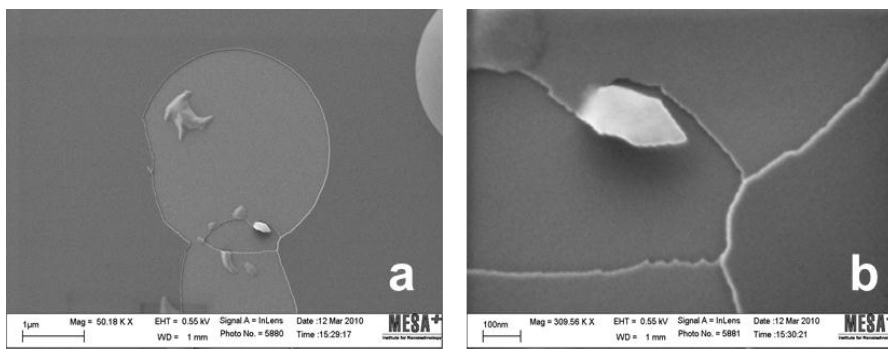


Figure 3.6: (a) Close-up images of a blister footprint collected from the same sample that produced the image in figure 1(b).
(b) Zoomed-in image of a portion of image (a).

3.3.4 Deuterium exposures.

Identical samples were exposed to hydrogen and deuterium from the thermal cracker under similar conditions (5 hours exposure time; 100 °C substrate temperature; 1 sccm). The exposed samples were again studied by SEM. Comparing SEM images on the same scale (Fig. 3.7) demonstrates that the blisters formed during exposure to deuterium are significantly smaller than in the case of exposure to hydrogen, while the area number density of features is higher. This is similar to the trend that was observed for the H₂ exposures at different sample temperatures and may also be due to differences in the rates of diffusion (of the atoms themselves or the H(D)-vacancy complexes that they form).

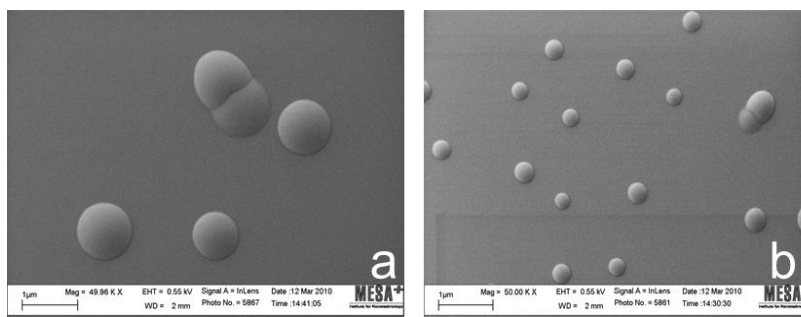


Figure 3.7: SEM images of samples, held at 100 °C, exposed for 5 hours using
(a) H₂ and (b) D₂ in the thermal cracker.

Isotopic effects in ion blistering of materials have been reported previously [146], where hydrogen and deuterium ion exposures of Si and other materials were conducted. The authors observed that higher fluences of D ions were required to form blisters, as compared with H. The authors suggested that the difference they see between H and D induced blistering may be correlated with the differences in hydrogen–vacancy complex formation: H forming hydrogen-rich complexes and D forming vacancy rich complexes. These authors also attributed temperature-dependent changes in the isotope effect to enhanced diffusivity [147].

3.3.5 Influence of total fluence.

A set of 4 identical multilayer samples was exposed for 5 hours at 100 °C to H₂ flow-rates through the cracker ranging from 0.2 sccm to 2 sccm. Increasing the flow results in a higher incident flux such that samples gained a larger total fluence for a constant exposure time. Note that, due to the pressure (flow)-dependent nature of capillary crackers [148], the distribution profile of hydrogen across the surface may change with the flow. Hence, we analyzed the surface modification in the regions of the samples where the maximum flux was coming to the surface.

Figure 3.8 shows optical microscopy images of the resulting damage. The area number density and size of the features tend to increase with increasing gas flow.

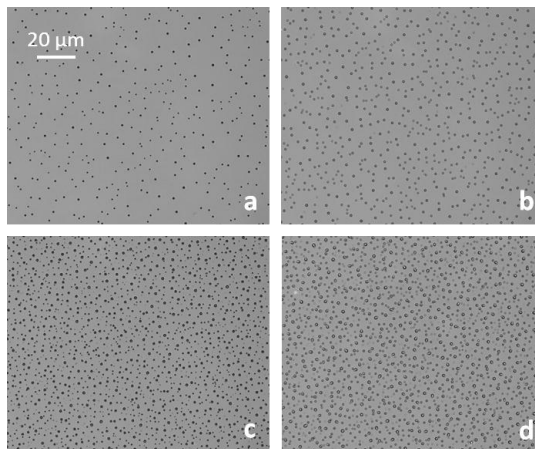


Figure 3.8: Optical microscopy images of samples after exposure for 5 hours at 100 °C to varying H₂ flows. (a) 0.2 sccm, (b) 0.5 sccm, (c) 1.0 sccm, (d) 2.0 sccm. The images were collected at a magnification of 50×.

Initial studies of hydrogen interaction with thin film multilayered structures

A more quantitative analysis of these images was done using image analysis software on the basis of feature size. The number of features on the surface was counted and the total surface area covered was measured. The results are presented in figure 3.9. The total number of structures generated initially increases with the flow, but stabilizes at the highest rates (Fig. 3.9(a)). This suggests that there is an upper limit to the number of features that can be generated on this type of sample. The total surface coverage (area fraction covered in percent) also increases with the gas flow (Fig 3.9(b)). In this case the area covered does not stabilize but consistently increases with the flow, albeit at a slowing rate.

A more detailed analysis of the size distribution of the features in terms of their area is shown in figure 3.10. This reveals a distinct progression in the formation of features. For the lowest flow (Fig. 3.10(a)) only a single size distribution is evident. At an increased flow (Fig. 3.10(b)), the average blister size increases along with the total number of features. With a further increase in the flow (Fig. 3.10 (c)) the size distribution becomes bimodal as a second distinct distribution of blisters emerges. This suggests that there are two distinct fluence thresholds for blistering of the sample. At the highest flow (100%) the average area of both distributions has increased. The spread in the size distribution of the largest blisters also increases.

Since detachment of different layers has been observed by TEM and is also evident in the footprints seen in figure 3.6, it is tempting to correlate the two distributions with blister formation at progressively deep positions in the multilayer structure. However, a direct correlation of blister size with depth for a given set of exposure conditions was not clearly evident from the TEM analysis. Whether the bimodal distribution of sizes is due to a similar mechanism operating on different time/fluence scales or to two distinct blistering mechanisms has yet to be determined.

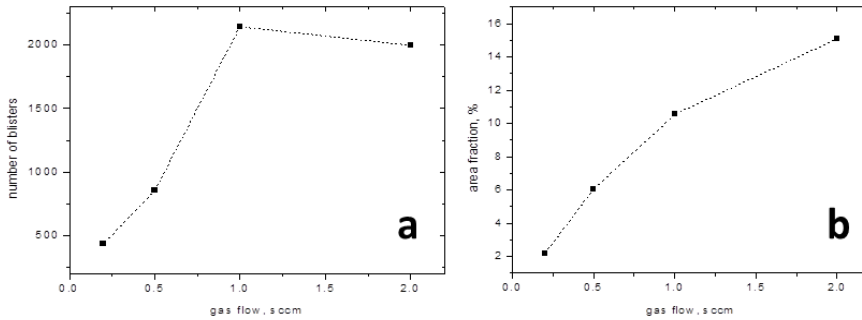


Figure 3.9: Dependence of (a) the total number of blisters formed and (b) the total fraction of the surface covered on the H_2 gas flow for 5 hours exposures at $100\text{ }^\circ\text{C}$. These data points were derived from the images shown in figure 3.8.

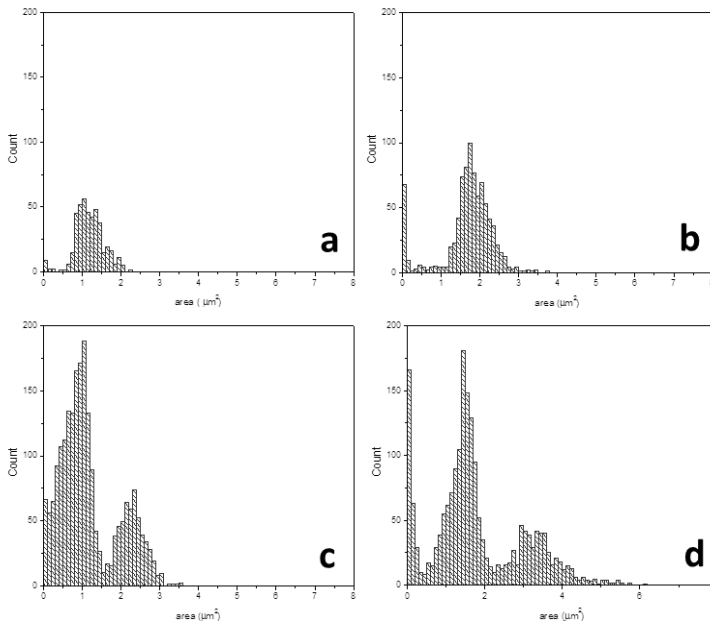


Figure 3.10: Size distribution of blisters for various H_2 gas flow for 5 hours exposures at $100\text{ }^\circ\text{C}$. (a) 0.2 s.ccm, (b) 0.5 s.ccm, (c) 1 s.ccm, (d) 2 s.ccm. These data were derived from the images shown in figure 3.8.

3.4 Conclusions.

In this work we presented first results on hydrogen interaction with EUVL relevant materials. Irradiations of Mo/Si multilayer structures with low-energy deuterium ions were conducted. Analysis has shown erosion of the first silicon layer for ion-energies ≥ 5 eV/D and a deuterium retention of approximately 1×10^{16} D/cm² for energies ≥ 25 eV/D. The penetration depth of ions and the low retention of deuterium by molybdenum suggests that the majority of deuterium diffuses to the layers underneath the molybdenum. If all the D is retained in the Si-layer immediately beneath the outermost Mo layer, then it represents a deuterium to Si ratio of 0.4.

Surface blistering has been another effect of hydrogen interaction with multilayer structures. The extent of surface damage, as represented by blisters, is strongly dependent on irradiation conditions. The effects of substrate temperature, isotopic species and gas flow rate have been studied. The trends observed as a function of temperature are consistent with diffusion playing a role in determining the area number density and average size of the features generated. Changing the source gas from H₂ to D₂ has the opposite effect to increasing the sample temperature: more but smaller blisters are formed.

The number and size of features formed increases with the gas flow. The areal density of features reached saturation at the highest flows utilized, whereas the feature size increased continuously for the range studied. Two distinct size distributions emerge on the surface for exposures with increasing gas flow. This suggests two different fluence thresholds and, possibly, two mechanisms, responsible for the formation of blisters, but does not appear to be directly associated with blistering occurring at differing sample depths.

4. Hydrogen-induced blistering mechanisms in thin film coatings.

Abstract.

We report on the mechanisms of hydrogen-induced blistering of multilayer coating. The blister formation is a result of highly-localized delamination occurring at the two outermost metal-on-silicon interfaces. The number, size, and type of blisters formed varied depending on the composition and ion energy of the incident flux. The results are explained in terms of the multilayer structure being simultaneously susceptible to blistering via two independent mechanisms. A high density of small blisters developed when relatively energetic (several 100's eV) ions were present. Independently, a thermal neutral process that was facilitated by the presence of a small flux of low energy ions (≤ 50 eV) induced a low density of large blisters.

4.1 Introduction.

Blistering and delamination of materials as a result of direct exposure to energetic (keV) ions is a well-known phenomenon [149-151]. The effect is typically associated with stress relief, with the blister formation being localized in a region determined by the mean ion penetration depth. Comparable effects can also be induced with the aid of suitable defect/trap layers. For instance, high energy ion irradiation and implantation followed by low energy plasma-driven hydrogenation has been used to induce delamination of silicon [152-154]. Blistering and the associated buckling and delamination of deposited thin films [95, 155, 156] is also associated with the relaxation of stress [157-159]. Hence, a buried compressively strained layer has been used to induce controlled delamination of thin Si layers [32, 33], with the strained layer acting initially as a preferential trap for vacancies leading ultimately to highly-localized crack formation.

There have been some reports on blistering related specifically to multilayer (ML) systems [105, 107, 160]. These studies have focused on the formation of blisters under high-energy (33-100 keV) He ion irradiation and are aimed at the development of damage resistant materials for use in harsh environments such as fusion reactors. More recently, damage to ML coatings of a type intended for solar mission instrumentation has been reported as a result of 1 keV hydrogen ion bombardment [87]. Layer detachment resulting in a degradation of the optical performance was observed. Similar damage may be induced as a result of bombardment by solar wind particles (see [87] and references therein). It is necessary to fully understand the processes that underpin such effects in order to facilitate the development of MLs intended for use in such potentially hazardous conditions.

We have investigated the susceptibility of the latter type of ML structure to blistering by comparing the effects of a variety of hydrogen exposure conditions on uncapped Mo/Si ML samples. Various exposures resulted in the appearance of symmetric blisters on the sample surface. These were the result of highly-localized bilayer delaminations occurring exclusively at the two outmost Mo-on-Si interfaces. The extent and type of blistering observed was strongly dependent on the composition of the incident hydrogen flux. The samples were unaffected by exposure to neutral hydrogen but exhibited blistering once ions were present. Two distinct blister size distributions are observed. On the basis of correlating the characteristics of the blisters formed with the composition of the incident flux, the ML structure is identified as being simultaneously susceptible to blistering via two separate mechanisms. One is induced by relatively energetic (e.g. 650 eV) ions, while the other is a thermal neutral process that is facilitated by the presence of low energy (≤ 50 eV) ions generating a sub-nA current on the sample.

4.2 Experimental.

The samples investigated were Si-terminated ML stacks consisting of 50 Mo/Si bilayers deposited on an ultra-smooth Si wafer. They were produced by magnetron sputtering, with post-deposition polishing of the individual Si layers by low energy Kr ions [68, 127]. The layer thicknesses were ~3 nm (Mo) and ~4 nm (Si). All samples were exposed to atmospheric conditions after deposition and again after hydrogen irradiation. All irradiations were performed in a single vacuum vessel, which had a typical base pressure of $\sim 1 \times 10^{-8}$ mbar. Samples were mounted on a manipulator that allowed radiative heated from the back side. No pre-treatment was applied to the samples before the hydrogen exposures.

Blistering has been observed after exposures using a variety of hydrogen sources. The results shown in this report are for a capillary-type thermal cracker (Oxford Applied Research TC 50); an ion sputter gun (Riber CI-10) and a hot W filament used in conjunction with an independently biased (+50 V) plate (henceforth denoted “W-fil/Plate”). The filament, sample, and plate formed a roughly triangular configuration. When biased, the plate attracted and accelerated electrons emitted from the filament. The resultant electron ionization produced a net positive current on the sample of ~0.1 nA. Thus, the maximum energy that could be attained by ions reaching the grounded sample surface was 50 eV. The capillary cracker is nominally a neutral source. However, it utilizes electron emission heating of a +1 keV biased capillary resulting in the production of ions that generated a net positive current on the sample. For the current exposures the capillary cracker was operated at a power of 55 W with a 1 sccm flow of H₂. These conditions produced a current on the sample of ~75 nA. Although the ions in the centre of the beam had a broad energy range (0-1000 eV; measured with a retarding field analyzer), the majority of these ions had a relatively well-defined energy of ~860 eV. For the ion gun exposures the ion energy was ~650 eV and the current generated was ~3.9 μ A. The experimental conditions specific to the individual exposures are tabulated later in the text when the effects observed for different sources are compared.

4.3 Results.

Damage to the samples as a result of hydrogen exposure was first evident as a dulling of the original highly-reflective surface that was visible to the naked eye before breaking vacuum (sometimes requiring the aid of a strong light). Atomic force microscopy (AFM) revealed the damage to be due to blister-like structures on the surface. Figure 4.1(a) shows a 3-D representation of a $25 \times 25 \mu\text{m}^2$ AFM scan obtained from a sample after a 5 hour exposure using the capillary cracker. It contains ~450 distinct features. Figure 4.1(b) shows a 2-D representation of a

$5 \times 5 \mu\text{m}^2$ scan from the same sample illustrating the highly symmetric nature of the structures formed. In addition to single blisters, several instances of overlapping double-blisters are visible. Two distinct blister sizes are evident in both images (compare to size distributions in Figure 3.10 of Chapter 3). The majority of blisters have a height of 35-65 nm and a diameter of 300-500 nm. These are interspersed with a lower number of large blisters that have heights up to ~ 180 nm and diameters up to $\sim 1.7 \mu\text{m}$.

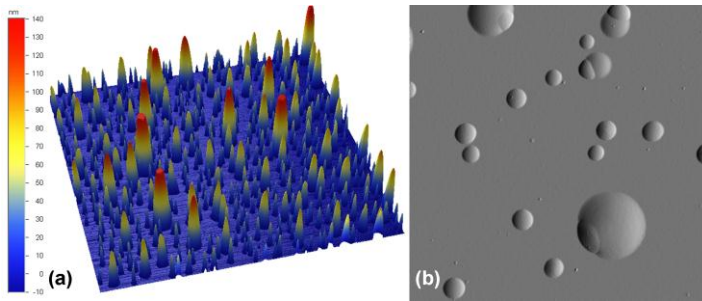


Figure 4.1: AFM images collected from a sample after 5 hours exposure via the capillary cracker. (a) 3-D representation of a $25 \times 25 \mu\text{m}^2$ region. (b) 2-D representation of a $5 \times 5 \mu\text{m}^2$ region.

Cross-sectional transmission electron microscopy (TEM) revealed the blisters to be the result of localized detachments occurring exclusively near the two outermost Mo-on-Si interfaces of the ML stack. Representative TEM images from the sample after 5 hours exposure using the capillary cracker are shown in figure 4.2. The dark (light) layers are Mo (Si). Figure 4.2(a) illustrates the origin of the double-blisters seen in figure 4.1(b). They arise from overlapping delaminations occurring at different interfaces. The larger blister is due to single-bilayer detachment while the smaller blister is due to double-bilayer detachment. Figure 4.2(b) shows a cross-section of a complete blister due to single-bilayer detachment. Figure 4.2(c) shows a close-up of the detachment point of a double-bilayer blister. Detachment at deeper interfaces and detachment at Si-on-Mo interfaces have not been observed.

Blisters developed on the current samples after hydrogen exposure using the three sources listed in the experimental section. A common feature of all exposures that resulted in blister formation was the presence of ions in the irradiating flux. In this report we illustrate the results of various exposure conditions and attempt to correlate them with the likely mechanisms involved. The conditions applicable to the individual exposures are listed in table 1.

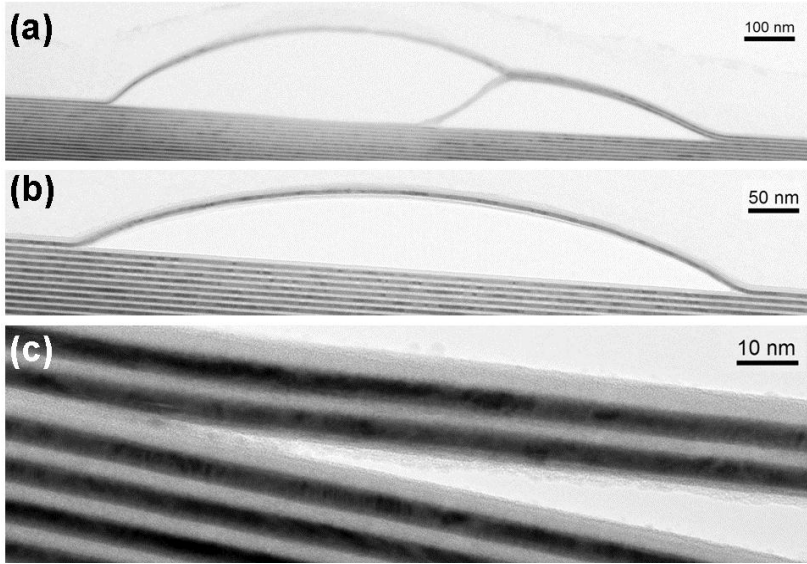


Figure 4.2: TEM cross-sections collected from a sample after 5 hours exposure via the capillary cracker. (a) Double-blister; detachments at 1st and 2nd Mo-on-Si interface. (b) Single-blister; detachment at 1st Mo-on-Si interface. (c) Close-up of a double-bilayer detachment point.

Table 1. Exposure conditions utilized in the current work.

Source	Exposure time (s)	Pressure [H ₂] (mbar)	Sample temperature (K)	Sample current (nA)
Capillary cracker	10800	5×10^{-5}	300-360	75
Capillary cracker	18000	5×10^{-5}	300-360	75
W-fil/Plate	3600	2×10^{-2}	300-390	0.1
Ion Gun	3600	5×10^{-5}	373	3900

The elevated temperatures indicated in table 1 for the capillary cracker and W-fil/Plate exposures are the result of direct heating by the respective sources and the absence of active sample cooling. In the specific case of the W-fil/Plate, once the filament was switched on the sample temperature quickly exceeded 350 K and continued to increase at a more gradual rate over the course of the exposure. Due to the extended time used for the capillary cracker exposures, the temperature was stable at the maximum indicated for most of the exposure. There was no significant direct heating of the sample by the ion gun. Deliberately heating was applied during this exposure in order to maintain the

sample temperature in a range comparable to that produced by the other sources. Blistering at room temperatures has been observed for exposures using the (retracted) capillary cracker and the ion gun. The details of the temperature dependence of the blister formation are currently under investigation. In general, visible damage to the sample surface was observed to develop faster at higher temperatures. In addition, with increasing temperature the number of blisters formed decreases, while the size of individual blisters increases. The exposures performed at room temperature with the ion gun and the capillary cracker both resulted in high densities of very small blisters. Tentatively, the development of the larger blister distribution evident in figure 4.1 appears to be suppressed as the temperature is reduced.

Figure 4.3 shows a comparison of $25 \times 25 \mu\text{m}^2$ AFM images obtained after the various exposures indicated in table 1. All images are represented on a common Z-scale. Figure 4.3(a)&(b) were obtained after exposure via the capillary cracker for 3 and 5 hours respectively. Figure 4.3(c) is the result of the 1 hour exposure to W-fil/Plate (50 V bias) in a hydrogen atmosphere. No damage was evident when a similar exposure was performed without the biased plate. Finally, figure 4.3(d) is the result of the 1 hour hydrogen exposure via the ion gun.

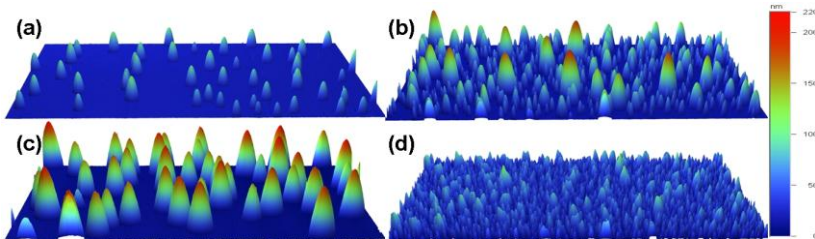


Figure 4.3: 3-D representations of $25 \times 25 \mu\text{m}^2$ AFM scans from samples exposed for: (a) 3 hours and (b) 5 hours via the capillary cracker; (c) 1 hour to the W filament with +50V biased plate; (d) 1 hour via the ion gun.

The 3 hour exposure to the capillary cracker resulted in a low density of moderately sized blisters (as compared with the 5 hour exposure). As already shown in figure 4.1, a high density of small blisters interspersed with larger blisters is present after 5 hours. The W-fil/Plate exposure produced a low density of large blisters after 1 hour. This source produced the largest blisters of the exposures shown. The ion gun produced a very high density of predominately small blisters after 1 hour. Table 2 gives an estimate of the composition and total fluence of particles incident on the sample surface for these exposures.

Table 2. Exposure composition estimates associated with figure 4.3.

Source	Image [figure 4.3]	Fluence estimate (cm ⁻²)			Ion fraction	Ion energy (eV)
		H	H ₂	Ions		
Capillary cracker	(a)	4.8×10^2_1	2.4×10^{21}	5.1×10^{15}	7.1×10^{-7}	0-1000
Capillary cracker	(b)	7.9×10^2_1	4.0×10^{21}	8.4×10^{15}	7.1×10^{-7}	0-1000
W-fil/Plate	(c)	3.6×10^2_0	7.7×10^{22}	2.2×10^{12}	2.9×10^{-11}	≤50
Ion Gun	(d)	-	1.9×10^{20}	8.6×10^{16}	4.5×10^{-4}	650

The ion fluence estimates are based on the drain current measured on the sample plate. For the W-fil/plate and ion gun sources, the H₂ fluences have been derived from the operating pressure in the chamber during the exposures. In the case of the capillary cracker, the H₂ fluence is based on the flow value used and the quoted cracking efficiency of the capillary (50% for H₂). In this case, the contribution from the background gas has been neglected. The H fluence for the capillary cracker has also been derived from the flow value and quoted cracking efficiency. The H fluence estimate for the W-fil/plate source is based on etch rate measurements using deposited carbon films. Note that all of these estimates represent an average over the total sample surface area. However, only the W-fil/Plate source produced damage that appeared uniform. Both the capillary cracker (collimated beam) and the ion gun (ion focusing) have non-uniform flux profiles that resulted in a visible variation in the damage pattern across the surface. For these sources the AFM scans shown in this work were collected in the region of maximum damage (beam center).

Table 3 gives a blister-count and the fraction of the surface covered by blisters for the various exposures. Blisters are designated as “small” and “large” on the basis of their absolute size and aspect ratio (lateral radius:Z-height). Note that this designation is not specifically based on the absolute dimensions of the blisters but on the relative sizes of the features produced by a given exposure. “Large” blisters are present in all cases, whereas “small” blisters are primarily evident in figure 3(b)&(d).

Table 3. Blister count and percentage coverages associated with figure 3.

Source	Image [figure 4.3]	Blister count ^a		Blister coverage (%)
		Small	Large	
Capillary cracker	(a)	7	43	3.7
Capillary cracker	(b)	378	72	17.2
W-fil/Plate	(c)	0	38	13.8
Ion Gun	(d)	3550	177	37.9

^a Blister counts are based on a $25 \times 25 \mu\text{m}^2$ AFM scan area with the exception of the “small” blister count for the ion gun. Due to the high feature density, this count is extrapolated from a higher resolution $5 \times 5 \mu\text{m}^2$ AFM image (142 small and 5 large blisters). In all cases, partial blisters appearing on image borders were not counted.

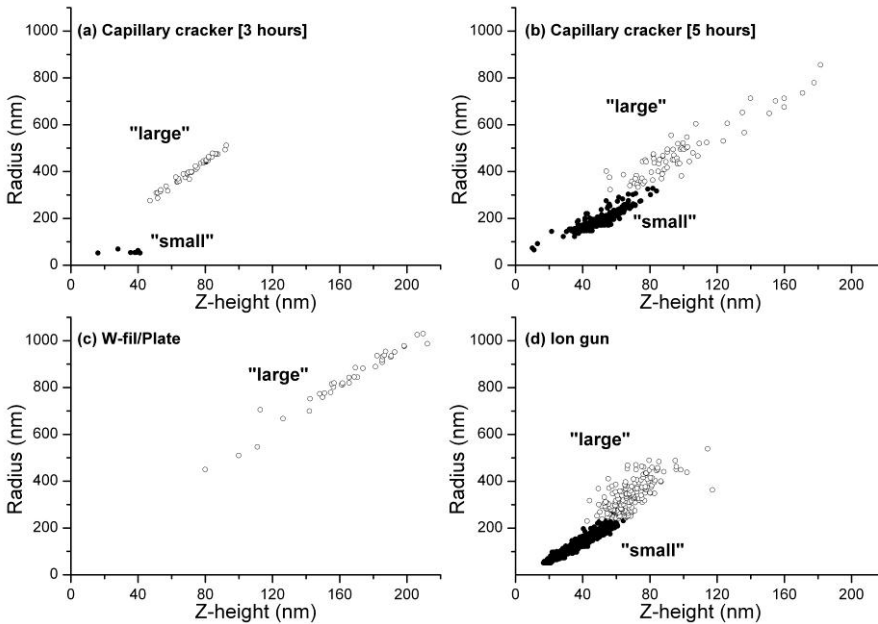


Figure 4.4: Plots of radius versus the corresponding Z-height of the individual blisters derived from the AFM scans shown in figure 3. Filled circles indicate blisters that were designated as “small” and open circles indicate blisters designated as “large”.

Figure 4.4 shows plots of the individual blister radius versus blister height derived from AFM images. The blisters that are designated in table 3 as “small” and “large” are indicated on this figure by filled and open circles, respectively. This illustrates the difference in blister aspect ratio that was used in

distinguishing and quantifying the two distributions. “Large” blisters are somewhat flatter (larger radius for a given Z height) than “small” blisters. The “small” features indicated for the 3 hour capillary cracker exposure are at the limit of the lateral resolution of the AFM image. Hence the dimensions indicated in this case should be treated with caution. These features are currently attributed to the onset of “small” blisters, but they might also represent an early stage of “large” blisters development.

4.4 Discussion.

In the first instance, the hydrogen-induced blistering of MLs can be attributed to stress-induced delamination resulting from hydrogen incorporation into the stack (see literature cited in the introduction). The as-deposited Si and Mo layers in the current samples typically have compressive and tensile stress, respectively [68, 161]. Hence, layer stresses and defects that allow blistering to occur are introduced by the deposition processes rather than by specific post-deposition treatment of the sample. The localization of the delamination point can be understood on the basis of vacancy accumulation and subsequent hydrogen trapping effects introduced by compressively strained buried layers [32, 33]. The Si layers in the current samples play the role of the buried SiGe layers in the previous works. They provide nucleation points for vacancies and incorporated hydrogen, leading ultimately to blister formation.

The unique aspect of the current results is that comparison of the images and correlation of the number and type of blisters formed with the exposure conditions clearly suggests the presence of two independent paths to blistering. One is induced by the presence of “energetic” ions and produced the high density of “small” blisters seen in figure 4.3(b)&(d). The number of “small” blisters produced by these two exposures correlates with the (energetic) ion fluence (see tables 2 and 3), indicating that such ions have the potential to induce new preferential blister initiation sites. The need to create new initiation sites can be expected to introduce a fluence threshold to the appearance of the associated blistering. Such a threshold for the appearance of the “small” blisters is indeed suggested by the comparison of the two capillary cracker exposures (figure 4.3(a)&(b)).

The other pathway to blister formation is a ‘thermal neutral’ process that does not require energetic ions, Blistering induced by thermal neutrals is typically dominated by the availability of pre-existing initiation sites since incident particles do not have sufficient energy to generate new initiation sites. In such cases, the number of blisters that can develop should be primarily related to the sample preparation methods and be relatively independent of the total fluence. The “large” blisters seen in figure 4.3(a)-(c) are attributed to this process. It is noteworthy that the 3 hour capillary cracker and W-fil/Plate exposures produced

a roughly equivalent numbers of large blisters. The 5 hour capillary cracker and ion gun exposures produced noticeably more “large” blisters. However, in both of these cases the blister size analysis is complicated by the presence of double and complex multi-blisters structures. This is reflected in the increased scatter in the aspect ratio of the “large” blisters produced by these exposures (see figure 4.4(b)&(d)). It is noteworthy these double-/complex-blisters structures are only evident on the samples that also exhibit the “small” blisters (i.e. once the influence of energetic ions has manifested). This suggests that there may be an inter-play between the ion-induced and hydrogenation processes. Such an inter-play would also explain the increased number of “large” blisters on these samples.

The size of the individual large blisters produced by the various exposures is most directly correlated with the estimated H₂ fluence. Exposures to date indicate that the main influence of the operating H₂ pressure is on the growth rate of large blisters. Hence, the rapid development of very large blisters by the W-fil/plate exposure is a consequence of the high operating pressure (10⁻² mbar range). When this source is operated at significantly lower pressures (10⁻⁴ mbar range) it also produces a single distribution of “large” blisters, but these develop at a slower rate.

In the scheme outlined above, the ion gun induces blistering primarily via the ion-induced mechanism and the large ion flux quickly produces a high density of small blisters. For the W-fil/Plate only the thermal neutral pathway is open, limiting the number of blisters that form. The ionization pathway provided by the biased plate facilitates the hydrogenation process, but the ions generated do not lead to the creation of new preferential initiation sites. The presence of a high H₂ background induces rapid blister growth as compared with the “large” blisters formed by the capillary cracker. Both mechanisms appear to be operative in the case of the capillary cracker. The features observed after 3 hours of exposure are primarily consistent with thermal neutral process. After 5 hours the large blisters have increased in size, and somewhat in number. However, they are vastly outnumbered by the small blisters. Comparing individual blister shapes resulting from the different exposures indicates that when blistering via thermal neutral process is dominant (W-fil/Plate; 3 hour capillary cracker) exclusively single blisters are formed. In contrast double/multiple-blisters structures are common when the ion-induced process emerges (5 hour capillary cracker; ion gun). This difference is consistent with the proposed dual paths. The energetic ions present in the current exposures are capable of penetrating several bilayers, whereas the first available nucleation interface can act as a barrier to the thermal neutral process.

There are several noteworthy aspects of the current samples when compared with previous reports on the blistering of materials. One is the ability to

efficiently development of blisters using basic laboratory vacuum equipment and relatively benign exposure conditions. This is in contrast to materials that may require high (keV) energies and/or plasma processing in order to induce blisters. Another is the discrete nature and highly self-consistent dimensions of the blisters formed. Equivalent blisters could be induced on different samples in a very reproducible fashion. These characteristics make such samples appealing as a model system for detailed investigation of blistering processes. Their potential in this regard is illustrated by the ability, as demonstrated in this manuscript, to clearly distinguish parallel (and potentially competing) processes.

4.5 Conclusions.

We have demonstrated that hydrogen-induced blistering of ML samples can be strongly dependent on the exposure conditions. Blister formation, which is the result of delamination occurring at the Mo-on-Si interfaces of the two outermost bilayers in the stack, is attributed to a stress-driven delamination of hydrogen-implanted layers. Two distinct pathways to blistering are identified: “ion-induced” and “thermal neutral”. The former is the direct result of the presence of relatively energetic (100’s eV) ions in the incident flux whereas the latter is facilitated by presence of low-energy (≤ 50 eV) ions. The energetic ions can induce new blister initiation sites within the sample. In this case, the number of blisters formed is correlated with the ion fluence received by the sample and there is a threshold to the appearance of blisters. In contrast, the number of blisters formed via “thermal neutral” process is dominated by pre-existing initiation sites that are introduced during the deposition process. The individual blister size in this case is correlated with the neutral hydrogen fluence. The results indicate that careful consideration must be given to the composition of the irradiating flux when analyzing the formation of blisters on such structure.

5. Hydrogen-induced blistering of Mo/Si multilayers: uptake and distribution

Abstract.

We report on the uptake of deuterium by thin-film Mo/Si multilayer samples as a result of exposure to fluxes of predominantly thermal atomic and molecular species, but also containing a small fraction of energetic (800-1000 eV) ions. Following an initial uptake period, the D-content stabilized at $\sim 1.3 \times 10^{16}$ at./cm². The exposures resulted in blister formation characterized by layer detachment occurring exclusively in the vicinity of the Mo-on-Si interfaces. This localization is attributed to the strained centers introduced within the interfacial region due to silicide formation and the subsequent Mo crystallization. The correlation between D-content and blistering was studied. Blister development is not simply a function of the content. Different blistering processes are simultaneously operative, with three distinct distributions being observed. The number densities of the initial two blister distributions to appear are established before the content stabilizes, while the multilayer is susceptible to successive stages of blistering associated with the effects of energetic ions. H-atom depth profiling of hydrogen-exposed samples by resonant nuclear reaction analysis shows preferential retention in the Mo layers. A distinct local maximum with a remarkably high hydrogen concentration (~ 19 at.%) develops in the outermost Mo layer. This is attributed to enhanced accommodation of hydrogen in voids and vacancies within the layer as a consequence of its polycrystalline structure and its highly-constrained state.

5.1 Introduction.

Processing and deposition of layered materials on the nano-scale level is becoming ever more important for technological development. Hence, it is crucial to study the properties of such materials and how they interact with and are modified by their processing and operational environments. Examples include the development and application of thin film and multilayer (ML) structures in general [43], and their interaction with hydrogen in particular [162, 163]. Hydrogen can lead to significant modification of the optical, electronic, magnetic, and structural properties of thin films and MLs. For instance, it can be used to alter the magnetic properties of ultrathin metal MLs [88, 113, 114]. A possible negative consequence of the interaction with hydrogen is the formation of blisters. Several examples of such effects have been reported in different MLs. Blistering has been observed as a result of hydrogen absorption by magnetic Co/Pd MLs [88]. Blister and crater formation occurred after annealing of hydrogenated Si-Ge ML structures relevant to multi-junction solar cells technology [89]. Hydrogen ion irradiation has induced blistering of Mo/Si MLs designed for solar missions [87].

It has been shown that hydrogen-induced blistering of MLs can have a strong dependence on the precise composition of the incident flux [85]. In order to identify the key parameters influencing the formation of blisters, an in-depth understanding of the processes involved in hydrogen interaction with ML structures is required. This will allow estimation of the level of structural modification that can be anticipated prior to exposure to specific hydrogen-containing environments. It will facilitate the development of mitigation strategies to prevent blister formation. Conversely, for thin-layer transfer related techniques, such as those developed in relation to silicon-on-insulator technologies [164, 165], enhancement of the localization and rate of layer detachment is desirable. In both cases, understanding of the correlation between the hydrogen fluence received and the resultant hydrogen content, and of the consequent distribution in layered structures, is desirable.

In the current manuscript we have tracked hydrogen uptake and distribution among the outermost layers of a Mo/Si ML. Elastic recoil detection (ERD) has been used to determine the time dependence of the D-uptake by samples exposed to a deuterium flux. Atomic force microscopy (AFM) measurements were used to correlate the resultant blister formation with the D-content. Independently, resonant nuclear reaction analysis (NRA) was used to obtain H-atom depth profiles of hydrogen-exposed samples. The distribution of H is related to the stress states of the individual layers and their respective structures (amorphous Si versus polycrystalline Mo). The development of blisters is discussed in light of existing work related to the used of buried strained layers, most notable SiGe layers in order to produce controlled delamination of thin Si

overlayers. A critical factor is the introduction of localized strained states as a result of the formation of a silicide layer and subsequent Mo crystallization during deposition of Mo on a-Si. Combined, the results provide insight into the complexities of hydrogen-uptake and the associated blistering of a nano-layered structure.

5.2 Experimental.

The samples under investigation were deposited using in-house deposition facilities. The pre-deposition pressure in the system was $<1 \times 10^{-8}$ mbar, the main constituent of which was water. The samples were composed of 50 Mo/Si bilayers deposited on an ultra-smooth Si wafer by magnetron sputtering. The first layer deposited (directly on the Si wafer) was a Si layer and the stack was also terminated with a Si layer. The individual layer deposition times were ~ 60 (Si) and ~ 70 (Mo) seconds. Additionally, the Si layers were ion polishing (~ 26 sec) using a Kaufmann ion source in order to minimize the development of interfacial roughness. This ion polishing represented an “etch-back” of roughly 10% of the as-deposited layer. Krypton was used as the operating gas for both magnetron deposition and ion polishing. The interval between individual deposition/etch steps was ~ 35 sec.

Individual layer thicknesses of ~ 2.7 nm for Mo and ~ 4.65 nm for Si were derived from Rutherford Backscattering Spectrometry (RBS) measurements. These estimates are based on bulk material densities, and non-uniformities arising from intermixing and compound formation at the interfaces are not factored in the estimations. Hydrogen exposures were done in a separate vacuum chamber operated at a base pressure of $\sim 1 \times 10^{-8}$ mbar. The samples were exposed to the flux from a thermal capillary cracker source (Oxford Applied Research TC50) operated at a power of 55 W using either D_2 or H_2 at gas flows of 2 and 1 sccm, respectively. Assuming a 50% cracking probability, the resultant neutral atomic fluxes would be on the order of $\sim 10^{17}$ $cm^{-2}s^{-1}$. In addition to the neutral flux, the cracker also produced an ion current on the order of ~ 75 -150 nA/ cm^2 depending on the flow rate. Thus, the ion fraction in the flux was on the order of 10^{-6} . Although the ion energy spanned the range from 0-1000 eV, the majority of ions had an energy >800 eV. All samples were maintained at 100 °C during exposure. Under such conditions, these samples typically exhibited pronounced blistering on a 3-5 hour timescale (neutral fluences on the order of 10^{21} cm^{-2}) [85].

Samples were transported through air both before and after exposure. No special treatment was applied to the samples pre- or post-exposure. Eight equivalent samples were exposed to the deuterium flux from the capillary cracker (2 sccm) for periods ranging from 1 to 8 hours. The resultant structural modification of the ML surfaces was measured by AFM. The total D-content of these samples

was determined by means of ERD. Deuterium was utilized for enhanced sensitivity and, since the D-content in unexposed samples is negligible (in contrast to a native H-content of $\sim 10^{15}$ at./cm²), the determination of absolute uptake as a result of the exposure is more exact. Resonant NRA measurements utilizing the $^1\text{H}(^{15}\text{N},\alpha\gamma)^{12}\text{C}$ reaction [166, 167] were performed on equivalent samples after exposure to a hydrogen flux (1 sccm) for periods of 4 and 5 hours. The amount of hydrogen trapped as a function of depth was derived from measuring the resultant gamma radiation. The correspondence between the incident NRA particle energy and the reaction depth was assigned on basis of the layer profile derived from RBS measurements.

5.3 Results.

We first consider the exposure time (i.e. fluence) dependence of the uptake and distribution of deuterium in the Mo/Si ML structure and its correlation with the consequent blister development. There was no obvious indication of physical damage to the surface of the sample after exposure to the deuterium flux for 1 hour, whereas all longer exposures resulted in a visible “discoloration” of the exposed region, which was a consequence of blister formation. AFM scans revealed the presence of a variety of blister sizes and shapes (single; double; multiple) on the surface. The structures observed were similar to those formed

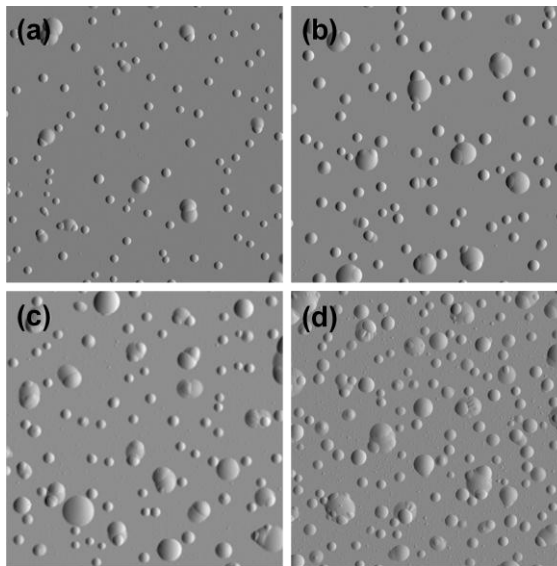


Figure 5.1: 2-D representations of $10\times 10\ \mu\text{m}^2$ AFM scans taken from samples after exposure to the deuterium flux for (a) 2 hours, (b) 4 hours, (c) 6 hours, and (d) 8 hours.

Hydrogen-induced blistering of Mo/Si multilayers: uptake and distribution

after comparable exposures utilizing H_2 [85]. The number and size of blisters increased with exposure time and the extent of the “discoloration” was correlated with this increase. Figure 5.1(a)-(d) shows a series of $10 \times 10 \mu m^2$ AFM images collected after exposure times of between 2 and 8 hours. Two distinct blister size distributions are discernable on these images.

It is evident that extending the exposure times leads to the development of increasingly complex double- and multi-blister structures. After the 2-hour exposure (figure 5.1(a)) most of the blisters in the larger size distribution already exhibit at least a double-blister structure. These become progressively more complex and distorted with exposure time leading to the very complex structures evident after the 8-hour exposure (figure 5.1(d)). The blisters in the smaller size distribution also exhibit complex structures, but these are much less prevalent. Even after the 8-hour exposure a significant number of these blisters are still discrete, single-component features. An additional “third distribution” was also evident in AFM scans (zoomed-in images, not shown). This distribution became clearly evident for exposure times ≥ 6 hours and more than 1600 distinct features were identifiable on a $25 \times 25 \mu m^2$ scan collected from the sample exposed for 8 hours. Its emergence is apparent by the small features (height < 15 nm) that appear in the “flat” regions of figure 5.1(d).

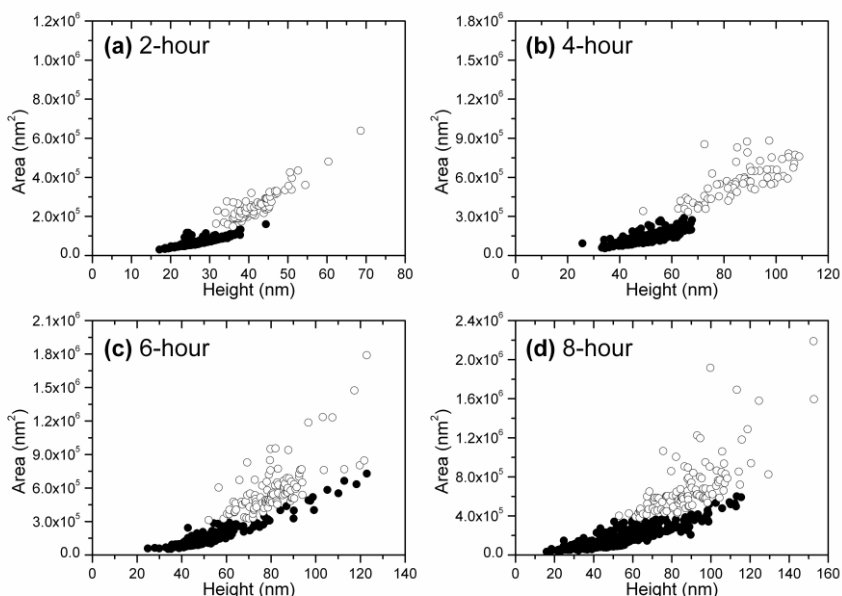


Figure 5.2: Plots of individual blister area versus the corresponding blister height derived from $10 \times 10 \mu m^2$ AFM images. The blisters are assigned as either “ion-induced” (filled circles) or “thermal neutral” (open circles).

Figure 5.2 shows a plot of individual blister area versus height derived from analysis of $25 \times 25 \mu\text{m}^2$ AFM scans. Blisters are designated as belonging to either an “ion-induced” or “thermal neutral” distribution. (The “third distribution” features were neglected for this analysis.) The designation used to identify the two distributions is derived from the previous report on hydrogen-induced blisters [85], in which two distinct distributions were also observed. In that case, comparison of the effects of different incident fluxes indicated that the smaller of the two was due to the action of energetic ions, while the larger was associated with hydrogenation via the incident thermal neutral flux. The designations “ion-induced” and “thermal neutral” are employed as short-hand labels of convenience. It should not be construed that the blisters in the two distributions develop entirely independent of each other. Indeed, the presence of energetic ions has been observed to modify the development of the “thermal neutral” blisters. However, the validity of the generalized designations of these distributions has been confirmed, in particular that the formation of the smaller of the two does indeed require the presence of energetic ions. Role of energetic ions is described in details in Chapter 6. Consequently, their role will not be considered in detail in this Chapter.

For exposure times ≤ 5 hours the distinction between these two distributions was relatively clear-cut. The “ion-induced” blisters were smaller, had a different aspect ratio, and tended to have greater shape uniformity than the “thermal neutral” blisters. With extended exposure time, the dimensions of the blisters in both distributions exhibit increasing scatter and the distinction between the two becomes increasingly blurred. This is due to the emergence of the progressively more complex multi-blister features, as illustrated by Figure 5.1. Such structures can result in a significant change in area covered with little or no corresponding change of feature height. The reverse (i.e. a more dramatic change in feature height relative to area covered) can also occur in the form of “blister-on-blister” structures, several instances of which are visible on figure 5.1(d). These complex features introduce the increased scatter in the data points with increasing exposure time that is evident in figure 5.2.

Figure 5.3 shows cross-sectional TEM images obtained from a D-exposed sample. Blistering is the result of delaminations occurring at the two outermost Mo-on-Si interfaces. This is the same behaviour as was observed in TEM images obtained from a similar samples after H-exposure [85].

Double-blister structures in the “thermal neutral” distribution are the result of overlapping delaminations occurring at different Mo-on-Si interfaces, such as that shown in figure 5.3(b). The multi-blister structures present on the current samples may be more extreme manifestations of the same effect. Note that, unlike the case shown previously from a H-exposed sample, in this particular

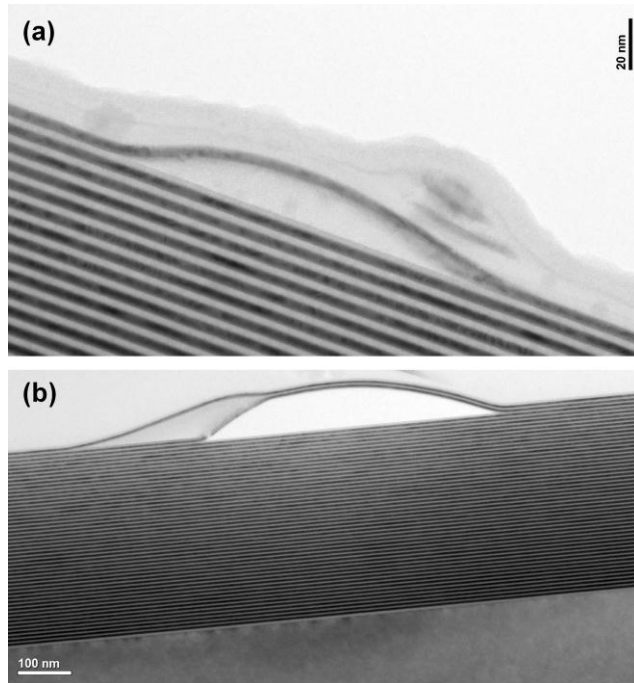


Figure 5.3: TEM cross-sections from a D-exposed sample. Si layers appear light and Mo layers dark. (a) Single blister with delamination occurring at the outermost Mo-on-Si interface. (b) Double-blister structure with overlapping delaminations occurring at the outermost two Mo-on-Si interfaces.

instance the larger component of the double-blister is located at the deeper Mo-on-Si interface.

The total D-content of the exposed samples was determined by ERD and the results are presented in figure 5.4(a). In all cases, the measured D was restricted to the outermost 1.7×10^{17} at./cm² of the ML (~ 30 nm; ~ 4 bilayers). The content increased in an approximately linear fashion during the first 3 hours of exposure. It peaked at $\sim 14.5 \times 10^{15}$ at./cm² and subsequently stabilized at $\sim 12.8 \times 10^{15}$ at./cm². This is comparable to the content that was determined after similar samples were exposed to a microwave discharge deuterium plasma [84]. It was evident from the ERD measurements that the H-content of the samples also exhibited an initial increase and peak with increasing exposure time before stabilizing at a level that was $\sim 50\%$ higher than that of an unexposed sample.

The remaining panels in figure 5.4 show the corresponding evolution of characteristic blister parameters. These are derived from distribution analyses such as those plotted in figure 5.2. The “ion-induced” and the “thermal neutral” distributions are treated both separately and as a single combined distribution. Figure 5.4(b) shows the blister count data. No blisters were evident after the 1-hour exposure, but both distributions were present after all longer exposures. The total number of blisters remains constant for exposure times from 2 to 6 hours and then increases for longer exposures. This increase coincides with the rapid emergence of the “third distribution” (which is not part of this blister count) suggesting that both features are related to a common underlying process. Considering the individual distributions, the additional blisters that develop after 6 hours of exposure are attributed exclusively to the “ion-induced” distribution, whereas the number of blisters designated as “thermal neutral” remains essentially unchanged for exposures of up to 8 hours.

Figure 5.4(c) shows that both distributions exhibit an initial increase in average height as a function of exposure time followed by a stabilization. The average height of the “ion-induced” blisters stabilized after 3 hours. In contrast, that of the “thermal neutral” blisters increased for the first 4 hours. Neither distribution showed any significant subsequent change in the average blister height. Figure 5.4(d) shows the percentage of the surface area covered by the blister distributions after each exposure. The combined data shows an initial growth period from 2-3 hours of exposure, a more gradual increase from 3-6 hours, and then accelerated growth for 7 and 8 hours. Considering the individual distributions, the area covered by “thermal neutral” blisters shows a continuous increase across the full exposure range studied. After an initial period of rapid growth during the first 3 hours of exposure, the area covered increases more gradually with extended exposure time. In contrast, the area covered by “ion-induced” blisters remains constant between the 3-hour and the 6-hour, after which there is a second significant increasing in the total area covered by blisters attributed to this distribution. This increase in area coincides with the increase in the blister count. However, there is no significant change in the average blister height. The reason for this is evident from figure 5.2(c) and (d). These panels indicate that for exposures ≥ 6 hours additional blisters are “added” on both the lower and upper sides of the “ion-induced” distribution. The former is due to the emergence of new blisters, while the latter indicates the resumption of growth (both laterally and in height) of existing blisters. The net effect is a relatively unchanged average blister height.

Hydrogen-induced blistering of Mo/Si multilayers: uptake and distribution

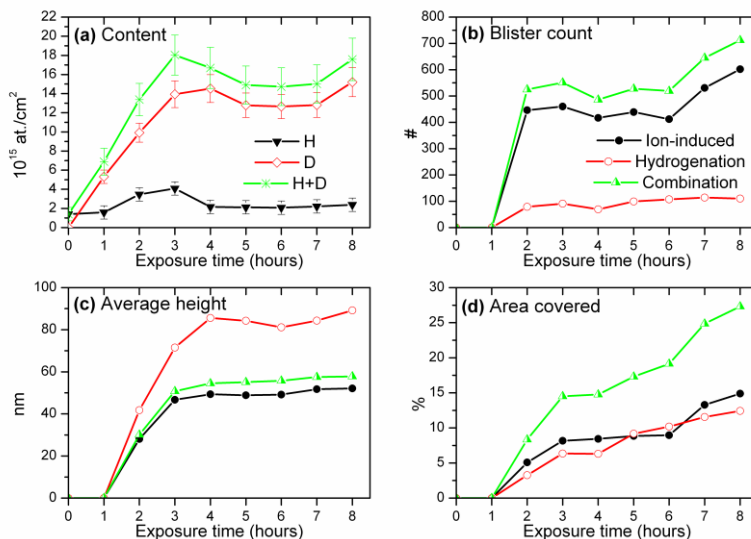


Figure 5.4: (a) H- and D-contents in the outermost 30 nm of the ML sample as a function of exposure time, as determined by ERD. (b-d) Analysis of resultant blisters distributions derived from $25 \times 25 \mu\text{m}^2$ AFM scans: (b) blister count; (c) average blister height; and (d) percentage surface area covered. The trace labels shown on panel (b) apply to panels (b-d).

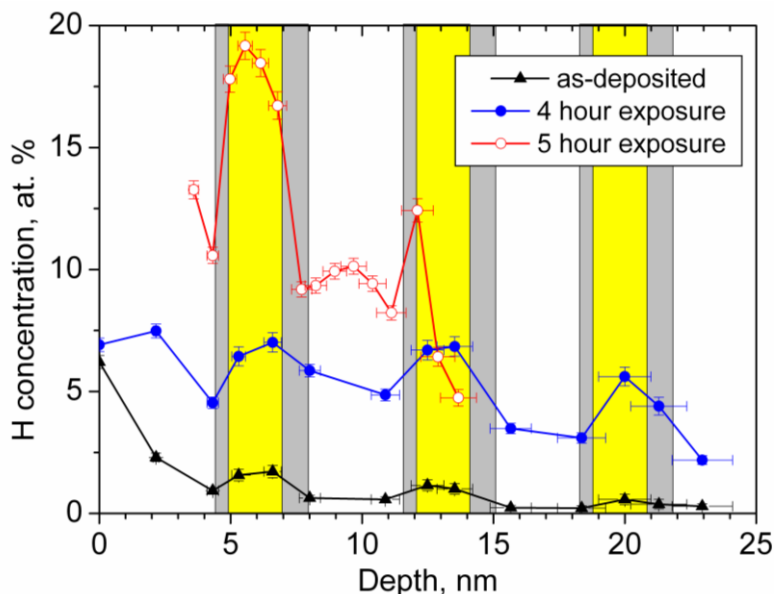


Figure 5.5: H concentration depth profiles measured by NRA. Si and Mo layers are indicated by white and yellow respectively. The intervening grey regions represent likely interface mixing zones.

In order to obtain a picture of how hydrogen is distributed within the ML structure, samples were exposed using H₂ as the feed gas and analyzed by resonant NRA. The results of measurements from an unexposed sample and from samples after 4- and 5-hour hydrogen exposures are shown in the figure 5.5. Due to the difference in flow rates, these exposures are roughly equivalent to 2 and 2.5 hours on the time scale of the D₂ exposures. The approximate ML structure is indicated on the figure. The assignment of reaction depth to incident particle energy was based on the layer profile derived from RBS measurements, which have an accuracy of ~5%. Likely intermixed zones of ~0.5 nm and ~1 nm for the Si-on-Mo and Mo-on-Si interfaces [168], respectively, are also indicated.

An oscillatory variation in H-content that correlates with the ML structure, with enhanced retention in Mo layers, is evident for all samples including as-deposited. After the 4-hour exposure, the H-content of all layers probed by NRA has increased substantially compared to the unexposed sample. The general shape of the profile has not been significantly altered, although the oscillation in the layer content has been enhanced. The increase is largely independent of the layer depth. In contrast, a substantial change in the profile is evident after the 5-hour exposure, with the layers closer to the surface exhibiting enhanced uptake of H. The oscillatory profile is still evident, but with a strong gradient as a function of depth. The content in the first Mo layers now peaks at ~19 at.%. In addition, while the second (deeper) Mo layer now exhibits a lower H-content than the Si layer immediately above it, there is evidence of a strong localized enhancement of the H-content in the vicinity of the intervening interface.

H-contents of $\sim 7.5 \times 10^{15}$ at./cm² and $\sim 1.2 \times 10^{16}$ at./cm² were derived from the 4- and 5-hour NRA data, respectively. These estimates are based on averaging the concentration of individual layers and subsequent summation of the derived contents. The corresponding D-contents obtained from ERD of samples exposed for 2 and 3 hours (compensating for the difference in flow-rate) are $\sim 1.0 \times 10^{16}$ at./cm² and $\sim 1.4 \times 10^{16}$ at./cm², respectively. The agreement between the two methods is reasonable. Interestingly, there is good agreement between the NRA- and ERD-derived contents for the longer exposure times, in spite of the shorter NRA depth range available for the 5-hour exposure. This indicates that the enhanced H-uptake in the outermost layers that is evident in the NRA data between the 4- and 5-hour exposures is being replicated during the D-uptake that occurs between the corresponding 2- and 3-hour exposures.

5.4 Discussion.

5.4.1 Native hydrogen in the MLs

The NRA data from the as-deposited sample indicates a high H-content at the surface with a strong gradient toward increasing depth. Separate ERD analysis of an as-deposited sample indicated a H-content of $\sim 1.4 \times 10^{15}$ atoms/cm², which was localized in the outermost ~ 17 nm of the multilayer. This constitutes a local atomic concentration of $\sim 1.5\%$. A surface hydrogen peak was also seen by Windt *et al.* in ERD measurements on Mo/Si MLs comparable to those used in the current study [169]. Since there was no indication of a significant deterioration in conditions during the final stages of deposition, we do not attribute this H-profile to the deposition process.

The level of the H-signal arising from deeper levels in the ERD data corresponded to ~ 0.3 at.%. Thus, the H-contents determined by NRA in Si and Mo at depths >15 nm (~ 0.2 at.% and ~ 0.6 at.%, respectively) are truer representations of the H-content that arises during the sample deposition. The primary source of this hydrogen is water in the vacuum system, which is the dominant component in the residual gas before deposition commenced. The O- and C-contents of the samples currently under investigation, as determined by X-ray photo-electron spectroscopic depth profiling, were below the limits of detection (1 and 2 at.%, respectively). Windt *et al.* [169] studied the effect of initial background pressure (also predominantly H₂O) in the range 1.33×10^{-5} to 8×10^{-8} mbar. The O content of their MLs was found to be ~ 0.5 at.% while the C content was below the limit of detection (~ 0.1 at.%), with neither content being influenced by the initial background pressure. In contrast, they found a linear scaling of the H-content of their samples with background pressure.

H-uptake during deposition of thin films can have a significant influence on their properties [170-172]. In the specific case of Mo/Si MLs, increased H-content results in a reduction of the overall compressive stress of the MLs [173]. Analysis indicated more compressive Si layers and more tensile Mo layers, with the effect on the Mo layers being ~ 2.5 greater than that on the Si layers. Windt *et al.* reported an average H at.% of $\sim 0.25\%$ for the ML deposited at the lowest pressure ($\sim 8 \times 10^{-8}$ mbar). This is comparable to the content indicated by the NRA and ERD data for the deeper layers in our sample. The better starting base pressure in our case is partially offset by an approximately 5 times longer deposition time as compared to that of Windt *et al.*

The gradient in the H-content from the surface and the elevated content in the two outermost bilayers relative to the deeper layers suggests that the H-content in the near-surface region of samples increases as a result of exposure to ambient conditions (as opposed to a simple accumulation of ad-layer

contaminants). However, it cannot be ruled out that the profile is an effect induced by the analysis beam. In this context it is noteworthy that the ERD analyses of the D-exposed samples tended to show a significant initial decrease in H-content (up to ~57%) upon onset of the irradiation. This was attributed to the removal of adsorbed molecules (e.g. water) due to beam-induced heating of the samples (up to ~70 °C). However, the effect, which was not observed from the 1-hour D-exposed sample, became more pronounced with increased exposure times. It was not observed during ERD analysis of unexposed and H-exposed samples. This suggests that the D-exposures induced structural and/or chemical composition modifications to the surface that increased the carrying capacity for adsorbed species.

5.4.2 Hydrogen uptake and distribution

Broadly speaking, the result of increasing the D exposure time is an initial increase followed by a stabilization of the content in the sample. However, the content also appears to pass through a small maximum around 3-to-4 hours of exposure before stabilizing at a slightly lower value (see figure 5.4(a)). The same trend is also observed in the H-content of these samples, with the H presumably being sourced from hydrogen-containing molecules in the apparatus and on the surface. The simultaneous increase and coincident peaks of the H- and D-contents suggest that synergistic uptake or layer modification effects that alter the maximum “hydrogen” content that can be retained by the ML structure are operative. The effect is transient, with the accumulated H- and D-contents decreasing somewhat with extended time. However, the amount of H in all D-exposed samples remains elevated relative to that of an as-deposited sample.

Considering the uptake and distribution of hydrogen in the samples, the flux incident on the surface was dominated by thermal atoms and molecules, while containing a minor fraction (<0.0001%) of energetic (>800 eV) ions [85]. Hydrogenation of a sample via the uptake and diffusion of thermal species should tend to produce a decreasing gradient from the surface of the sample. In contrast, the ions are capable of penetrating through several layers of the ML structure. Hence the expectation, at least during the early stages of exposure, is that hydrogenation via neutrals should favour uptake by the outermost layers, while ion implantation should play a more important role in the deeper, buried layers.

The NRA data after 4 hours of H-exposure shows a relatively flat profile over the depth being probed. This indicates that the H-content arising from direct implantation and associated ion-induced effects (e.g. facilitated transport of thermal species to deeper layers) is competitive with that arising from thermal species during the initial period. Although the fraction of ions is extremely small, their high energy ensures a much higher uptake probability relative to

thermal species. The oscillatory variation observed after 4 hours is not inconsistent with simple ion implantation. SRIM calculations using 850 eV H⁺ ions also exhibit preferential H retention in Mo layers, which is due to the relative material stopping powers. However, the profile change that occurs between the 4- and 5-hour hydrogen exposures is not consistent with an ion-dominated process.

The strong gradient in H-content as a function of sample depth indicates that thermal processes become progressively more important with extended exposure time and dominate the latter stages of H-uptake prior to stabilization of the content. These processes strongly favours uptake by Mo. Furthermore, the depth profile suggests that the Mo-on-Si interface may act as a significant hindrance to transport to deeper layers. Yamashita *et al.* reported that a strained SiGe layer could prevent penetration during plasma hydrogenation of Si [173]. Hydrogen content can be locally reduced by a compressively-strained SiGe layer [174], whereas it can accumulate in one that is tensilely-strained [175]. In a similar fashion, blocking of hydrogen penetration to deeper layers by the Mo-on-Si interface may be related to the strain in the silicide interface that forms between the two materials (see later). The lack of H-content increase in deeper layers between 4 and 5 hours further suggests that either ion-driven uptake of hydrogen ceases to be effective once a certain fluence limit has been reached and/or that the maximum H-content that can be achieved via ion-driven processes is significantly lower than that which can be realized via thermal hydrogenation processes.

H-retention by the Si layers is almost certainly dominated by passivation of Si dangling bonds. Amorphous Si (*a*-Si) layers deposited in a hydrogen atmosphere [110] or subjected to post-deposition hydrogen ion treatment [109] can accommodate H-contents of up to 30 at.%. In both cases, contents of up to ~20 at.% could be achieved with only a minor decrease in the layer density relative to non-hydrogenated *a*-Si. Thus, the content levels reached in the current case would not necessitate a significant expansion of the as-deposited layers. The activation energy for H diffusion in *a*-Si is reported as ~1.5 eV, as compared with Si-H bond strengths of up to 3.5 eV [176, 177]. Consequently, passivated dangling bonds should represent a stable sink for hydrogen in the Si layers. Based on *ab initio* MD simulations, Su and Pantelides identified a floating bond-H complex as the “migrating species” for H-diffusion in *a*-Si [177]. Abteu *et al.* identified a somewhat similar “fluctuating bond center detachment” mechanism for release of hydrogen bonded within a Si network [178]. Both mechanisms require an active site in the form of an under-coordinated Si atom for the diffusion of H through the layer. The availability of such sites in the as-deposited layer is likely dependent on the deposition conditions. Part of the influence of ions contributing to the two distribution blistering seen in the current study may be due to enhancement of diffusion

through the Si layers via defect introduction and cleavage of existing bonds, thereby introducing new active sites for diffusion.

The H concentration observed in the outermost Mo layer is remarkably high. By way of comparison, retention on the order of several at.% has been reported for Mo and W samples exposed to hydrogen isotopes [20, 135]. The current result is also higher than the H retention measured in disordered nano-crystalline W films (~9 at.%) [179] and is comparable to the maximum H concentration observed during co-deposition of W and H (~16 at.%) [180].

The retention of H by Mo is particularly surprising in light of its positive heat of solution [181]. This is highlighted by the distribution of hydrogen in Mo/V single crystal superlattices [182, 183], where it is localized exclusive in the V layers (V having a negative heat of solution). Somewhat closer to the current ML are Nb/Ta superlattices [184, 185], which are characterized as “weakly modulated” since both materials have an affinity for hydrogen. The Mo/Si system can be considered as an inverse case since neither bulk material is a natural adsorber of hydrogen. A notable difference between metal/metal and metal/semiconductor systems is the potential for a strong chemical interaction between the materials in the latter case.

The polycrystalline nature of the Mo layers in the current case will contribute to the ability to retain of hydrogen. A comparative study on the retention of D by single crystal and polycrystalline Mo indicated a 2 orders of magnitude greater uptake by the bulk in the latter case [135], although the absolute amount remained on the order of 10^{-2} at.%. In this case the chemical state of Mo did not appear to have an influence on the ability to incorporate H, with a MoO₃ layer exhibiting a similar retention to that of polycrystalline Mo.

Rigato *et al* indicated that hydrogen was not retained by thick Mo layers deposited in Ar/H₂ mixtures containing up to 10% H₂ [110]. The stress in the individual layers and the stress differences between layers can play a role in determining hydrogen uptake. The Si layers in Mo/Si MLs with layer thicknesses in the 3-5 nm range typically exert compressive stress, while the Mo layers exert tensile stress [161, 186-188]. In contrast, thick Mo layers exhibit compressive stress [188]. Mo layers deposited on *a*-Si layers exhibit an amorphous-to-crystalline transition at a thickness of ~2 nm and a scaling of the crystallite size with layer thickness above this point [189]. The polycrystalline structure of the Mo layers [190] with the small size of Mo nano-crystallites (~3 nm) [67], should allow for enhanced trapping in vacancies and at grain boundaries and crystallite faces relative to thicker layers containing larger crystallite. This represents an example of a material constrained on the nano-scale exhibiting properties substantially different from those of the corresponding “bulk” [191]. Hydrogen accumulated in this way can more

readily provide a reservoir to feed blister growth than hydrogen that is chemically bound in the Si layers.

5.4.3 Blister development

Figure 5.4(b) illustrates that the initial number density of both “ion-induced” and “thermal neutral” blisters is established well before the D-content reaches a stable value. In neither case is the number of blisters formed a simple function of the D-content. In the case of the “thermal neutral” blisters, pre-existing nucleation sites introduced during sample deposition are likely to play a crucial role in nucleation. Since the number of such sites will be determined by the sample preparation methods, the number of associated blisters that can be formed is inherently limited. In contrast, the creation new nucleation sites by the incident energetic ions should be related to the total ion fluence received. Nonetheless figure 5.4(b) demonstrates that a fluence limit exists, which is reached well before the D-content has attained a saturation value. The early establishment of the number density of “ion-induced” blisters suggests that the processes involved are subject to competition between blister activation/nucleation, on the one hand, and active blister growth, on the other. Growth of existing blisters dominates over the emergence of new blisters, for instance via Ostwald ripening, once a sufficient density of active sites has been realised.

Considering the data shown in figure 5.4(c), the average height of “ion-induced” blisters stabilizes after 3 hours, correlating directly with the stabilization of the D-content. In contrast, the average height of the “thermal neutral” blisters continues to increase during the first 4 hours of exposure. This suggests that their growth has a greater dependence on (re-)distribution of D-species within the ML structure occurring on a longer timescale than the D-uptake. Comparing the trends shown in figure 5.4(c) and (d), the average height of the “thermal neutral” blisters remains stable for the 4-hour and longer exposures. In contrast, the percentage surface area covered by such blisters continues to increase with each extended exposure time. Thus, the “thermal neutral” blisters continue growing laterally even after their height has stabilizes, also suggesting that internal redistribution (e.g. transport; segregation to interfaces) factors significantly in the development these blisters.

The additional lateral growth reflects the emergence of the increasingly complex blister structures seen in figure 5.1. As noted in the Results section, the “thermal neutral” blisters are more prone to develop these structures than the “ion-induced” blisters. This difference points to another distinction between the two distributions. The relatively infrequent development of complex structures among the “ion-induced” distribution suggests that their formation is a random process arising from the incidental overlap of otherwise independent blisters. In

contrast the early and widespread development of double-blisters among the “thermal neutral” distribution points to an active and dependent connection between the blister components. Considering the TEM image illustrating that these blister components originate at different interfaces (figure 5.3(b)), this implied highly localized transport of hydrogen species between the components (i.e. across the bilayer structure).

5.4.4 Blistering mechanisms

The blistering phenomena observed in the current case have obvious similarities with techniques utilized in relation to silicon-on-insulator transfer technology. The original process employs a defined-energy ion beam to cleave a Si sample at a desired depth [164]. However, the use of buried strain layers for the localized nucleation of platelets [32, 33] is more relevant to the current case. In these cases a buried, compressively-strained SiGe layer acts initially as a strong sink for vacancies leading to subsequent accumulation of platelets oriented along the layer plane. Consequently, layer delamination is initiated while avoiding straggling effects typically associated with energetic ions.

In the current case it appears that the interfaces between the Mo and Si layers act as preferred nucleation points for the accumulation of vacancies and mobile hydrogen species. Detachment and the development of macroscopic blisters occur preferentially at Mo-on-Si interfaces. While detachment at Si-on-Mo interfaces was not observed, the spike at ~12 nm depth in the NRA data for the 5-hour exposure indicates accumulation of hydrogen in the vicinity of this interface. A similar enhancement is not evident at the outermost Si-on-Mo interface, although it may be masked by the high H-content in the “bulk” of the Mo layer.

In the case of a Si/SiGe/Si heterostructure, peaks in the out-of-plane strain developed at both interfaces [33]. As-deposited Mo and Si layers in ML structures such as those currently under investigation are typically tensile and compressive, respectively [161, 169, 186, 192]. While the Si layers are amorphous, the Mo layers exhibit an amorphous-to-polycrystalline transition at a thickness of ~2 nm [67, 189]. Zubarev *et al* identified a (1-2 nm) cluster form of Mo, which developed at nominal layer thicknesses between 1.5 and 1.9 nm after formation of a silicide layer, as a transient state between the amorphous and polycrystalline ones [193]. Above the transition thickness, the crystallite size is limited by the layer thickness and they do not exhibit a preferred growth orientation [194]. The Mo-Si interfaces are symmetric for Mo layer thicknesses <2nm, whereas asymmetric zones develop above the transition thickness due to reduced silicide formation when Si is deposited on polycrystalline Mo [189, 195].

Hydrogen-induced blistering of Mo/Si multilayers: uptake and distribution

Stress in deposited MLs can be linked to internal strain in Mo crystallites due to lattice mismatch originating during growth at the interfaces [194]. The development of stress in Mo layers within the ML structure is also strongly dependent on the layer thickness [193, 196]. Factors affecting the stress were identified as bombardment by energetic particles (inherent in magnetron deposition processes), generating biaxial compressive stress, while recrystallization introduced tensile stress. In ion-implanted Si wafers, blister nucleation is driven by the formation of passivated (001) platelets [103, 197, 198], with in-plane compressive stress and out-of-plane tensile strain inducing the layer separation [103, 151, 199]. In the current case the localization of mobile vacancies and hydrogen species and the subsequent manifestation (or not) of macroscopic blister will be determined by the stress states introduced during silicide formation at the two interfaces. Fillon and co-workers [200, 201] have demonstrated the impact of the underlying template and the layer crystallization on the development of microstructure and stress in Mo films. In the ML stack the alternating interfaces develop from a starting point of *a*-Si and polycrystalline Mo. In the former case an initially stabilized amorphous silicide layer transitions to a polycrystalline Mo form while in the latter it returns to *a*-Si. With reference to the published work in relation to buried SiGe layers, blister formation localized at the Mo-on-Si interface coupled with H accumulation at the Si-on-Mo interface point to the determining influence of compressed and tensile regions within the respective interfacial layers. The former would accumulate vacancies while tending to block thermal transport of H to deeper layers. The latter would getter hydrogen but not readily progress to the formation of macroscopic blisters.

The main effect of the ion polishing step applied to the as-deposited Si layers is the reduction of interface roughness. Since the Si layers are amorphous, ion treatment will not dramatically alter the material structure. Sufficiently high energy ion irradiation can modify the buried Si-on-Mo interface resulting in an increased interfacial thickness and chemical composition. The energy employed during the current depositions is insufficient to induce such effects. However, noble gas atoms implanted near the top of the Si layer may act as blister nucleation points and thus may contribute to the localization of blistering that we observed.

5.4.5 Effects of extended exposure

The trends in the “ion-induced” distribution shown on figure 5.4(b) and (d) indicate that the ML is prone to successive distinct stages of blistering as a result of exposure to energetic ions. The first stage ends with the initial stabilization of the D-content and the “ion-induced” blisters remain constant in terms of number density, average height, and area covered for a period after this point has been reached. Resumption of blister formation attributed to “ion-

induced” processes occurs between the 6- and 7-hour exposures. This may indicate a second fluence threshold arising from blister initiation at deeper levels in the sample. The gradual development of multi-blister structures in the “ion-induced” distribution is consistent with the emergence of new overlapping delamination points. Based on the current and previous [85] TEM cross-sections, the detachment points formed during the first 4 hours of exposure are localized at the two outermost Mo-on-Si interfaces. Slower accumulation of deuterium in deeper layers, coupled with preferential consumption by active sites in the overlaying bilayers may delay the manifestation of blistering at deeper Mo-on-Si interfaces.

The renewed blistering does not appear to coincide with an appreciable increase in the measured D-content. At best, an increase is evident after the 8-hour exposure. This suggests that the resumption of blister development is mainly the result of redistribution within the ML structure and/or that only a small fraction of the total D-content may be sufficient to induce the additional blistering stage. The fraction of incorporated atoms that ultimately contribute to blistering of silicon is typically relatively small [103]. Thus, implantation/transport of a small amount of deuterium to deeper layers could allow blister development without a substantial increase in the total content.

The rapid development of the “third distribution” blisters coincides with renewed development and growth of “ion-induced” blisters. Since the latter suggests the existence of a second ion fluence threshold, the development of the “third distribution” may be an associated ion-induced effect. One possibility is that it represents the emergence of delayed (relative to the Mo-on-Si interfaces) blister formation at the outermost Si-on-Mo interface.

5.5 Conclusions.

We have studied the correlation between D-uptake by Mo/Si ML samples and the growth and number density of blisters formed as a consequence. Hydrogen-induced blistering of these samples is complex and multi-faceted. Various blister development processes are simultaneously operative across different depth and time scales. Two distinct distributions, attributed to the effects of energetic ion irradiation and thermal H uptake, are tracked as a function of exposure time. The effects observed cannot be accounted for simply on the basis of the total hydrogen content in the sample. The number of “ion-induced” blisters is established well before stabilization of the D-content, although their size is directly correlated with it. The number of “thermal neutral” blisters is also established before content stabilization. However, these continue to grow in lateral size, via the development of blister structures of increasing complexity, even after the content has stabilized. In this case, relatively slow internal re-

Hydrogen-induced blistering of Mo/Si multilayers: uptake and distribution

distribution processes must play a more significant role in blister growth and localized transport across the ML structure is inferred.

NRA depth profiling of H-exposed samples reveals preferential retention in the Mo layers. The profiles indicate that processes induced by the minority ion fraction are competitive with direct uptake of thermal neutrals during the early stages of exposure, while thermal processes come increasingly to the fore with extended exposure time. The latter produce a strong enhancement of the H-content in the outermost Mo layer, reaching a maximum of ~19 at.%. This content is made possible by the polycrystalline nature of the Mo layer with small crystallite sizes, which allows for numerous defects, voids, and vacancies that can accommodate multiple H atoms. Preferential detachment at the Mo-on-Si interfaces together with the indication of H-accumulation at the Si-on-Mo interface is attributed to the introduction of compressive and tensile strained centres in the interfacial layers during deposition.

Extended exposures indicate that the ML structure is susceptible to successive stages of blistering via ion-induced mechanisms. These may be due to development of blisters at deeper interfaces in the samples, at the Si-on-Mo interfaces, or within the individual layers. A major challenge remains to study how the underlying processes operate in isolation and the extent of synergistic effects when the incident flux contains a mixture of neutral and ionic species.

6. Ion effects in hydrogen-induced blistering of Mo/Si multilayers

Abstract.

The role energetic (>800 eV) hydrogen ions play in inducing and modifying the formation of blisters in nanoscale Mo/Si multilayered samples is investigated. Samples are confirmed to be susceptible to blistering by two separate mechanisms. The first is attributed to the segregation of H atoms to voids and vacancies in the Mo layers, resulting in H₂ accumulation in bubbles that drives the blister formation. This process can occur in the absence of ions. A second blister distribution emerges when energetic ions are present in the irradiating flux. This is attributed to an ion-induced vacancy clustering mechanism producing vacant blisters. The defects and strained states associated with the Mo-on-Si interfaces provide the preferred nucleation points for blistering via both mechanisms. The effect of ions is ascribed to promotion of the uptake and mobility of hydrogen, in particular through the Si layers, the generation of additional mobile species in the Si and Mo layers, and to the creation of new blister nucleation points. In addition to direct stimulation of blistering via vacancy clustering, ions also modify the development of the H₂-filled blisters to produce overlapping delaminations at different interfaces. This is explained by the introduction of active transport across the Mo-on-Si interface to deeper layers. The ion-induced variations in hydrogen uptake, distribution, and nucleation create local differences in blister size and number density that produce a macroscopic pattern across the surface.

6.1 Introduction.

The interaction of hydrogen with materials is one of the most basic, yet challenging, research topics, which impacts on a wide range of application. While much is understood, there remain many open and active questions regarding the manner in which hydrogen behaves within materials. One possible outcome of the interaction of hydrogen with certain materials is the formation of blisters. Depending on the material type and composition, different exposure conditions ranging from energetic ion implantation to (plasma-)hydrogenation, or combinations thereof, can result in blister formation [152, 202, 203]. Understanding of the underlying phenomena is relevant for such diverse applications as the development of plasma-facing materials for fusion reactors [10, 180, 204-206], thin film deposition [100, 150, 157], and silicon-on-insulator layer transfer processes in the microelectronics industry [33, 152, 207, 208].

Deposited layers can exhibit a susceptibility to blistering that is typically dependent on the layer structure and composition, and on the presence of interfaces. For instance, localization of delamination can be achieved with a buried strained layers [32, 33]. Multilayer (ML) structures are extreme example of deposited layer systems in that multiple interfaces at various depths are available as potential blister nucleation sites. The formation of blisters on such structures has potential consequences for several applications, and various authors have addressed blister formation in MLs, amongst other consequences of interaction with harsh environments [105-107, 209]. In solar-cell related research, surface damage in the form of blisters and craters (collapsed blisters) has been observed upon annealing of hydrogenated Si/Ge ML structures [89, 210], while the development of microstructures has been observed in MLs for hydrogen storage [112]. Blistering has also been observed during hydrogen bombardment of ML mirrors intended for a solar research mission [87] and during hydrogenation of Co/Pd multilayers studied in the context of data storage [88].

In a previous paper [85] we reported on how the extent and type of hydrogen-induced blistering of Mo/Si ML samples was dependent on the composition of the incident flux. The individual layers are comprised of amorphous silicon (a-Si) and polycrystalline Mo, with intermixed interface layers (see Discussion). A great deal of research spanning many decades has focused on the interaction of hydrogen with these materials on an individual basis. Silicon is primarily studied in relation to the micro-electronics/semi-conductor industry and the development of solar cells technology [211, 212], while molybdenum is typically studied in the context of hydrogen-storage and for fusion and plasma-facing wall materials [213] or as part of broader investigations of hydrogen with a range of metals. An overview of some studies on hydrogen interactions with

semiconductors and metals that are relevant to the current work is provided in the following paragraphs.

The configurations of hydrogen in a-Si span a wide range of energies [214-217]. The bulk of hydrogen in an a-Si network is typically in the form of passivated dangling bonds. Due to the bond strengths involved, direct diffusion of such species is unlikely [214]. Su and Pantelides [177] suggest a floating bond-H complex as the “migrating species” while Abteu et al. [178] illustrated a “fluctuating bond center detachment” mechanism for the diffusion of hydrogen bonded within a Si network. Both mechanisms require an active site in the form of an under-coordinated Si atom for transport of H through the layer. Thus motion of hydrogen in a-Si will be determined by availability of the necessary defect structures and will ultimately be determined by only a minority of the total hydrogen in the system.

Ab initio simulations of H in a-Si and hydrogenate amorphous silicon (a-Si:H) show a strong tendency to attack strained structures in the network [212]. Formation of H₂ in large voids with excess H-content was observed. Based on studying hydrogen diffusion in nano-structured a-Si, Kail *et al* [218] proposed that molecular diffusion might be the dominant process in microcrystalline Si. Significant fractions (up to 40%) of molecular H₂ have been observed in a-Si:H films deposited by plasma-enhanced chemical vapour deposition [176, 219]. Danesh *et al* report the H₂ content of a-Si:H films with a H content near the solubility limit (~16 at.%) to be ~1 at.% [220, 221]. They proposed that that the molecular content correlates with the material properties rather than the total H-content, with 1-2% absolute H₂ content representing a limit based on film quality.

The effect of ions on a-Si can be understood in terms of their ability to introduce or remove the defect structures necessary for efficient transport of hydrogen through the network. Exposure of a-Si:H films to hydrogen plasma at elevated (>500 K) temperatures can lead to re-crystallization [222, 223]. The process is driven by structural relaxation arising from H insertion to strained Si-Si bonds and in bond-centered position between unbonded Si atoms [224]. Similarly, Sadoh *et al.* [225] reported stress relaxations of deposited SiGe layers during H⁺ implantation as a result of bond breaking. Ion irradiation-induced electronic excitation stimulated the release of hydrogen implanted in Si from simple defect complexes and resulted in diffusion and attachment to vacancies defects [226]. Subsequent annealing resulted in blister formation that was absent in the case of un-irradiated samples. Thus ion irradiation enhanced the effective mobility of H in Si by releasing it from strongly-bound configurations. The interaction of hydrogen with metals is typically dominated by the material structure. For instance, the solubility and diffusion of hydrogen in amorphous and nano-crystalline metals differs significantly from their crystalline and

polycrystalline counterparts [227-230]. The diffusion coefficient typically has a strong dependence on the hydrogen concentration, being less than that of the crystalline form at low concentrations, but increasing and exceeding the latter at higher concentrations [230].

Rigato *et al.* [110] reported negligible H retention in thick Mo layers deposited in a H₂-containing atmosphere. This was attributed to the high positive heat of solution of H in bulk Mo [181]. The only reported effect of hydrogen on Mo layers in a ML deposited in a hydrogen containing background was as slight reduction in the integrated intensity of the X-ray diffraction peak. However, trapping of hydrogen at ion-induced defects in Mo is commonly observed [231, 232]. Nagata and co-workers [233, 234] found substantial hydrogen uptake by He implanted Mo single crystal samples. Up to 20% at.% of H were found in the He saturated layer. The H trapping was associated with the nanostructure around the implanted He. In a similar vein, Hoshihira *et al.* reported significant tritium accumulation near grain boundaries of polycrystalline Mo samples after exposure to an AC glow discharge [213]. They identified two hydrogen blistering mechanisms in Mo. One involved exfoliation as a result of H accumulation at grain boundaries or clustered defects, while the other was the result of hydrogen bubble coalescence.

In general the most stable form for metal-H alloys is a defect structure containing a large number of vacancies [143]. Calculations on the configuration and binding energies of H atoms in transition metal mono-vacancies show that up to 12 atoms can be accommodated in Mo [235]. Incorporation of additional atoms resulted in H₂ formation. Based on first principles calculation, Zhou *et al.* [236] reported an increased H solubility in anisotropic strained BCC metals (W, Mo, Fe, Cr) over a wide range of both compressive and tensile values. Only over a small region of compressive strain was the solubility slightly less than that of the strain free metal. Consequently, local anisotropic strain fields of either sign could drive the segregation of hydrogen to hydrogen bubbles. This would increase the stain, stimulating further segregation resulting in a cascaded effect of bubble growth.

The current work expands on our earlier report [85] by focusing on the specific roles that energetic ions play in inducing and modifying blistering of Mo/Si MLs. The influence on ions is elucidated by studying the development of blisters as a function of exposure time and by comparing the effects of exposures performed with and without ions in the irradiating flux. The presence of two separate blistering processes is confirmed. These are attributed to H₂ bubble formation, which does not require energetic ions, and a vacancy clustering mechanism, which does. The factors that drive the localization of blisters and ion-induced modification of blister development on both a microscopic and a macroscopic scale is discussed.

6.2 Experimental.

The MLs under investigation were composed of alternating layers of molybdenum and silicon. The stack was terminated by a silicon layer. The thickness of the individual layers was ~ 3 nm for Mo and ~ 4 nm for Si. These were deposited by magnetron sputtering using in-house deposition facilities. An additional ion polishing step was applied to the Si layers in order to minimize the development of interface roughness during the course of the deposition [127, 128]. All samples were exposed to ambient atmosphere after deposition. Consequently, a native oxide layer formed the top of the outermost Si layer.

No special cleaning was applied to the samples prior to hydrogen irradiation. Samples were irradiated with the hydrogen flux generated by a thermal gas cracker (TC-50, Oxford Applied Research). Cracking occurs on the hot walls of a thin metal capillary (see [237] for more details). The cracker was mounted in an exposure chamber that was operated at a base pressure of $\sim 1 \times 10^{-8}$ mbar. It was connected to a gas line via a flow controller that allowed H_2 gas flows of up to a maximum of 2 sccm.

In the current study, the source power was kept constant (55 W) and a H_2 flow of 1 sccm was used ($\sim 2 \times 10^{17}$ mol./cm²s). The thermal cracker is nominally a source of only neutral species. However, during exposures a measurable drain current was collected by the sample. The total current varied depending on the operating condition. In the current case, the measured current was ~ 75 nA. The energy of the ions as determined using a retarding field analyzer (RFA) was predominantly in the range from 800 to 1000 eV (see Results section).

During exposures, the background pressure in the chamber was $\sim 5 \times 10^{-5}$ mbar. Samples were exposed at elevated temperatures, typically ranging from 358 K to 373 K. Details of the sample temperature during specific exposures are given at the relevant points in the Results section. Elevated temperature resulted in accelerated manifestation of blisters.

Exposures were also performed with the addition of a deflection plate close to the sample and parallel to the irradiating beam direction. By applying a bias voltage of -1100 V to this plate, charged particles were deflected from the incident flux resulting in the net current measured on the sample dropping to a fraction of a nA. The influence of ions could thus be distinguished by comparing the effects of otherwise equivalent exposures performed with biased plate (neutral only) and without the biased plate (ion+neutral).

Damage to exposed samples was evident to the naked eye prior to breaking vacuum. Post-exposure analysis required transport through air. Samples were analyzed by Optical Microscopy and Atomic Force Microscopy (AFM) to

identify and quantify structural changes to the surface. Resonant nuclear reaction analysis (NRA) utilizing the ${}^1\text{H}({}^{15}\text{N},\alpha\gamma){}^{12}\text{C}$ reaction was used to produce depth profiles of the H-content of selected samples. Subsequent elastic recoil detection (ERD) analysis was also performed in order to estimate the total hydrogen content. The ERD measurements were performed by AccTec BV using a 3.5 MV particle accelerator (singeltron type). The depth resolution of the ERD analysis was ~ 30 nm.

6.3 Results.

6.3.1 Ion flux profiles

The primary focus of this report is on the role that ions play in inducing blisters in ML structures. Therefore we begin by presenting some details of the ion profiles that were generated by our source. Figure 6.1(a) shows ion energy profiles measured along the central axis of the source. Most ions have an energy in the range from 800-1000 eV. Two distinct peaks appear in this range, one centered at ~ 860 eV and one at ~ 1000 eV. The capillary is heated by an electron flux that is accelerated from a hot filament to a biased (+1000 V) capillary (see [237]). Thus the ion energies measured are consistent with repulsion of ions

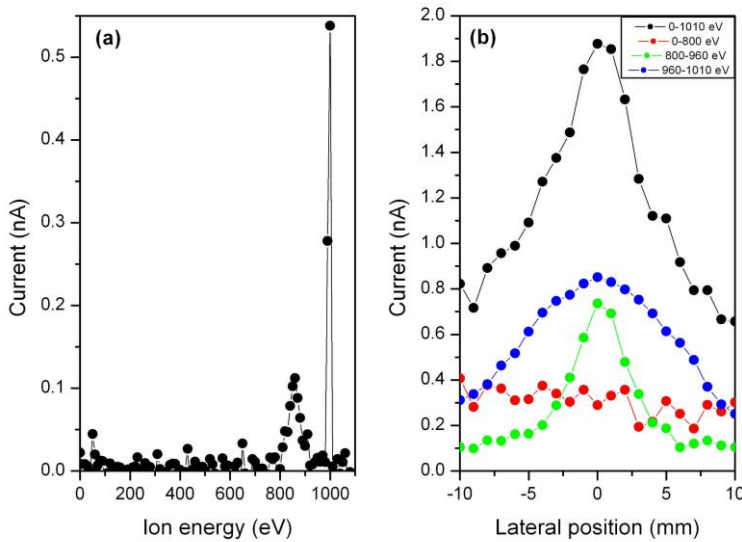


Figure 6.1: Ion energy and current profiles from the capillary cracker a for H_2 gas flow of 1 sccm. (a) Ion energy measured along the central axis position of the capillary cracker beam, (b) Ion currents for selected beam energy ranges as a function of lateral distance from the central axis position.

Ion effects in hydrogen-induced blistering of Mo/Si multilayers

created in the vicinity of the capillary. The origin of the two peaks is not obvious. However, comparison of their lateral intensity profiles (see below) suggests that the 860 eV peak may be due to ionization of particles in the direct flow from the capillary cracker while the 1000 eV peak may be due to ionization of background hydrogen. The former would imply a mixture of atomic and molecular ions, while the latter would be primarily molecular ions. The current density in the centre of the hydrogen beam was ~ 100 nA/cm². However, the ion flux was not uniform across the sample surface. Figure 6.1(b) shows lateral ion flux profiles derived from RFA measurements. The total ion profile (0-1010 eV) has a maximum in the center of the beam and decreases towards the periphery. Individual profiles for the energy ranges <800 eV, from 800-960 eV, and from 960-1010 eV are also plotted. The <800 eV profile is essentially flat, the 800-960 eV profile is strongly peaked along the beam axis, while the 960-1010 eV has a broad peaked distributions.

6.3.2 Blister formation during ion+neutral exposures.

Direct exposure of samples to the unmodified hydrogen flux from the capillary cracker resulted in the development of distinctive circular damage patterns on the surface as a function of exposure time. The effect is illustrated in Figure 6.2(a) and (b), which show photographs of $\sim 12 \times 12$ mm² samples taken following 3-hour and 5-hour exposures, respectively. The sample temperature during these exposures ranged from ~ 298 -358 K. This range was the result of direct heating from the thermal cracker. At the start of an exposure the sample was at room temperature. After ~ 45 minutes the temperature was stable at ~ 358 K.

The images in Figure 6.2 correctly reproduce the damage patterns that were discernable by eye, although the photographic method exaggerates the contrast between different regions. The apparent color is also an artifact of the photographic method; to the naked eye the damaged areas appear whitish. The area indicates as “deposition clamp” represents a region of bare Si wafer, which was exposed to the hydrogen flux, while the “exposure clamp” is a region of deposited ML that was covered during the exposure.

For the purposes of the current work the damage pattern observed can be divided into three regions. In Figure 6.2 these are characterized as a “central spot”, an “intermediate ring”, and a “periphery region”. On both samples the central spot had the appearance of being the most severely damaged. The periphery region exhibited a diffuse discoloration that was less intense than that of the central spot. The intermediate ring was the slowest to exhibit visible damage. After 3 hours this portion of the surface retained its original mirror-like reflectivity and by eye appeared unaffected by the exposure.

Inspection of the samples using white-light interferometry and AFM revealed the presence of blister-like structures in all three regions of both samples. Thus, blisters were also present in the “intermediate ring” after the 3-hour exposure, although both their size and the number density were very small, indicating that the manifestation of macroscopic blisters has only commenced.

The $25 \times 25 \mu\text{m}^2$ AFM images that were shown in [85] were collected from the central spots of the two samples shown in Figure 6.1. Figure 6.3 shows $5 \times 5 \mu\text{m}^2$ AFM images collected from the periphery regions ((a) and (c)) and the central spots ((b) and (d)) of these samples. After the 3-hour exposure (Figure 6.3(a) and (b)) the blisters in the two regions appear similar, although those in the periphery are somewhat larger than those in the central spot. After the 5-hour exposure the blister density in the periphery is essentially unchanged but the individual blisters have increased in size (Figure 6.3(c)). In contrast, the number density of blisters in the central region has increased dramatically due to the emergence of a large number of comparatively small blisters (Figure 6.3(d)). The central spot now contains fewer blisters that are of comparable size to those evident in the periphery region of the same sample. Thus, although both regions exhibit a continued growth of existing blisters when the exposure time is extended, the growth rates differ significantly. This difference can be attributed to the influence of ions on the blister growth (see Discussion).

TEM images shown in [85] illustrate that blistering is the result of delamination occurring at the two outermost Mo-on-Si interfaces. Thus far no instance of delamination at a Si-on-Mo interface or at deeper Si-on-Mo interfaces has been observed. Instances of “double-blisters” structures are also visible in Figure 6.3(d) (see red arrows). Such structures arise from overlapping delaminations occurring at different Mo-on-Si interfaces [85]. They were only observed in the central spot after the 5 hour exposure.

The blisters seen in Figure 6.3(a)-(c) are consistent with a single size distribution. The presence of two distributions occurs only in the central spot after the 5 hour exposure. As outlined in [85], the two distributions could be distinguished on the basis of their relative size and their aspect ratio (e.g. radius to Z-height), with the larger of the two being attributed primarily to the uptake of neutral hydrogen and the smaller to direct ion-induced processes. Throughout this manuscript, these two distributions will be referred to by the short-hand labels “thermal neutral” and “ion-induced”. The validity of these labels will be considered in light of the results presented.

Ion effects in hydrogen-induced blistering of Mo/Si multilayers

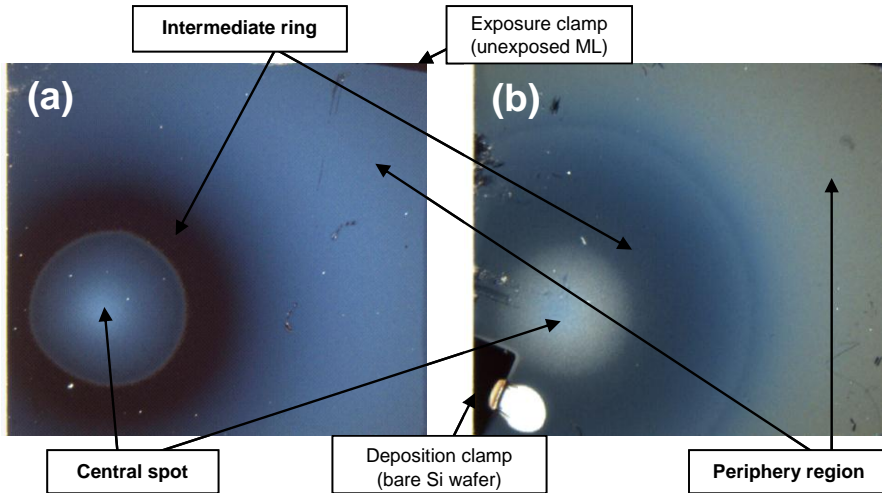


Figure 6.2: Optical images of $\sim 12 \times 12 \text{ mm}^2$ ML samples after exposure for (a) 3 hours and (b) 5 hours to the unmodified hydrogen flux from the thermal capillary cracker at 1 sccm H_2 flow. ($T_{\text{exposure}} \sim 298\text{-}358 \text{ K}$.)

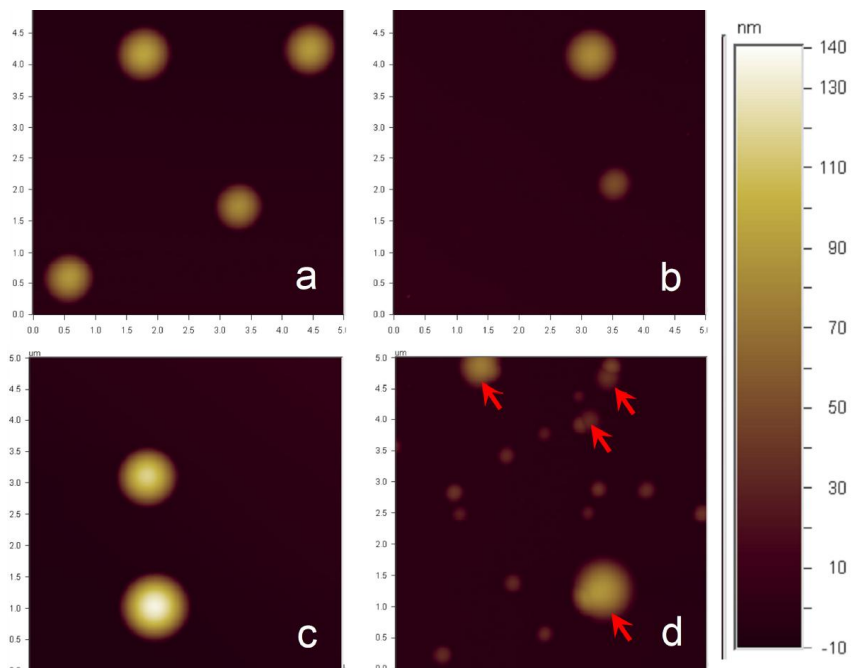


Figure 6.3: $5 \times 5 \text{ }\mu\text{m}^2$ AFM images collected from (a) the periphery and (b) the central spot of the sample shown in figure 2(a) (3-hour exposure); and from (c) the periphery and (d) the central spot of the sample shown in figure 2(b) (5-hour exposure). The red arrows on panel (d) indicate “double-blister” structures. The Z-scale is common to all images.

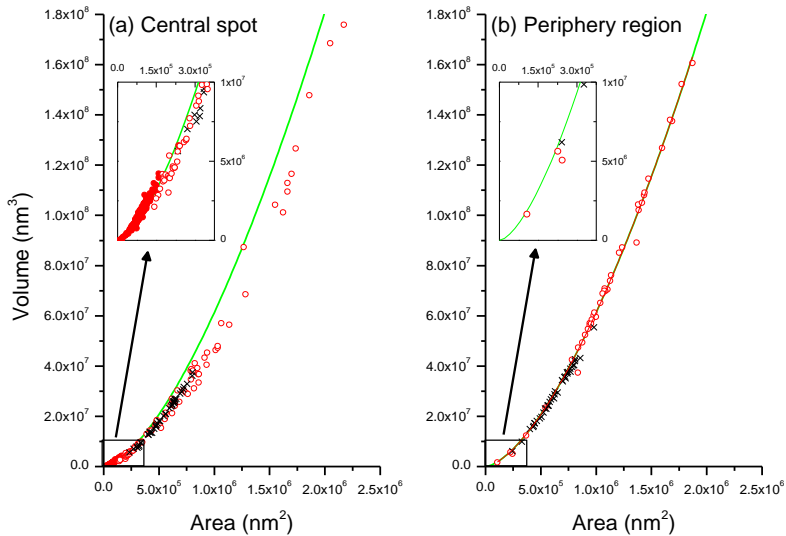


Figure 6.4: Plots of blister volume versus surface area covered by individual blisters derived from $25 \times 25 \mu\text{m}^2$ AFM scans: (a) central spot and (b) periphery region. The data from the samples exposed for 3 and 5 hours are indicated with black crosses and red circles respectively. In the case of the 5-hour exposure data, filled circles indicate “ion-induced” blisters and open circles indicate “thermal neutral” blisters. The green trace is obtained by fitting the 5-hour exposure data in the periphery region with the function: $y = a \times (x^b)$. The insets on the two panels are blow-ups of the dimension range containing the “ion-induced” blisters.

Figure 6.4 shows plots of individual blister volume versus area covered derived from $25 \times 25 \mu\text{m}^2$ AFM scans collected from the samples shown in Figure 6.2. Figure 6.4(a) shows data from the central spot and Figure 6.4(b) from the periphery region. The solid line in both panels is the result of fitting the data points derived from the scan of the periphery region after the 5 hour exposure with an equation of the form: $y = a \times (x^b)$. This trace is reproduced on both panels as a reference curve to aid comparison between the datasets. The data from the periphery region after the 3 hour exposure also exhibit a good correlation with this curve. Thus, in the periphery region the main effect of increasing the exposure time is an increase in blister size. All blisters in this region are classified as “thermal neutral”.

The blister distribution in the central spot after the 3-hour exposure is comprised of symmetric single-component structures that are qualitatively similar to those in the periphery region. However, they are on average smaller

than those in the periphery and are “flatter”, as is indicated by their position relative to the reference curve. These blisters are also classified as “thermal neutral”.

Divergence of the blister development in the central spot after the 5-hour exposure is clearly evident from Figure 6.4(a). While some of the “thermal neutral” blisters in the central spot exhibit significant growth, the majority remain clustered at sizes similar to those present after the 3 hours. There is increased scattering in the data points, but all remain below the reference curves. The addition “ion-induced” blisters that have emerged have individual areas of $<2 \times 10^5 \text{ nm}^2$. They lie above the reference curve, indicating that they are generally “taller” than the “thermal neutral” blisters in aspect ratio terms. Also evident from the insets is that a significant number of additional “thermal neutral” blisters have developed in the central spot after 5 hours as compared with the 3-hour exposure. A similar effect is not evident in the corresponding periphery region data.

6.3.3 “Ion+neutral” versus “neutral-only” exposures.

To test the assignment of “thermal neutral” (neutral flux) and “ion-induced” (energetic ions) blister distributions, exposures performed without and with utilization of the biased deflection plate were compared (hereafter referred to as “ion+neutral” and “neutral-only”, respectively). Figure 6.5 shows optical images taken after 5-hour exposures of samples to (a) the ion+neutral flux and (b) the neutral-only flux. The most obvious result of the neutral-only exposure is the absence of a circular damage pattern. Note that between these exposures and those shown in Figure 6.2, the cracker-sample distance had been increased by ~50 mm. This reduced direct heating of the sample by the source. Instead, active heating was applied via a rear-mounted filament and the sample temperature was stabilized at 373 K before the start of the exposures to ensure constant exposure conditions. Thus the different damage patterns seen in Figure 6.2(b) and Figure 6.5(a) are to the result of differences in the incident flux and the exposure temperature.

Comparison of AFM images collected from the central spot and periphery regions of the samples shown in figure 6.5 show that the “ion-induced” distribution is present in the central spot after the ion+neutral exposure but is absent after the neutral-only exposure. Thus, the attribution of these features is confirmed. In addition, in the latter case all the blisters (“thermal neutral”) that do develop exhibit a single-component structure, whereas all “thermal neutral” blisters in the central spot after the ion+neutral exposure have a double- or multiple-component structure. Consequently, the development of such structures is also attributed to the presence of energetic ions in the irradiating flux. In the case of AFM images collected from the periphery regions of the

samples, a single distribution of single-component blisters is observed in both cases.

Figure 6.6 shows plots of individual blister volume versus area covered derived from $50 \times 50 \mu\text{m}^2$ AFM scans of the samples shown in Figure 6.5. The reference curve from Figure 6.4 is again reproduced in these panels. Figure 6.6(a) compares the data from the central spot regions of the two samples. The “ion-induced” distribution is represented by the high density of points with area $< 8 \times 10^5 \text{ nm}^2$. These blisters are much larger than the corresponding blisters in the central spot of the samples shown in figure 6.2(b). There are few features in this size range on the sample exposed without ions.

The development of multi-component blisters in the central spot when ions are present versus single-component blister when they are absent is again apparent from the relative scatter in data points for blisters designated as “thermal neutral”. For these exposures the presence of ions leads to an increase in the average blister size of these blisters both in volume and area covered relative to when ions are absent. Similar to the case for Figure 6.4(a), “ion-induced” blisters tend to lie above the reference curve. “Thermal neutral” blisters tend to lie below the reference curve after the ion+neutral exposure, while they have a reasonably good correspondence with it after the neutral-only exposure.

In the periphery region both samples exhibit only single-component blisters, which is apparent from the uniformity of the volume versus area data points shown in Figure 6.6(b).

Both datasets have a good correspondence with the reference curve. However the blisters that develop in this region are significantly smaller when ions are present compared to when they are absent. After exposure to the ion+neutral flux the blisters in the periphery region are also significantly smaller than the “thermal neutral” blisters in the central spot of the same sample. This is in marked contrast to the sample shown in Figure 6.2(b) where the “thermal neutral” blisters are larger in the periphery region. In contrast, the blisters distributions in the periphery and central spot regions of the sample exposed to the neutral-only flux are very similar to each other.

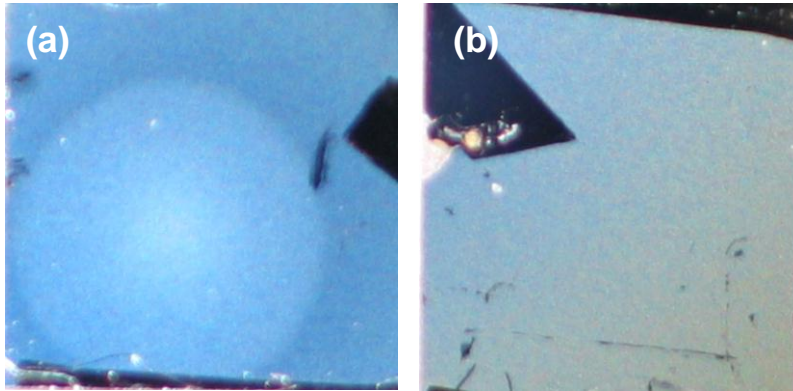


Figure 6.5: Optical images of $\sim 12 \times 12 \text{ mm}^2$ ML samples after exposure for 5 hours to (a) the “ion+neutral” and (b) the “neutral-only” flux from the thermal capillary cracker at 1 sccm H_2 flow. ($T_{\text{exposure}} \sim 373 \text{ K}$.)

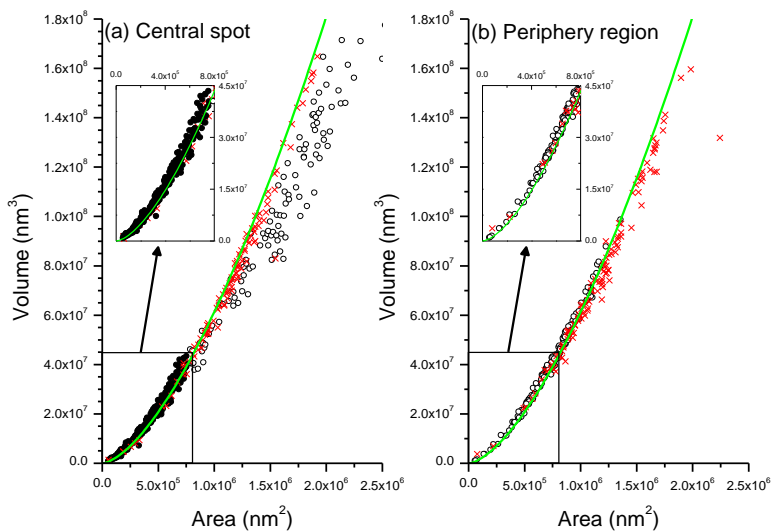


Figure 6.6: Plots of blister volume versus area covered by individual blisters derived from $50 \times 50 \mu\text{m}^2$ AFM scans of (a) central spot and (b) periphery region of the samples shown in figure 5. Black circle and red crosses indicate data from the sample exposed to the “ion+neutral” and “neutral-only” fluxes, respectively.

In the case of the “ion+neutral” data, “ion-induced” blisters are indicated by filled circle and “thermal neutral” blisters by open circles. The green trace is a reproduction of the curves show in figure 4. The insets on the two panels are blow-ups of the dimension range containing the “ion-induced” blisters.

6.3.4 H-content and depth profile

Figure 6.7 shows a comparison of resonance NRA H-content profiles measured in the central spot region of the samples shown in figure 6.5. The oscillatory profile with enhanced H-content in the Mo layers relative to the adjacent Si layers was reported previously [238]. There H-content in the outermost Si and Mo layers was elevated in the case of the neutral-only exposure as compared with the ion+neutral exposure. However, post-NRA determination of the total H-content in these samples by ERD yielded H concentrations of $\sim 1.4 \times 10^{16}$ at/cm² and $\sim 1.13 \times 10^{16}$ at/cm² in the outermost ~ 30 nm of the samples exposed to the ion+neutral and the neutral-only fluxes, respectively. Thus, ERD indicates that the H-uptake is increases by $\sim 24\%$ when ions are present, whereas the NRA data showed an enhancement of the local content in the outermost

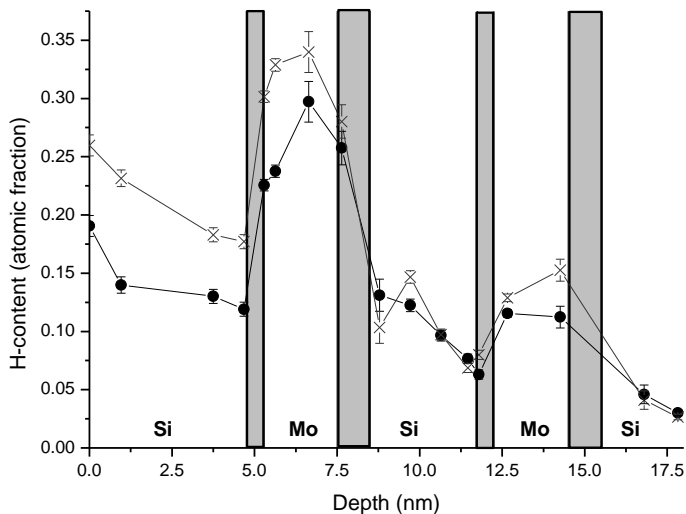


Figure 6.7: Resonant NRA depth profiles of the H-content of samples after exposure to the “ion+neutral” (circles) and “neutral-only” (crosses) fluxes from the thermal capillary cracker. The approximate layer structure is indicated. The grey regions represent interfacial zones.

layers when they are absent. Alteration of the content as a consequence of the successive post-exposure beam analyses cannot be ruled out, although there was no indication of instability in the H-content of either sample during the course of the ERD measurements. A possible cause of the discrepancy is that ions are promoting not only hydrogen uptake, but also enhancing its distribution and localization within the ML structure. Enhanced localization would be consistent with the increased blistering that is observed when ions are present. This should not affect the total content measurement derived from ERD, but depending on the degree of localization as a function of depth could potentially result in an

under-estimation by the point-wise resonant NRA measurements. In particular, gaseous H₂ trapped in blisters might be under-estimated by resonant NRA.

6.4 Discussion.

Before addressing the specific results presented in this paper, we first outline the likely effects of hydrogen in general and ions in particular on the type of samples under investigation. It is important to bear in mind that we are dealing with materials that are constrained by the nanometer scale thickness of the individual layers. The constraining of materials within thin layered structures can have a dramatic impact on the interaction with hydrogen [239]. The behavior of such systems cannot necessarily be inferred from bulk material properties. The H-related properties of the ML will be determined by the local strain states in the individual layers, the presence and density of defect sites and (self-)interstitials, the level of intermixing between individual layers and the crystallinity (and crystal size) of the layers. These parameters will be dependent on the precise details of the deposition procedures and composition of the layers. For instance, the vessel residual gas during deposition can have a significant influence on the native H-content and layer stress values of deposited Mo/Si layers [169].

The structural and compositional details of Mo/Si MLs have been extensively investigated [67, 70, 128, 194]. The Si layers are amorphous, while the Mo layers are polycrystalline. Since the Mo crystallite size is determined by the layer thickness [194], the Mo layers can be characterized as highly defective polycrystalline or nano-crystalline layers. Given the small layer thicknesses involved, the material properties tend to be dominated by interfacial effects. An intermixed Mo-Si zone is formed at both interfaces during deposition. The interfacial regions are asymmetric with a thicker layer growing at Mo-on-Si interfaces than at Si-on-Mo interfaces [128, 189]. This effect is primarily related to the crystallinity of the Mo layers. When Mo is deposited on a-Si an amorphous-to-polycrystalline phase transition occurs at a critical thickness of ~1nm [189, 193]. The point of transition is determined by the Si-content in the intermixed layer and can be postponed by depositing Mo layers with a small Si content [200, 201]. In the case of the Si-on-Mo interface, Si is deposited on poly-crystalline Mo. This hinders intermixing and results in a more rapid transition to the a-Si phase.

The deposited layer structures typically have significant internal stresses that arise due to the lattice mismatches at the interfaces. Since the layers are very thin, the individual materials do not relax back to their bulk properties before a new interface is initiated. Stress measurements based on wafer curvature indicates that the Si layers produce compressive stress (i.e. they are tensilely-strained in-plane) while the Mo layer produce tensile stress (compressively-

strained in-plane) [161]. These macroscopic effects are determined by localized effects on the atomic scale, particularly those occurring in the interfacial regions where the effects of lattice mismatches are at their greatest [194].

Interfaces can play a significant role in the context of hydrogen retention. Okada *et al* reported H trapping at an Au/Ir interfaces with was attributed to lattice relaxation of the strained Au layer [162]. Noble gas atoms, which become incorporated in a-Si layers during magnetron sputter deposition [110], can also act as defects that promote hydrogen accumulation. The application of post-deposition ion polishing of the Si layers in order to control deposited layer roughness and interface mixing of deposited layers [109, 240] will enhance the number of noble gas atoms incorporated at the top of the Si layer (i.e. in the vicinity of the Mo-on-Si interfaces).

The effect of hydrogen in the ML will be dominated by the local chemical and structural composition and the associated lattice strains. Before addressing how ions impact blister development in the current exposures, we will first sketch a scenario for blistering under neutral-only conditions. The uptake of hydrogen in the neutral-only case will be determined by the “natural” availability of dangling or stressed bond centers in the outermost Si layer. In the first instance the majority of hydrogen will go to passivating dangling bonds resulting in a H-content that is effectively static. A small fraction of the total hydrogen in the layer will be “mobile” and will mediate transport to deeper layers. The diffusion of hydrogen in the Mo layer will initially be hindered by the presence of deep defect trap sites. However, it will increase with increasing H-content and become orders of magnitude faster than in a-Si. Thus the rate of vertical penetration of hydrogen through the structure will be determined primarily by the Si layers, while lateral redistribution of hydrogen will be mediated via the Mo layer.

Exposure to the neutral-only flux results in an elevated H-content primarily in the outermost Si (~0.18 at.%) and Mo (~0.34 at.%) layers (Figure 6.7). The content of the Si layer is comparable to the levels that were attained by deposition in a H-containing atmosphere [110] and by post-deposition ion treatment of Si layers [109]. The high content in the Mo layer can be attributed to the tendency for hydrogen to stabilize and accumulate in vacancies in the structure [235]. Segregation of multiple H-atoms to Mo mono-vacancies is energetically favorable and can lead to H₂ production. Given the positive heat of solution of hydrogen in Mo and the tendency for H₂ formation in high H-content vacancies, it seems likely that segregation of H₂ molecule drives the formation of “thermal neutral” blisters. As will be discussed below, the ion-induced conversion of “thermal neutral” blisters from single- to multi-component structures may represent an indirect indication of H₂ in these features.

The comparatively low H-content in the first buried Si layer suggests slow or hindered transport across the intervening Mo-on-Si interface. Macroscopic blistering in the case of neutral-only exposures appears to be exclusive to this interface. Relaxation of the compressive strain on the Mo layers, which is further increased by hydrogen incorporation, may be a driving force in this process. The highly localized formation of blisters may indicate a stress-driven cascaded effect such as that proposed by Zhou *et al.* [236] where the anisotropic strain produced by bubble formation facilitates further bubble growth by enhancing H solubility.

In light of the overview of the interactions of hydrogen with a-Si and metals given in the Introduction, the main effect that can be anticipated due to the presence of energetic ions in the irradiating flux are as followed:

- Ions will enhance the diffusion of hydrogen within and through the Si layers as a consequence of cleavage of existing Si-Si or Si-H bonds within the network, producing under-coordinated Si atoms that facilitate transport. Related to this, the energetic ions can facilitate uptake of hydrogen by producing reactive trapping sites at the surface. Ion-enhanced uptake is consistent with the ERD contents measured, while the lower H-content in the outermost Si layer is indicative of enhanced mobility within the network.
- The main effect of ions on the Mo layers is likely to be the creation of lattice defects and implantation that can act as trap sites for hydrogen and potentially lead to void formation. Ion-enhanced segregation of hydrogen to voids and vacancies (including macroscopic blisters) may account for the lower H-content in the “bulk” of the Mo layer that is seen in NRA profile of the “ion+neutral” sample.
- In the interface layer the influence of energetic ions is likely to be a combination of its effects on the pure layers. Defects and implantation can introduce new trap sites, while cleavage of Si bonds will aid transport within and across the interfacial zones and may also allow relaxation of stressed bonds within the network.

We can now address the following specific features of the current results:

1. The appearance of the “ion-induced” distribution;
2. The development of the double-/multiple-blister structures in the “thermal neutral” distribution;
3. The lateral damage pattern and related effects.

1. The appearance of the “ion-induced” distribution

At the most basic level, the appearance of the second distribution is due to the introduction of new blister nucleation sites in the ML structure. This can be in the form of defect creation (vacancies or self-interstitials) or from the direct implantation of ions. The ability of defects introduced in materials by ion irradiation to accumulate hydrogen is well-established. Induced defects and implantation can occur across the entire region probed by the penetrating ions. None-the-less, macroscopic blister formation remains localized in the vicinity of the Mo-on-Si interfaces. Thus their manifestation must be determined by local structural properties of the layers, with the Mo-on-Si interface clearly providing the preferred site for blister development.

It is noteworthy that, despite their common detachment point, the “ion-induced” and “thermal neutral” blisters distributions remain structurally distinguishable from each other. This suggests different underlying mechanisms of blister growth. The different mechanism of bubble formation that can occur in metals are near-surface plastic deformation (“blistering”), dislocation loop punching, and vacancy clustering [102]. The former two involve gaseous H_2 accumulation in bubbles, while the vacancy clustering mechanism can produce voids with low molecular hydrogen content. This mechanism has been observed in ion-irradiated Mo [102]. It involves the nucleation of hydrogen-vacancy (HV) complexes into a higher H_xV_y complex that acts as the bubble nucleus. Vacancies formed by hydrogen ion irradiation are also stabilized by hydrogen, preventing their recombination with metal interstitials. Hence, this is a plausible mechanism for the development of the “ion-induced” blisters in the current samples.

As was noted in relation to figure 6.4(a), the number of “thermal neutral” blisters in the central spot increased when the exposure time was extended from 3 to 5 hours, an effect that was not observed in the periphery region. The implication is that the ion irradiation also induces the development of additional “thermal neutral” blisters. Hence, defects introduced by the energetic ions were not restricted to inducing only one type of blister. Local strain states will be the determining factor in the type of blister that is formed by a given induced defect. Zhou *et al* [236] suggest that H-solubility in bcc metals could be enhanced by anisotropic strain almost irrespective of the sign, thereby facilitating a cascade effect of bubble formation. None-the-less, the effect as a function of applied strain was more pronounced for tensile strain values. In contrast, vacancy accumulation is energetically favorable in regions with compressive strain. Consequently, on the basis of H_2 accumulation driving the “thermal neutral” blistering and vacancy clustering driving the “ion-induced” blistering, these processes would be preferentially associated with localized tensile and compressive strain centers, respectively. The existence of atomic scale regions

Ion effects in hydrogen-induced blistering of Mo/Si multilayers

with opposite strain values in the Mo-on-Si interface is possible given the variations in material, composition and crystalline state that occur during the transition.

2. The development of the double-/multiple-blister structures

Multi-component thermal neutral blisters are due to overlapping delaminations occurring at different Mo-on-Si interfaces [85]. The apparently universal conversion of these blisters from single- to double-/multiple-component blisters in the presence of ions is remarkable. It is inconsistent with a random process in which the individual components develop independently of each other. Rather, it suggests a direct connection between components. The immediate implication is that ions are inducing the transport of hydrogen across the layered structure. This can be mediated by the formation of active trapping sites at the lower surface of the initial single-component blister. However, efficient transport also requires a ready reservoir of material to be transported. Gaseous H₂ in the initial blister is a candidate for such a reservoir. An indirect suggestion of the presence of H₂ in the gas phase can be inferred from the volume-area plots shown in Figures 6.4 and 6.6. In all cases the presence of ions in the irradiating flux results in a decrease in the volume of “thermal neutral” blisters relative to their area. This is the case even when the blisters still exhibit a single-component structure (Figure 6.4(a); 3 hour exposure data). Reduction of internal pressure via the transport of H₂ to deeper layers would account for this effect.

3. The lateral damage pattern

Before discussing the origin of the lateral damage pattern, it is useful to consider the likely flux profiles of the particles that were incident on the samples during the exposures. Details of the ion profiles generated by our source have been presented in the Results section. The neutral profiles have not been measured. However, several reports on the typical profiles of capillary cracker-type sources have been published [129-131]. The generic characteristics detailed in those studies will also be valid for the current source. The neutral particle profiles from capillary sources are typically peaked on-axis. However, depending on the capillary dimensions and operating conditions, an on-axis dip can develop in the H-atom profile. None-the less, the blistering damage in the case of the current neutral-only exposures is uniform. This uniformity suggests either a relatively flat flux profile or a high effective lateral mobility of the hydrogen that segregates to macroscopic blisters. In any case, the neutral flux profile is not the critical factor in the development of the observed damage patterns.

The concentric damage pattern was only evident when the ion+neutral flux was used. It appears that the energetic ions (>800 eV) are responsible for the

development of this pattern, since the ions in the 0-800 eV range have a flat lateral profile. Furthermore, comparison of the diameters of the central spots seen in Figures 6.2 and 6.5(a) with the intensity profile widths shown in Figure 6.1(b) suggests that ions in the 800-960 eV range are the most critical for the development of the damage pattern. As mentioned in the results section, their relatively sharp lateral profile may indicate ionization of particles in the direct flow from the capillary, implying a significant fraction of atomic ions.

The macroscopic damage pattern that develops during ion+neutral exposures is a consequence of the lateral variations in blister height and number density across the surfaces. This is related to the impact of energetic ions on the density of local blister nucleation sites. However, while the ion profiles shown in Figure 6.1(b) are either flat or have simple peak shape, the blister formation as a result of ion+neutral exposures is not a simply linear function of the distance from the center of the beam spot. Thus, the individual ion profiles are also insufficient to explain a pattern development in which the intermediate ring can be the slowest to manifest blisters. To account for such a pattern, an inter-play between different processes or between the effects of different incident species must be invoked.

Three ion-influenced factors affect the rate at which macroscopic blisters appear. These are the rate of hydrogen uptake by the ML, the rate of transport to the blister nucleation sites and the local density of active nucleation sites. The presence of ions can enhance all three factors, with the effect being dependent on the local flux and composition of the incident species. As outlined above, energetic ions can enhance the uptake and transport rate in a-Si leading to more rapid development of blisters. However, stimulation of the second blistering mechanism by energetic ions will have a counter-acting effect, with the increased number of sites consuming available hydrogen slowing the development of individual blisters.

The enhancement of hydrogen uptake and distribution will be related to the local ion flux. The rate of initiation of “ion-induced” blisters will also be flux dependent. However, there is a limit to the number of “ion-induced” blisters that can be formed [238], which is established before the hydrogen content of the samples has stabilized. This means a shift from primarily site creation/activation during the early stages of exposure to predominately blister growth during the later stages. With increasing number of active blister sites, the increased competition for available hydrogen will tend to hinder the emergence of new blisters. This will particularly be the case if the cascade effect proposed by Zhou *et al* [236] is operative.

The combination of locally varying uptake and transport rates, blister nucleation site densities, and a flux/fluence dependent transition from dual active processes

(new blister initiation and blister growth) to a single active process (growth only) easily provide sufficient variables to account for a complex lateral variation in the rate of blister development. However, the comparison of ion+neutral and neutral-only exposures provides an indication that an additional factor, namely lateral redistribution, may also be operative. This is based the variations in blister number density and volume as a function of distance from the central spot, as is shown in figure 6.8. This figure compares (a) the blister count, (b) the total volume occupied by blisters, and (c) the average volume occupied per blister for the neutral-only and ion+neutral exposure, with the “ion-induced” and “thermal neutral” distributions being analyzed separately in the latter case.

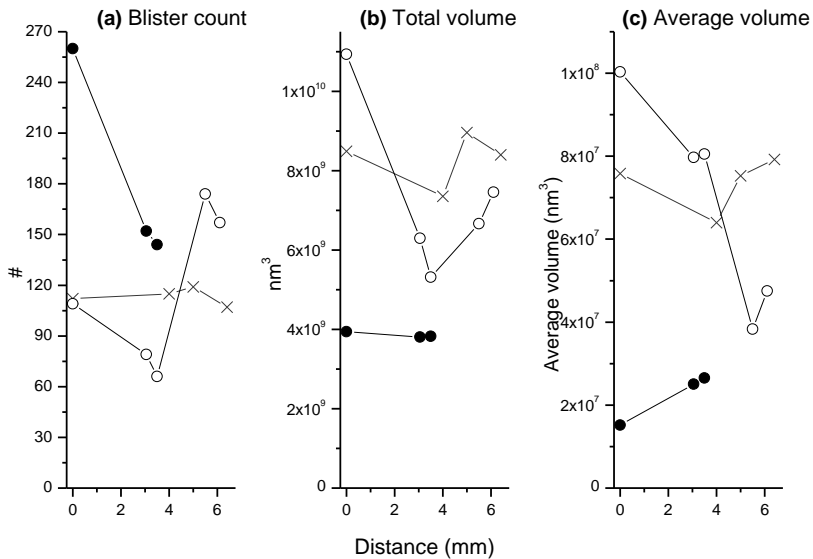


Figure 6.8: Plots of (a) blister count, (b) total blister volume, and (c) average blister volume derived from $50 \times 50 \mu\text{m}^2$ AFM scans of after exposure to the “ion+neutral” (circles) and “neutral-only” (crosses) fluxes from the thermal capillary cracker. In the case of the “ion+neutral” exposure, data from the “ion-induced” and “thermal neutral” distributions is indicated by filled and open circles, respectively. The x-axis values are referenced to the approximate centre of the “central spot” position.

The most interesting feature is the large variation in the total and average volumes of the “thermal neutral” blisters in the case of the ion+neutral exposure. Both decrease with increasing distance from the centre to the outer part of the central spot region, which can be attributed to an ion-flux dependent enhanced of the local uptake and transport of hydrogen. However, in the periphery region the average volume occupied by a “thermal neutral” drops below that of blisters in the same region after the neutral-only exposure, in spite of there being

ostensibly no direct ion-induced effects operative in this region. A possible explanation is enhanced (hindered) lateral transport of hydrogen toward (away from) the central spot region. It should be stress that, given the number of variables at play during the blistering of ML sample, drawing a definitive conclusion regarding the role (if any) of lateral re-distribution is difficult, at best. This is not least the case because, as shown in figure 8.1, ions in the 960-1010 eV range are incident on the periphery region during ion+neutral exposures. Thus, the size variation of blisters in this region might be the result of different ions (e.g. atomic versus molecular) having differing effects on the interaction of hydrogen with the ML.

6.5 Conclusions.

Based on the comparison of the effects induced by exposure to incident neutral-only and ion+neutral exposures, an outline for two mechanisms leading to the development of two distinct blister distributions on nano-scale Mo/Si MLs has been proposed. The first involves hydrogen accumulation in voids and vacancies leading to the formation of H₂-filled bubbles. This can occur in the absence of ions and is driven by the energetically favorable segregation of hydrogen to vacancies in Mo. The second mechanism is a H-V clustering process that require energetic ions to produce the initiating stable vacancy complexes. Both processes lead to the formation of blisters that are localized at the Mo-on-Si interfaces. This localization is attributed primarily to localized strain centers and defects that develop during the formation of these interfaces and during subsequent ion irradiation. In addition to stimulating the vacancy clustering mechanism, energetic ions also promote the uptake and distribution of hydrogen within the ML. These effects are particularly relevant to transport across the Si layers. The formation of overlapping blister structure with delamination at different Mo-on-Si interfaces is attributed to ion-induced transport of trapped H₂ molecules across the layered structure. Finally, the emergence of concentric damage patterns during ion+neutral exposures as a result of lateral variation in blister size and density is attributed to local (flux- and fluence-dependent) variations in ion-induced uptake, distribution, and nucleation of hydrogen.

7. Temperature dependence of hydrogen-induced blistering of multilayered films.

Abstract.

We report on the effect of sample temperature on the development of hydrogen-induced blisters in Mo/Si multilayer thin films. Comparison is made between a mixed flux of hydrogen ions and neutrals and a flux of only neutrals. At low exposure temperatures ($<100\text{ }^{\circ}\text{C}$) ions were necessary to promote the formation of blisters, which develop in two distinct distributions. At higher temperatures a neutral-only flux was sufficient to induce one of these distributions, the growth of which was retard by the presence of ions. Ions also promoted the transport of blistering precursors to deeper layers resulting in the development of “multi-component” blister structures. In many cases these structures represent a modification of the blister distribution that develops in the case of neutral-only exposure. The ion-induced effects become less evident with increasing exposure temperature and at $200\text{ }^{\circ}\text{C}$ the only discernible effect is the stunted growth relative to neutral-only exposures.

Sample temperature during exposure was found to have a stronger effect than pre- and post- exposure annealing. A tentative explanation is given including effects of ion-induced sequestration and redistribution within the ML structure.

7.1 Introduction.

Hydrogen-induced blistering of materials is a complex phenomenon [102] that can have a strong dependence on the exposure conditions. Sample temperature is one of the critical parameters. The temperature dependence of blister formation is an open issue in fusion research where hydrogen retention [241-244], hydrogen-induced blistering, and other types of surface damage [10, 245, 246] to plasma-facing materials are being investigated. In the field of thin films, blister and crater formation occurs during annealing of hydrogenated Si-Ge multilayer (ML) structures [89]. The selection of appropriate annealing/exposure temperature is important for the process optimization in thin layer transfer techniques (Si-on-insulator technology) [153, 247-251].

In the case of hydrogen-induced blistering in Mo/Si ML coatings with nano-scale film thicknesses [85, 252] two separate blistering processes have been observed. They are attributed to H₂-filled blisters induced by thermal hydrogen species (or ‘thermal neutral’ process) and –the formation and clustering of hydrogen-vacancy complexes induced by relatively energetic (100’s of eV) ions (‘ion-induced’ process). Such ions also modify the development and growth of blisters induced by thermal hydrogen.

A preliminary study on the temperature dependence of blister formation in Mo/Si MLs was reported in [86]. The current manuscript extends beyond those results based on atomic force microscopy (AFM) data of blistering formed at various temperatures and includes data on exposures to a flux of neutral-only hydrogen in order to evaluate the effect of the presence of ionized hydrogen species in the beam. Increasing the sample temperatures (up to ~200 °C) for a fixed exposure period resulted in larger individual blisters and a smaller area number density. The effects of pre-annealing of the samples prior to hydrogen exposure as well as post-annealing are discussed.

7.2 Experimental.

The Mo/Si ML samples investigated in this study were equivalent to those studied in [85, 252]. They were deposited on a super-polished Si wafer by magnetron sputtering with additional ion polishing of the deposited Si layers. The thicknesses of individual layers in the samples were ~3 nm for Mo and ~4 nm for Si. The samples were transferred through air prior to and post hydrogen exposures and no special pre-treatment step was applied before starting the exposures.

The samples were exposed in the set-up described in [85]. The hydrogen source was a capillary-type thermal cracker (Oxford Applied Research TC50). It was operated at a power of 55 W with a 1 SCCM H₂ flow. In addition to the neutral

Temperature dependence of hydrogen-induced blistering of multilayered films

atomic and molecular hydrogen flux, the source also produced an ion current on the order of ~ 75 nA.

Samples were exposed for 5 hours to the unmodified hydrogen flux from the thermal capillary cracker at various set-point temperatures ranging from 50 °C to 275 °C, under otherwise identical conditions. All samples were stabilized at the desired temperature prior to commencing the exposure. The sample temperature was monitored by a K-type thermocouple, which was spot-welded to the sample clamp, and was controlled via radiative heating by a back-mounted filament. Similar exposures were performed with the insertion of a biased deflection plate parallel to the incident particle direction. A bias of -1100 V was used to deflect charged species from the flux prior to interaction with the surface. This reduced the drain current measured on the sample during exposure to <1 nA.

Damage to exposed samples was typically evident to the naked eye as a discoloration/dulling of the original mirror-like surface. Regions covered by clamps during the exposure always appeared undamaged. Exposed samples were characterized by optical microscopy and atomic force microscopy (AFM). For samples exhibiting non-uniform damage, the analysis presented in this report was derived from the region exhibiting the most damaged (corresponding to the on-axis position of the capillary flux profile). In cases where there was no visible damage or where the damage appeared uniform, the analysis position was selected with reference to the non-uniform samples.

7.3 Results.

7.3.1. Exposures to H radicals and mixture of radicals and ions at different temperatures.

Figure 7.1 shows a comparison of optical microscopy images (magnification $\times 100$) obtained from the two sets of samples exposed at temperatures ranging from 50 °C to 250 °C. The left-hand-side (LHS) image segments are from samples exposed without the biased plate (ion+neutral flux), while the right-hand-side (RHS) segments are from samples exposed with the biased plate (neutral-only flux).

Exposures to the ion+neutral flux typically resulted in the formation of a distinctive concentric damage pattern on the surface, which is primarily due to the influence of ions [252]. Samples exposed at temperatures between 50 °C and 100 °C exhibited a well-defined central spot surrounded by regions of more diffuse discoloration. Exposures at 150 °C and 200 °C showed almost uniform discoloration, although a central spot was still distinguishable under close

inspection. The sample exposed at 250 °C appeared to have a uniform discoloration, while the sample exposed at 275 °C exhibited no obvious damage. The biased deflection plate was used to eliminate ions from the irradiating flux. In this case, no damage was evident after exposures at 50 °C and 75 °C, while samples exposed at between 100 °C and 250 °C all exhibited a uniform discoloration of the exposed surface. The sample exposed at 275 °C again appeared undamaged.

For samples exposed to the ion+neutral flux the size of blisters increases while their area number density decreases as the exposure temperature is increased from 50 °C up to 200 °C [Fig. 7.1(a)-(e), LHS]. Further increasing the temperature to 250 °C results in a reduction in blister size [Fig.7.1(f), LHS], although the number density of blisters has continued to decrease. The most obvious difference in the case of the exposures to the neutral-only flux [Fig. 7.1(a-f), RHS] is the absence of blisters for exposures done at 50 °C and 75 °C. Blisters develop only for exposures ≥ 100 °C. The removal of ions from the irradiating beam also results in the disappearance of the smaller of the two blister size distributions and of the ‘complex’ blister structures. Both of these features have already been attributed to the presence of ions in the irradiating flux [252]. The blistering can now be characterized as a single size distribution comprised of symmetric single-component blisters. As before, the individual blister size increases with exposure temperature up to 200 °C, while the area number density decreases.

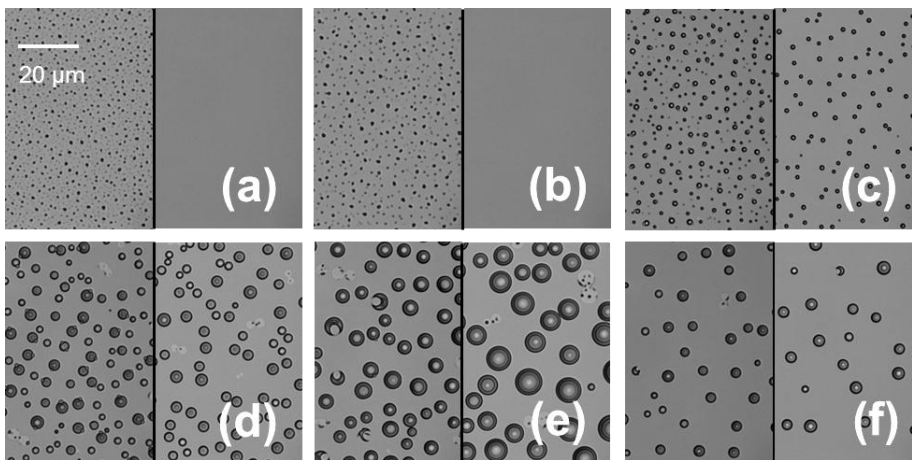


Figure 7.1: Optical microscopy images of the samples exposed for 5 hours using 1.0 SCCM gas flow at sample temperatures of: (a) 50 °C; (b) 75 °C; (c) 100 °C; (d) 150 °C; (e) 200 °C; and (f) 250 °C. The left-hand-side segment of each image represents an exposure to *unmodified flux* (neutrals and ions); the right-hand-side segment represents an exposure to *neutral flux only*.

Temperature dependence of hydrogen-induced blistering of multilayered films

At 200 °C, the blisters formed in the absence of ions are clearly larger than those formed when ions are present [Fig. 7.1(e)]. The typical blister size decreases again for the exposure at 250 °C, the result of which is roughly equivalent to that done without the biased plate.

Noteworthy aspects of these exposures are the distribution of blister sizes and the feature shapes. For exposures up to 150 °C two distinct blister sizes are evident on the optical images [Fig. 7.1(a)-(d), LHS]. The smaller of the two is attributed to direct ion-induced effects and the larger to blistering induced by thermal hydrogen [85, 238, 252]. ‘Double-’ and ‘multi-’ component structures (henceforth called ‘double’ blister structures as in the current case this kind of structures is dominant) arising from the apparent overlap of blisters are common on these samples. These typically consist of one or two smaller components attached to a single larger one. As is detailed in [252] these features are generally the result of ion-induced modification of the development of blisters induced by thermal hydrogen. With increasing exposure temperature, the size of the smaller components decreases relative to that of the larger component. At ≥ 200 °C only a single size distribution of single-component blisters appears to be present [Fig. 7.1(e)-(f), LHS].

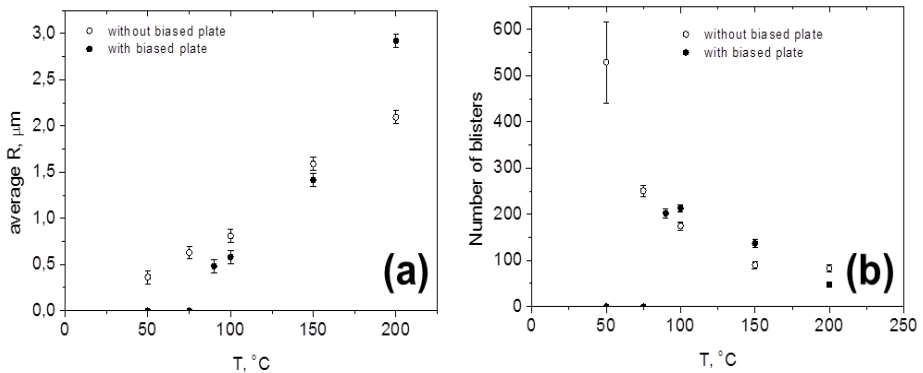


Figure 7.2: Comparison of (a) average blister size and (b) blister number for samples exposed to neutral H flux (filled circles) and to mixed flux of neutrals and ions. Data points are derived from optical microscopy images with 100x magnification.

Blister development on the two sample sets was analyzed on the basis of blister count and blister radius for the exposures between 50 °C and 200 °C. This analysis was done for ten unique optical images ($\sim 176 \times 132 \mu\text{m}^2$) from each sample and averaged values were derived. In the case of samples exposed to the ion+neutral flux, a size distribution analysis was used to designate blisters as either ‘ion-induced’ (smaller distribution) or ‘thermal neutral’ (larger distribution). All blisters formed by exposures to the neutral-only flux were deemed to be due to ‘thermal neutral’ process. Figure 7.2 shows a comparison

of the results for ‘thermal neutral’ blisters formed as a result of exposure with and without the biased plate.

Figure 7.2(a) shows the temperature dependence of the average blister radius. The presence on ions in the irradiating flux promotes the development of ‘thermal neutral’ blisters at the lower end of the temperature range studied, while they retard the growth of these blisters at higher temperatures. Figure 7.2(b) shows the ‘thermal neutral’ blister number density for the two sets of samples as a function of exposure temperature. In both cases the number of blisters decreases with increasing exposure temperature. For the exposures at 100 °C and 150 °C the number density of blisters is slightly larger in case of exposures done with the biased plate inserted. This may be a consequence of the selection threshold that must be applied when analyzing the samples exposed without the biased plate.

AFM measurements provide more detailed information regarding the blister dimensions. Figure 7.3 shows the result of a size analysis of AFM data obtained from the samples exposed to the ion+neutral flux. The individual blister radius is plotted versus the maximum Z-height. At temperatures ≤ 150 °C a clear distinction can be made between ‘ion-induced’ and ‘thermal neutral’ blisters. For temperatures ≥ 200 °C all blisters are designated as ‘thermal neutral’. The AFM scans confirm what is evident from the optical images: the blister density decreased with increasing exposure temperature across the full range, while the blister size increases with exposure temperatures up to 200 °C and decreased again for the exposure at 250 °C.

An analysis was also performed in order to track the shape change of ‘complex’ blisters, in particular ‘double-blister’ structures as a function of exposure temperature based on the relative dimensions of the two components. These features components were characterized in terms of their individual radii, which was done for 10 individual features on AFM data from samples exposed at between 50 and 150 °C. The averaged results are presented in figure 7.4. Figure 7.4(a) shows the absolute radii of the two components as a function of temperature, while figure 7.4(b) shows the corresponding ratio. Both components of these blisters grow in absolute terms with increasing exposure temperature, although, the ‘larger’ component grows faster than the ‘smaller’ one. Consequently, the ratio drops from ~ 0.8 at 50 °C to ~ 0.45 at 150 °C.

Temperature dependence of hydrogen-induced blistering of multilayered films

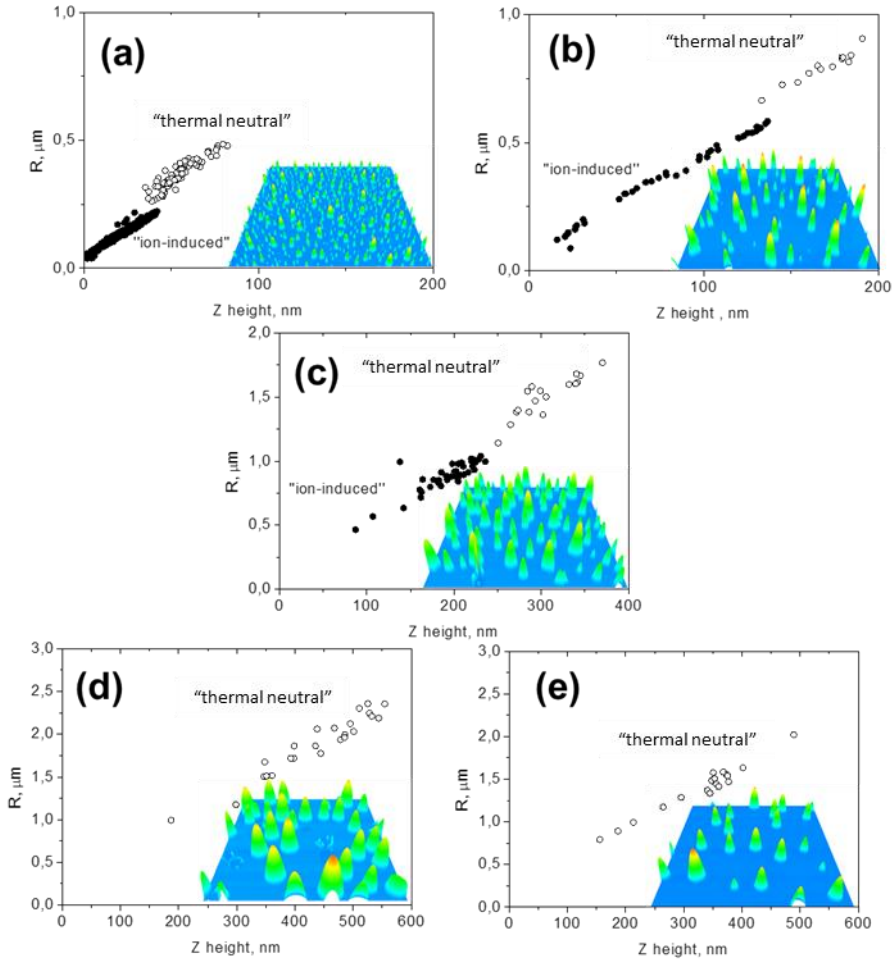


Figure 7.3: Plots of individual blister radius versus the corresponding Z height derived from the accompanying AFM scans of samples exposed without the biased plate at: (a) 50 °C; (b) 100 °C; (c) 150 °C; (d) 200 °C; and (e) 250 °C. Scans (a) and (b) are $25 \times 25 \mu\text{m}^2$; scans (c-e) are $40 \times 40 \mu\text{m}^2$. The Z-range of the AFM images matches the x-scale range of the associated plot.

It was previously shown by cross-sectional TEM images that intact ‘double-blister’ structures produced by H_2 exposures typically consist of a ‘large’ component that is formed due to delamination of the outermost bilayer overlapping with a ‘small’ component that is formed due to delamination of the outermost two bilayers. ‘Double-blister’ structures were not typically evident on samples exposed with the biased plate, although they were occasionally observed on the sample exposed at 200 °C. In these instances the structures were located in the vicinity of a burst footprint, suggesting that the rupture of the outermost bilayer may have contributed to their formation.

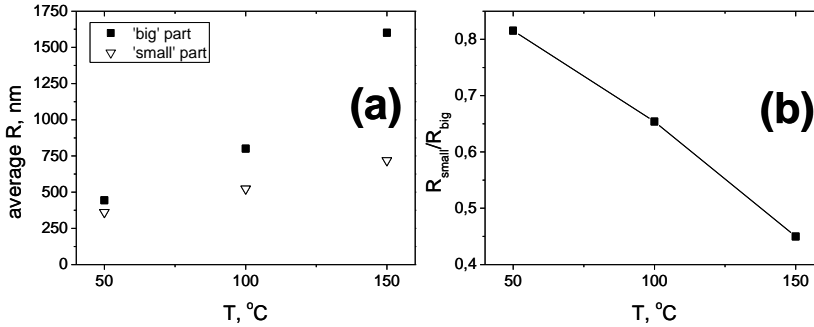


Figure 7.4: (a) Plot of “radius” of large and small components of “double blister” features as a function of exposure temperature. (b) Corresponding ratio of the two radii.

7.3.2. Effects of pre- and post-exposure annealing.

Pre- and post-annealing experiments were conducted in order to better understand the role of temperature as a modifier of the blister formation and growth. The purpose of pre-annealing was to determine the extent to which thermally-induced changes to the layered structure (e.g. layer compaction and intermixing) influence the formation and growth of hydrogen-induced blisters. Post-annealing was done to determine the extent to which temperature-driven redistribution of incorporated hydrogen contributes to blister growth.

For the pre-annealing study, the ML samples were held at temperatures of 250 °C, 300 °C, and 400 °C for 5 hours prior to exposure to the unmodified capillary cracker flux for 5 hours at 100 °C. After the exposure, the samples that had been pre-annealed at 250 °C and 300 °C exhibited blister damage, while that pre-annealed at 400 °C showed no visible damage. The absence of blistering in the latter case can be attributed to destruction of the ML structure due to intermixing. The post-annealing experiment was conducted by first exposing a sample for 5 hours at 100 °C followed by annealing at 250 °C for 5 hours.

Figure 7.5 shows a comparison of AFM images taken after an exposure without pre-/post-annealing (a), and from samples that were pre-annealed at 250 °C (b) and 300 °C (c) and post-annealed at 250 °C (d). The most obvious effect of pre-annealing is changes to the relative size of the “double-blister” components. At 250 °C (Fig. 7.5(b)) the size of the larger component has increased relative to those observed on the un-annealed sample, while that of the smaller component has decreased. The number density of blisters is approximately unchanged. For the 300 °C pre-annealing (Fig. 7.5(c)), the individual features are smaller compared to the un-annealed sample. In this case the smaller component is

Temperature dependence of hydrogen-induced blistering of multilayered films

almost absent. In addition, the number density of blisters has decreased. In the case of the post-annealed sample (Fig. 7.5(d)), the ‘hydrogenation’ blisters have increased in size relative to those on the un-annealed sample. This is primarily due to growth of the larger component of “double-blisters” structures. There was no significant change to the ion-induced blisters.

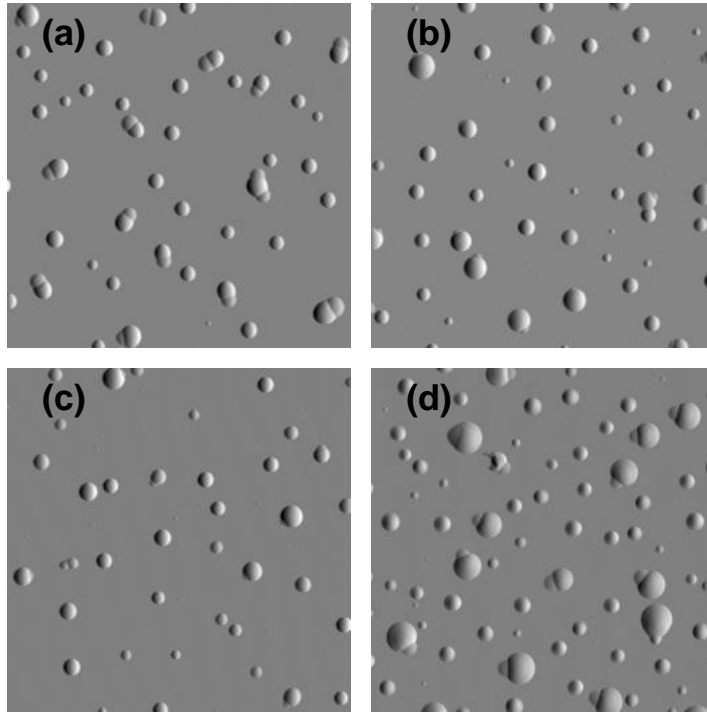


Figure 7.5: 2D representation of $20 \times 20 \mu\text{m}^2$ AFM scans of samples after 5 hours of exposure without biased plate at $100 \text{ }^\circ\text{C}$ with: (a) no pre-/post-annealing; (b) $250 \text{ }^\circ\text{C}$ pre-annealing, (c) $300 \text{ }^\circ\text{C}$ pre-annealing, (d) $250 \text{ }^\circ\text{C}$ post-annealing.

7.4 Discussion.

Three main topics are addressed in this section. The impact of ions on the observed temperature dependence; the relative importance of thermally-induced changes to the sample versus the temperature-dependence of blistering precursors; and an analysis of the blister growth as a function of temperature are discussed.

7.4.1. Influence of ions on blister formation

The simultaneous presence of two distinct blistering processes complicates the interpretation of temperature-induced changes. Performing exposures with the biased plate inserted suppressed the ‘ion-induced’ processes, allowing assessment of their influence on the temperature dependence. The comparison of the temperature dependence in the case of one versus two open pathways for blistering that is shown in figures 7.1-7.3 allows a number of conclusions to be drawn regarding the impact of ions on the underlying processes.

a) Ions promote hydrogenation blistering at low temperatures.

That ions facilitate blistering at lower temperature is evident from the absence of blisters on the samples exposed with biased plate at 50 °C and 75 °C. However, the blister distributions that are formed at these temperatures when ions are present are not consistent with solely an ion-induced processes being operative. These samples exhibit two characteristic blister size distributions, which are also present after the exposures done at 100 °C and 150 °C. In the latter cases, application of the biased plate results in the elimination of only the smaller of the two distributions. Consequently, the “larger” distribution is attributed to a blistering process induced by thermal hydrogen species. Thus, the emergence of two distributions at lower temperatures for exposures without the biased plate indicates that the ions are facilitating the ‘thermal neutral’ process. Note that it cannot be ruled out that a sufficiently long exposure to a neutral flux at lower temperatures would eventually result in blistering represented only by ‘large’ (hydrogen-filled) blisters. However, it is clear that the emergence of these blisters is greatly enhanced by the presence of ions.

An ion-assisted process of hydrogen trapping has been discussed by Airapetov *et al* [16]. Based on deuterium uptake measurements, the authors proposed that in case of D bombardment of carbon materials, ions promoted trapping of neutral deuterium. They suggested the creation of ‘active sites’ at the surface due to inelastic interaction of the impinging ions with the sample. Deuterium, trapped by this mechanism filled both pre-existing traps in the sample and ion-induced traps formed due to the energetic ion bombardment. Such a mechanism is consistent with the behaviour observed for the current ML samples and was confirmed in our previous manuscript, where ion-enhanced H uptake and, additionally, transport to deeper layers was observed [252].

b) Ions suppress blister growth at higher temperatures.

In seeming contradiction to the stimulating effect at low temperature, figures 7.1-7.3 also illustrate that the presence of ions appears to suppress hydrogenation blister growth at higher temperatures. With increasing sample

Temperature dependence of hydrogen-induced blistering of multilayered films

temperature the main effect of ions shifts from one of directly inducing the formation of blisters to one of retarding the growth of blistering via ‘thermal neutral’ processes. At 200 °C ion-induced blisters either do not develop or become indistinguishable from hydrogenation blisters. The blisters that do form at this temperature are significantly smaller when ions are present. This suggests that ions are still inducing formation of hydrogen-vacancy complexes that are precursors of ‘ion-induced’ blisters and thus some amount of hydrogen will be transferred to those sites, however it no longer leading to the emergence of additional macroscopic blisters, at least on the time-scales investigated in this study.

As is proposed in [85, 252], energetic ions are capable of creating new nucleation points for blistering precursors in the samples. Hence, they will increase the competition for available hydrogen species in a sample relative to an exposure done without ions. Distribution of available hydrogen over a larger number of sites should result in a smaller average blister size. This effect may be operative even if the new sites do not develop into macroscopic blisters.

c) Formation of ‘double-blisters’

As was demonstrated in [252] and again in figure 7.1, the development of ‘double-blisters’ structures requires the presence of ions in the irradiating beam. These features were generally absent from samples exposed with the biased plate. However, some such structures were occasionally evident on the sample exposed with the biased plate at 200 °C. They were generally observed in the vicinity of the ‘burst’ blisters. In this case it appears that the development of the ‘double-blisters’ is attributable to direct introduction of thermal hydrogen to deeper layers, which becomes possible after these layers are exposed as a result of blister rupture. This observation has several implications:

- The presence of ions is not an absolute prerequisite for the emergence of “double- blister” structures. They can develop provided a pathway to deeper bilayers is available to thermal hydrogen;
- In the absence of ions, transport of thermal hydrogen to deeper layers is ineffective while the ML structure remains intact;
- Ions promote the transport of hydrogen across the bilayer structure and formation of new trapping sites in deeper layers and it is this process rather than direct implantation of energetic hydrogen ions that drives the development of “double-blisters” in intact MLs.

As is discussed in the next subsection, the latter point is supported by the pre-annealing data shown in figure 7.5.

It can be seen in the LHS segments of figure 7.1 and in figure 7.4 that the individual components of ‘double-blisters’ develop differently as a function of the exposure temperature. Although both grow with increasing temperature, the growth of the ‘larger’ component is more rapid than that of the ‘smaller’ component. These components are typically associated with detachment of the outermost one and two bilayers, respectively. The current results support the contention that development of the ‘smaller’ component requires transport of hydrogen across the bilayer structure (see below). The “smaller” component grows more slowly because it is dependent on both the rate of thermal hydrogen trapping in the outermost bilayer and the rate of ion-induced transport to deeper layers, whereas growth of the larger component is primarily dependent only on the former. As noted in the next section, thermally-induced changes to the ML, which are typically dominated by growth of the molybdenum silicide interfacial layers, retard the growth of double-blister structures.

7.4.2. Thermally-induced effects.

Since the exposure conditions were identical, changes to blistering in the case of pre-annealed samples are solely the result of the thermally-induced modification of the ML structure. The main consequence of pre-annealing samples is changes to the “double-blister” features. The size of the smaller component of the double blisters decreases with increasing pre-annealing temperature [Fig 7.5(a)-(c)]. This is true both in absolute terms and relative to the size of the corresponding larger component. In contrast, the larger components on the sample pre-annealed at 250 °C have increased in size relative to those of the “standard” exposure. This is consistent with a reduction in efficiency of ion-induced transport to deeper layers. Consequently, more hydrogen remains in the outermost layer, contributing to the growth of the larger component. Reduced transport due to a thermally-induced increase in the interface layer thickness would allow for differential growth of blister components localized at different depths in the ML stack. It is known that growth of a compound interface between the layers occurs at elevated temperatures [70].

Gradual growth of the interfaces in Mo/Si ML during annealings up to ~ 300 °C has been reported by Nedelcu et al. [67]. For instance, annealing at 250 °C for 5 hours will cause interlayer thickness change growth of ~ 0.14 nm [168]. This change causes a significant of radius of ‘small’ part of a ‘double’ blister, a trend that continues for annealing at 300 °C.

While the larger component of the “double-blisters” increases in absolute size when the sample is pre-annealed at 250 °C, it decreased after the 300 °C pre-annealed. In the latter case, all blisters are smaller relative to the un-annealed sample. This indicates that thermally-induced stress relaxation and interface layer growth can contribute to a reduced susceptibility to the development of

Temperature dependence of hydrogen-induced blistering of multilayered films

macroscopic blisters. An additional factor is a possibility of phase transformation of the interface (from amorphous to crystalline) that occurs at $T \sim 300\text{-}325\text{ }^{\circ}\text{C}$ [67]. In this case, preferential trapping of hydrogen can occur deeper in the interface layer thus reducing amount of hydrogen that could have been consumed for growth of hydrogen bubbles in Mo layer [252].

No blister formation was observed on a sample that was pre-annealed to $400\text{ }^{\circ}\text{C}$. This temperature is sufficient to completely transform the individual Mo and Si layers to bulk MoSi_2 , eliminating the ML structure. The absence of distinct interfaces prevents the localized blister formation that is typical for these MLs. In the case of post-annealing, there is an increase of blister size relative to the reference sample (compare figure 7.5(a) and (d)). Thus, blister growth continues after the exposure has terminated. This additional growth is primarily associated with the thermal neutral blisters, and specifically with the larger component of these double-blisters structures. This suggests that the post-annealing stimulates re-emission of hydrogen gas from surrounding media to the blister cavities and thus increases the pressure inside the blister and its volume. The smaller components do not exhibit significant additional growth as in the absence of irradiating ions, transport from the outermost layers is absent.

The changes observed as a result of pre-/post-annealing are relatively minor in comparison to the influence of the sample temperature during the actual exposure (compare figures 7.1 and 7.6). Thus, the effect of temperature uptake and distribution of hydrogen during the exposure is far more critical in determining the size and number of blisters formed than thermally-induced structural and chemical modification to the ML. This is emphasized by the fact that blisters did not develop on the sample that was exposed at $275\text{ }^{\circ}\text{C}$ while they did appear on the sample that was pre-annealed at $300\text{ }^{\circ}\text{C}$ followed by exposure at $100\text{ }^{\circ}\text{C}$ (figure 7.5(c)). NRA and ERD analysis of samples exposed without the biased plate indicate that the sample exposed at $150\text{ }^{\circ}\text{C}$ had the highest H-content. The reduction in H-content at higher temperatures may be due to thermal re-emission of hydrogen. However, the growth of blisters is not simply related to the total H-content since the largest individual blisters are observed for the $200\text{ }^{\circ}\text{C}$ exposure. The decrease in blister size for the $250\text{ }^{\circ}\text{C}$ exposure and their absence for the $275\text{ }^{\circ}\text{C}$ exposure may also be due to enhancement of re-emission relative to blister nucleation and growth processes. As trapping of neutral hydrogen occurs initially in the outermost Si layer, relevant data on H diffusion/reemission in Si should be considered. For instance, in reference [253] it was reported, that H diffusion in silicon becomes significant at $\sim 250\text{ }^{\circ}\text{C}$, thus hydrogen out-diffusion from Si layers will be enhanced and would be reflected in a size decrease of observed blisters.

7.4.3. Processes of blister formation.

This section reviews the previous findings on the processes of blister formation in ML structure and points out how those processes are influenced by the temperature-induced effects (in the behavior of hydrogen as well as in the ML structure itself).

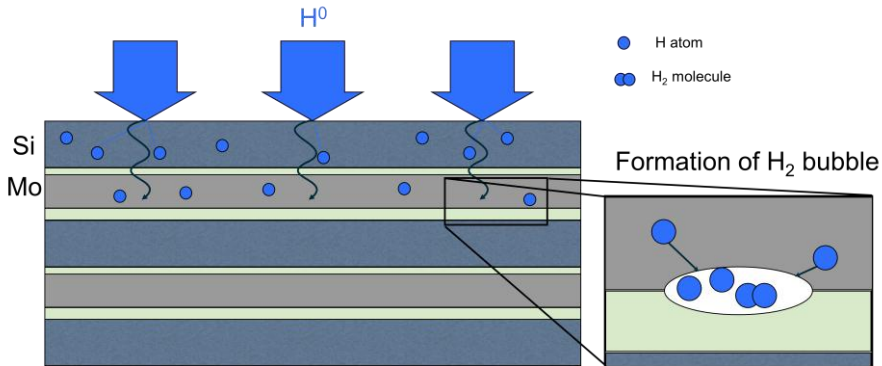


Figure 7.6: Schematic representation of ‘thermal neutral’ process of blister formation. Interface layers are shown in light green.

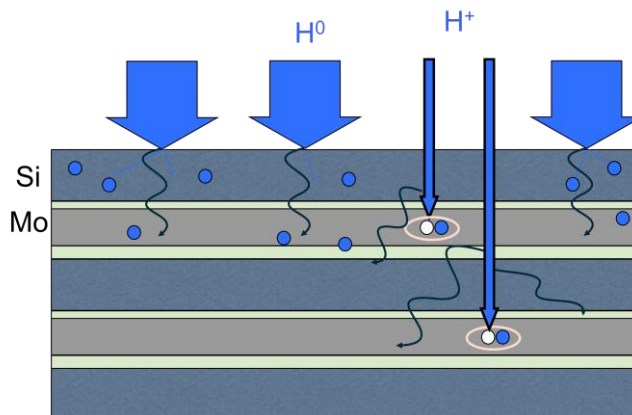


Figure 7.7: Schematic representation of ‘ion induced’ process of blister formation. Interface layers are shown in light green. Blue circles represent the same features as in figure 7.6. Formation of H-V complexes shown by ovals containing a vacancy (white circle) and an H atom (blue circle).

Let us start with the ‘thermal neutral’ process of blister formation. A simplified picture of the process is shown in Figure 7.6. The process consists of the following steps:

- Trapping of H atoms at the surface of the outermost Si layer

Temperature dependence of hydrogen-induced blistering of multilayered films

- Diffusion of H atoms through Si layer, some H atoms will be trapped at dangling bonds or stress centers in Si layer
- Diffusion of H atoms in Mo layer driven by deep sinks for H in Mo structure
- Segregation of H atoms to monovacancies in Mo and formation of H molecules
- Formation of blister precursors at stressed centers in the vicinity of Mo-on-Si interface
- Further growth of a hydrogen-filled bubble by accumulation of hydrogen molecules.

Figure 7.7 shows how this process is modified when neutral hydrogen flux is accompanied with flux of energetic H ions, thus an ‘ion-induced’ process of blister formation is operative. The ‘ion-induced’ process on itself can be described as follows:

- Ion exposure create ion-induced vacancies
- Those vacancies can form stable H-V complexes when interacting with diffusing H atoms
- Accumulation of H-V complexes at stressed centers at Mo-on-Si interface
- Further growth of a blister due to coalescence of H-V complexes

In addition to this process, the role of ions is in formation of the ‘double-blister’ structures facilitated by ion-induced process of H transport to deeper layers, including enhanced transport from Si to Mo layers due to ion-induced cleavage of Si-H bonds and creation of new trapping sites for H in Mo layer. However, creation of additional trapping sites also plays a reductive role in blister formation due to redistribution of hydrogen among more trapping sites and thus slowing down the growth of ‘thermal neutral’ blisters.

Let us now illustrate the effects of elevated temperature on blister formation in two regimes: $T \leq 200$ °C and $T \geq 200$ °C.

The first regime is illustrated in Figure 7.8. The effect is mainly in accelerated lateral diffusion of hydrogen that leads to formation of bigger blisters with smaller number density, as was previously stated in [86]. Let us focus on the simple picture including only formation of ‘thermal neutral’ blisters’. In this case, precursors of blisters can be described as hydrogen bubbles that start to form near the outermost Mo-on-Si interfacial layer. Increasing size of individual blisters and decreasing number density at elevated temperatures could reflect the initial preferential growth of ‘bigger’ bubbles that will happen due to consumption of hydrogen from ‘smaller’ bubbles in the surroundings. This can be an indication that the growth of blister precursors is governed by an Ostwald ripening-like process. Similarity could be found for instance with blister

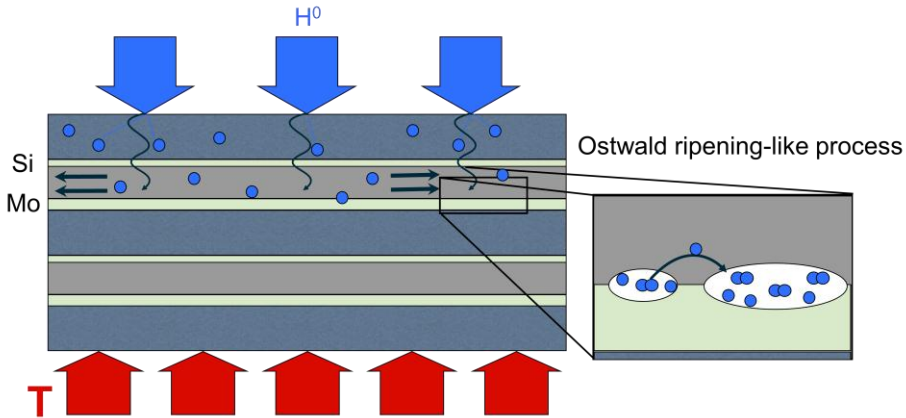


Figure 7.8: Schematic representation of the influence of exposure temperature on formation of ‘thermal neutral’ blisters in the first regime ($T \leq 200$ °C).

Formation during post-exposure annealing of H-irradiated Si samples that has previously been described in terms of an Ostwald ripening process [197]. Hydrogen exchange between platelets takes place leading to the growth of larger ones at the expense of the smaller. Longer annealing times resulted in bigger platelets with smaller number density. In the current case, the objects being observed are already macroscopic surface modifications rather than platelets. As demonstrated by figure 7.5(d), these features do not dissipate with annealing and the growth of larger blisters does not go at the expense of the smaller ones. However, the size and number density of blisters formed as a function of exposure temperature should reflect processes that were operative during the pre-blisters stages.

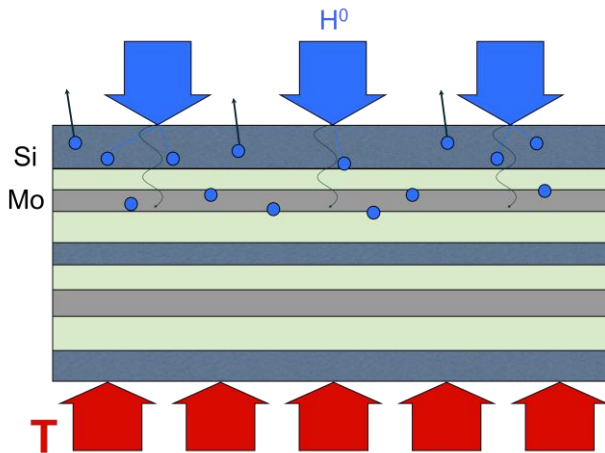


Figure 7.9: Schematic representation of the influence of exposure temperature on formation of ‘thermal neutral’ blisters in the second regime ($T \geq 200$ °C).

To simplify the picture, let us consider results of exposures only to neutral hydrogen flux. Thus, only blistering process induced by thermal hydrogen is effective and a single blister distribution is present on the surface. In this case, precursors of blisters can be described as hydrogen bubbles started to form in Mo layer. Increasing size of individual blisters and decreasing number density at elevated temperatures will reflect the initial preferential growth of 'bigger' bubbles that will happen due to consumption of hydrogen from 'smaller' bubbles in the surroundings. Further analysis is required to understand the details of ripening process in blister formation.

In the case of ion+neutral exposures, faster consumption of hydrogen for growth of blisters induced by 'thermal neutral' process at elevated temperatures is consistent with slower growth of small parts of 'double-blisters' structures meaning that less hydrogen travels transversely (in depth).

In the second regime (figure 7.9) blister formation is being suppressed due to the following processes:

- Hydrogen re-emission from ML structure at elevated temperature
- Broadening of and structural changes in the interface layers resulting in slower diffusion of hydrogen to deeper layers, including 1st Mo layer.

As a result, a decrease is observed both in number density and in the size of blisters.

7.5 Conclusions.

We have studied the temperature dependence of H-induced blister formation in multilayer (ML) samples consisting of nanoscale thickness Mo/Si films. The sample temperature during the irradiation was the dominant factor in the development of blisters. Effects related to thermally-induced changes of the ML structure were of lesser importance. For exposure temperatures up to 200 °C, the blister size increased and the total number density decreased. The trends observed are consistent with Ostwald ripening behaviour during the early stages of blistering, prior to the development of macroscopic blisters. At temperatures above 200 °C, an increasingly effective thermal re-emission of hydrogen resulted in a decrease of the blister size and their eventual absence at ~275 °C.

It was confirmed that the composition of the irradiating beam has an influence on the blistering process. In particular, the presence of energetic ions enhances blister formation at low temperatures (<100 °C). The results confirm presence of an ion-driven mechanism of neutral hydrogen trapping in the system. Furthermore, ions cause a transport of thermal hydrogen across the Mo-on-Si interface. Effects induced by energetic ions become less evident with increasing temperature. However, a continued influence of ions is identifiable in the stunted growth of blisters induced by neutral hydrogen.

8. Spectral and spatial structure of XUV radiation in a laser plasma-wall interaction.

Abstract.

Intense XUV radiation was observed during interaction of low temperature laser plasmas and wall materials. Laser plasmas with electron temperature $T_e \sim 40$ eV were created on massive solid targets (CF_2 and Al) by an excimer KrF laser (248 nm/ 0.5 J/ 13 ns/ 1 Hz). The wall was installed in the path of the laser-produced plasma expansion at distances between 0.5 and 3.5 mm. The spectral and spatial structure of XUV radiation (spectral range of $\lambda \sim 6\text{-}20$ nm) were studied using a grazing incidence spectrometer with a back-illuminated CCD camera as a detector. XUV spectra of F and Al ions were analyzed. At large plasma-wall distances three body recombination was identified as the dominate process responsible for ionic level population and radiation. The experiments demonstrate an effective way of creation of low temperature ($T_e \sim 1\text{-}10$ eV) plasmas interacting with the solid surfaces (walls).

8.1 Introduction.

One of the methods to generate a controlled process of plasma-surface interaction is to place a solid wall in the pathway of a laser produced plasma (LPP). The phenomenon of Laser Plasma-Wall Interaction (LPWI) was for the first time observed and described by Presnyakov and Shevelko [122] and was further investigated in [123-125]. It has been shown that LPWI process leads to emission of X-rays in the VUV and XUV ranges. The effect of LPP cooling by material interactions leading to an increase of 3-body recombination was used by Suckewer et al. for development of soft X-ray lasers [254, 255].

LPWI allows varying the parameters of plasma-surface interaction in a wide range by changing properties of the laser pulse, target-wall distance and by choosing appropriate target and wall materials.

LPWI experiments can contribute to understanding of plasma-surface interaction processes in tokamaks, namely in the extreme cases of transient events [126] which is a topic of intensive investigation [121, 256-258]. Another field of interest is study of particle damage to EUV collector mirrors for EUV photolithography by energetic highly-charged ions emitted from LPP sources [53, 54, 259-262]. LPWI studies could be used as complementary experiments to exposures at linear plasma generators with high particle fluxes [119, 120, 263, 264] and set-ups for studies of plasma-wall interactions relevant to collector optics development [265]. The advantages of LPWI experiments are that they cover a range of relevant conditions, do not require complex installations, they have a high repetition rate, and allow the use of well-established in-situ diagnostics (X-ray and XUV spectroscopy) to study the interaction of LPP with the solid surface.

Previous works were devoted to interaction of solid wall with highly charged ions produced in LPP. In the current contribution, LPP was produced with a medium power (0.5 J) excimer laser from Al and CF₂ targets resulting in lower ionization stages present in the plasma ($Z \sim 5$) and thus colliding with the wall (Ta). This interaction resulted in intense irradiation in XUV range (6-20 nm). Spectral and spatial structure of the irradiation has been recorded. In particular, the distribution of the various ionization stages was investigated to distinguish between excitation and recombination processes at different target-wall distances. The effects of cooling and shockwave formation on the plasma parameters were investigated. Three body recombination was identified as the dominate process responsible for ionic level population and X-ray irradiation. The plasma temperature range which is accessible in the experiment ($T_e \sim 1-10$ eV) is close to the expected temperature in the divertor region of ITER [266]. Thus we demonstrate an easy and effective way of creation of low temperature plasma interacting with solid surfaces.

8.2 Experimental.

The scheme of experiment is shown in Figure 8.1. Laser-produced plasmas were created by focusing of KrF excimer laser (0.248 nm/0.5 J/13 ns) radiation onto a massive solid target (CH_2 , CF_2 or Al). The laser beam was incident under 45 degrees relative to the target surface. A Ta wall was installed in the path of the laser-produced plasma expansion at variable distance R between 0.5 and 3.5 mm.

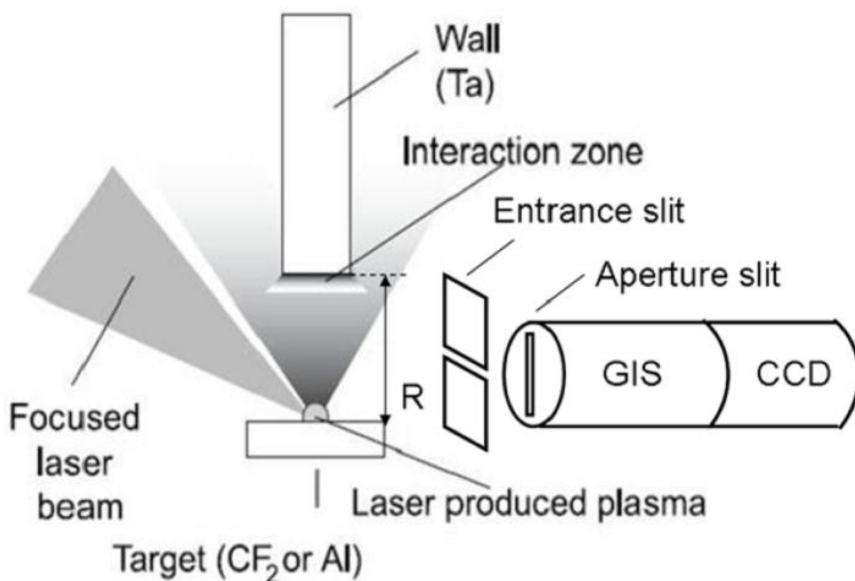


Figure 8.1: Scheme of laser plasma-wall interaction experiments. GIS – grazing incident spectrometer, CCD- back illuminated CCD camera.

The detailed representation of the experimental setup is shown in figure 8.2. XUV spectra were investigated using a 1-m grazing incidence spectrometer in off-Rowland geometry[267]. In the off-Rowland geometry, the curvature of the grating defines the ‘Rowland-circle’. By positioning the entrance slit of the spectrograph on the Rowland-circle, both the 0th order of diffraction as the higher diffraction orders give a sharp image of the entrance slit on the Rowland circle. By positioning the CCD camera perpendicular to the Rowland-circle only one wavelength will be focused, while at other wavelengths a slight broadening can be observed. By placing a slit in the spectrograph, perpendicular to the spectral dispersion direction, pinhole imaging is done perpendicular to the diffraction direction.

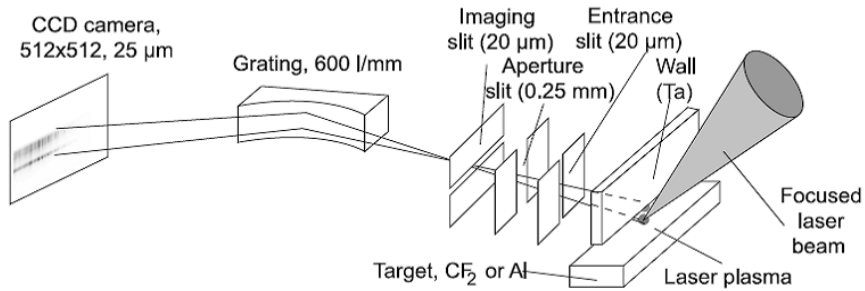


Figure 8.2: Detailed scheme of the grazing incidence spectrometer in off-Rowland geometry with additional imaging slit.

By careful alignment, the spectral and spatial directions are aligned such that the spectrum of the plasma is obtained as a function of the distance to the target. A 600 l/mm Au coated grating was used in the spectrometer. The wavelength range of registration was $\Delta\lambda = 6\text{-}20$ nm. The entrance slit ($20\ \mu\text{m}$ width) was positioned at 1.57 cm from the plasma. An additional aperture slit ($250\ \mu\text{m}$ width), positioned at 3.83 cm from entrance slit, was used to increase the spectral resolution in a larger spectral range. With this combination of slits, a width of $100\ \mu\text{m}$ is integrated in the plasma-wall region. Over the investigated spectral range the spectral resolving power varied from $\lambda/\delta\lambda = 90$ at the long wavelength range of the spectrum, limited off-Rowland positioning of the CCD camera, to $\lambda/\Delta\lambda = 100$ at the short end of the wavelength range, limited by the resolution of the CCD camera. The imaging slit was $20\ \mu\text{m}$, with a plasma-slit distance of 6.1 cm and a slit-CCD distance of 16.2 cm. We obtained a magnification of 2.7 in the focal plane. From measurements of the wall position of different images with known target-wall distance, a magnification was found of 2.66, which coincides with the above measurement.

The images were recorded on a back-illuminated CCD camera with 512×512 pixels of $25\ \mu\text{m}$ square. The sensitivity of the back-illuminated CCD camera is proportional to the energy of the incoming photons. The response of the CCD camera was compared to the response of a calibrated AXUV-100 diode [268] using narrow band imaging with multilayer mirrors at wavelengths of 4.4 and 13.5 nm. It was found that the response of the camera was 20 and 50% at given wavelengths. In the current manuscript the main focus is in qualitative studies of relative changes in the intensities at fixed wavelengths in dependence on the wall position. This kind of experiment does not rely on comparison of intensities in different wavelength ranges and thus does not require absolute or relative calibrations of the CCD spectral response and the grating efficiency.

Measured spectra showed good stability. The differences between series of measurements at fixed target-wall distances were about 10-20%. The noise level of the CCD was less than 10% of the smallest measured intensity (in the scale of figure 8.3 it is $\sim 0,001$ a.u.).

8.3 Results and Discussion.

The effective source size on a target in the XUV spectral range was measured using filtered zero order of reflection which represents a one-dimensional image of the source. The size was $r_0 \sim 300 \mu\text{m}$ at FWHM. Due to the plasma expansion, this XUV source is larger than the focal spot ($\sim 60 \mu\text{m}$).

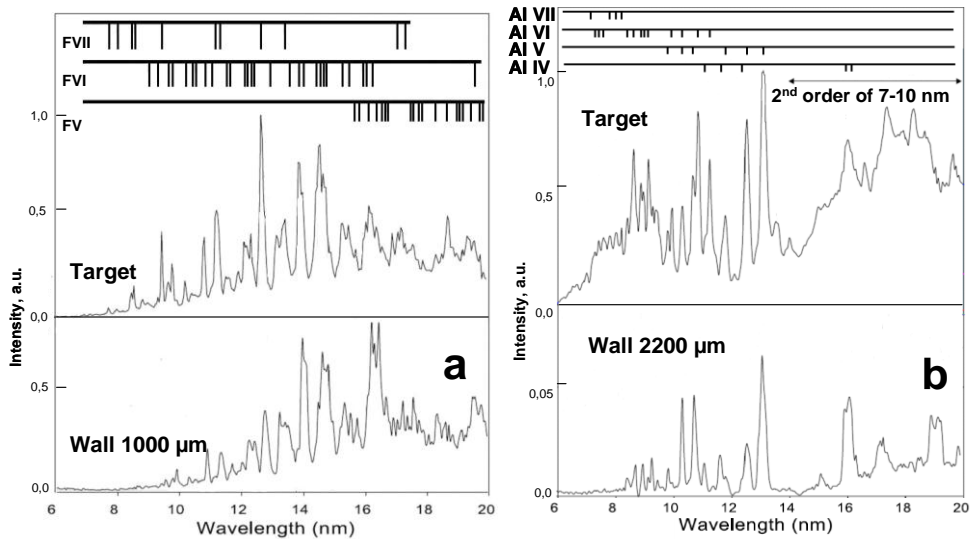


Figure 8.3: XUV irradiation spectra at selected target-wall distances.(a) F spectra. (b) Al spectra. Bars on top of every graph show positions of identified lines in the spectra.

Spectra of C V, C VI ions (CH_2 target) were used for electron temperature T_e measurements. The slope of recombination continuum gave a value of $T_e = 40 \pm 5$ eV. The T_e determined from the H-like C VI ($1s - 2p$) line to the He-like C V ($1s^2 - 1s3p$) line intensity ratio [267] calculated in a coronal equilibrium model was equal to $T_e \sim 60$ eV. The latter value is probably overestimated because the coronal model is not fully valid for dense low temperature plasmas of low Z ions.

Examples of different spectra as a function of target-wall distance for CF_2 and Al targets are shown in Figure 8.3. The analysis of data from Figure 8.3, showing the observed ions and identified transitions in laser-produced plasmas (on target surface) is presented in Table 8.1.

Table 8.1: Ions, ion data and transitions observed in laser-produced plasmas (on target surface).

Target	Averaged atomic weight (A)	Observed ions	Ionization potential I, eV	Ion charge (Z), and averaged charge (\bar{Z})	A/ \bar{Z}	Transitions
CF ₂	17	F VII	196	+6	3.4	2s-3p,3d
		F VI	168	+5 $\bar{Z}=+5$		2s ² -2s3p, 3d
		F V	120	+4		2s ² 2p- 2s ² 2p3s, 3d
Al	27	Al VII	252	+6	6	2s ² 2p ³ - 2s ² 2p ² 3s, 3d
		Al VI	207	+5		2s ² 2p ⁴ - 2s ² 2p ³ 3s, 3d
		Al V	161	+4 $\bar{Z}=+4.5$		2s ² 2p ⁵ - 2s ² 2p ⁴ 3s, 3d
		Al IV	116	+3		2s ² 2p ⁶ - 2s ² 2p ⁵ 3s, 3d

The dominant lines in the target region are lines of F VII (Ionization potential I =185 eV) and F VI (I = 157 eV). In the case of Al, lines of mainly Al VI (I = 190 eV) and Al V (I = 154 eV) are observed, as well as a few strong lines Al VII (I = 242 eV).

At short target-wall distances, the lines of the same ionization stages are visible, although the distribution shifts towards lower ionization stages. A comparison between emission from target region and wall region in case of short target-wall distance is shown for the case of F ions (see Fig.8.3a) The plasma near-wall region shows a similar spectrum, although emission lines of F VI and Al V are slightly stronger, indicating a lower temperature in the near-wall region. For larger target-wall distances the lines of F V (I = 114 eV) and Al IV (I = 120 eV) become more and more dominant. An example is shown in Fig.8.3b where emission spectra from target region and wall region in case of large target-wall distance are compared for the case of Al ions.

Figures 8.4 and 8.5 show the integrated intensity as a function of distance in two spectral bands for expanding F and Al plasmas respectively.

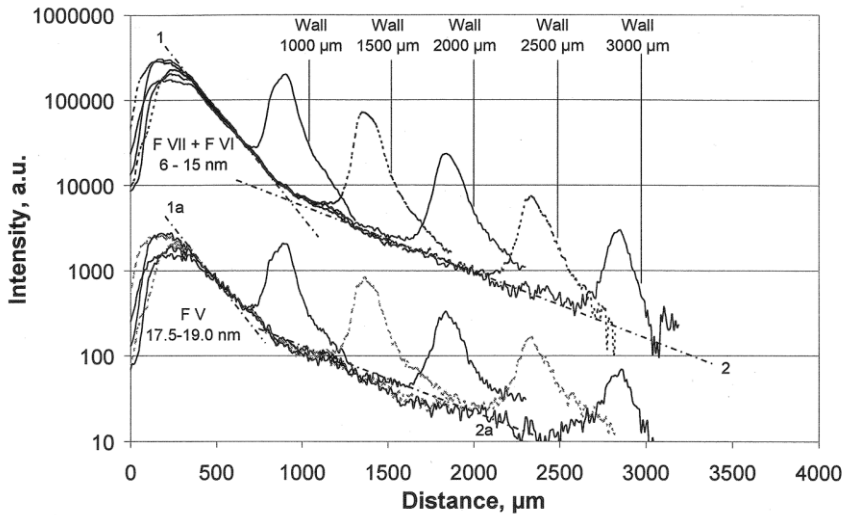


Figure 8.4: Distance dependence of the emission for the F plasma. Plotted are the integrated intensity of the 6-15 nm region, representative for F VII and F VI and the integrated intensity for 17.5-19.0 nm region, representative for F V. Dashed lines show separation of two emission regions : unperturbed plasma expansion (1 and 1a) and influence of plasma-wall interaction (2 and 2a).

Both unperturbed plasmas (F and Al) show an increase in emission of the FV-FVII and Al IV lines beyond $\sim 1000 \mu\text{m}$: line intensity curves show a bend at this point (see Fig. 8.4 and 8.5). The cause of the bend could be as follows. During the action of the laser pulse, heating of the plasma corona due to electron conductivity takes place. After the action of the laser pulse, the electron temperature T_e is decreased very rapidly during plasma expansion. This bend point at $\sim 1000 \mu\text{m}$ can be used for an estimation of the plasma expansion velocity, resulting in $v_0 = 1000 \mu\text{m} / \tau = 7.7 \cdot 10^6 \text{ cm/s}$ ($\tau = 13 \text{ ns}$ is a laser pulse duration).

The unperturbed plasma expansion velocity v_0 can be used for estimation of electron temperature T_e in laser-produced plasmas (hot core). The expansion velocity is equal to (see, for example, [269])

$$v_0 = a \cdot c_0 \quad (1)$$

where $c_0 = 10^6 [\text{cm/s}] \cdot (Z \cdot T_e (\text{eV}) / A)^{1/2}$ is the ion sound velocity (Z is ion charge, A is ion atomic weight) and a is a constant which can vary from 2 to 3. Using the data of Table 1 for an Al plasma ($Z \sim 6$, $A = 27$) we find $T_e \sim 30\text{-}67 \text{ eV}$.

This estimation is in a good agreement with T_e measurements using the slope of recombination continuum ($T_e = 40 \pm 5 \text{ eV}$).

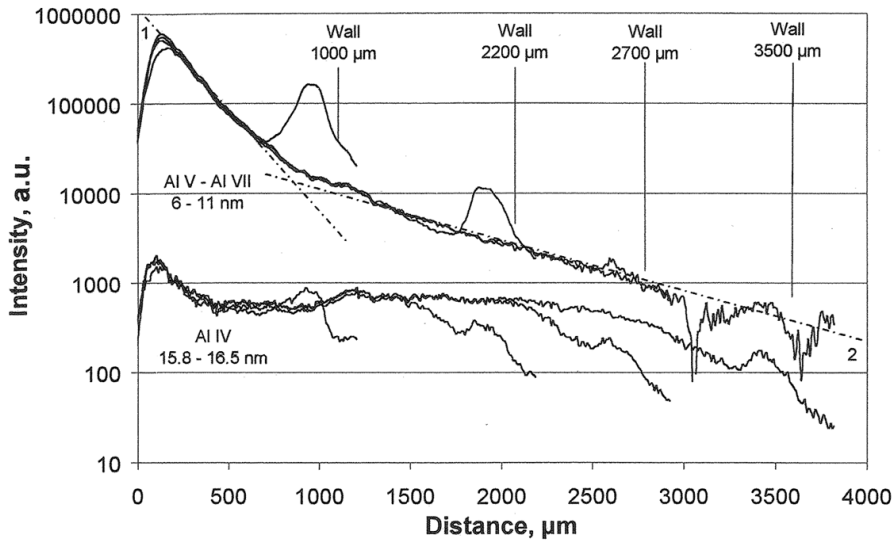


Figure 8.5: Distance dependence of the emission for the Al plasma. Plotted are the integrated intensity of the 6-11 nm region, representative for Al V – Al VII and the integrated intensity for 15.0-16.5 nm region, representative for Al IV. Dashed lines show separation of two emission regions : unperturbed plasma expansion (1) and influence of plasma-wall interaction (2) for Al V- Al VII emission.

There are three regions of XUV radiation (see Figs. 8.4 and 8.5): the hot core of the laser-produced plasmas (near the target surface), radiation in unperturbed expanded plasmas and radiation near the wall region. In the near wall region intense XUV radiation was observed. The same effect but in soft x-ray range was reported in [122, 125]. The intensity enhancement is substantial. The size of the interaction zone of expanded laser-produced plasmas with the wall is $\sim R$, the plasma – wall distance. The grazing incidence spectrometer is integrated in the plasma-wall range at a width of 100 μm , hence the total near wall intensity is in $(R_{\text{mm}}/0,1)$ times higher than intensities presented in Fig. 8.4&5. Another characteristic feature of the near wall emission is the presence of an additional dip in the intensity curve (especially clear for F V ions, see Fig. 8.4), which is observed before the maximum intensity at distances $R > 1.5\text{-}2$ mm.

The observed experimental results could be explained taking into account parameters and structure of the shock wave formed near the wall. When the laser-produced plasma bunch interacts with a wall, a shockwave is created near the wall. The shock wave front moves toward the incident plasma flux. The structure and the parameters of shock waves in plasma are considered in [270, 271]. In addition to the usual density jump in a shockwave – electron density N_e jump by a factor of 4 and electron temperature T_e jump by a factor of 2, there is a region of smooth temperature change. In front of the jump there is a region of

raised electron temperature due to the high electron thermal conductivity. The density jump and the increase in the electron temperature in the shockwave front, as well as the presence of a preheating "foot" ahead of the shock due to electron thermal conductivity, explain the overall intensity profile of the EUV emission near the wall. The density jump increases the rates of both the collision and the recombination processes, leading to intense XUV emission in line of highly charged ions. However, the processes, which are responsible for the observed emission, are different at various R distances: the observed "foot" of conductivity at $R > R_0 \sim 1.5\text{-}2$ mm indicates that processes responsible for radiation at this point are changed. At smaller distances $R < R_0$ near wall radiation is caused by excitation processes, at distances $R > R_0$ recombination processes prevail over excitation. This fact is also confirmed by the shape of the experimentally observed spectra: for small R the spectrum of near-surface plasma resembles the spectrum of the laser plasma (see Fig. 8.3a). In the case of large R the shape of the spectrum is significantly different from the initial one (see Fig. 8.3b), confirming that a change of the processes responsible for irradiation is taking place. We explain these in the following way. The various regimes observed in the experiment can be interpreted via the parameter of plasma bunch length, $v_0 \cdot \tau$, where v_0 is the unperturbed plasma burst expansion velocity, and τ is the laser pulse duration [125]. In our case as it was shown above $v_0 = 7.7 \cdot 10^6$ cm/s, $\tau = 13$ ns, and the parameter $v_0 \cdot \tau = R_0 = 1$ mm. At small plasma-wall distances $R \ll v_0 \cdot \tau$, the laser-heated plasma follows an expansion closed to isothermal one. When the plasma bunch interacts with the wall, an electron density jump in the shockwave takes place. The electron temperature observed in the shockwave front near the wall is approximately the same as in laser-produced plasmas. Both of these effects lead to excitation processes (rate is proportional to $\exp(-\Delta E/kT_e)$ [272], where ΔE is the excitation energy. At large plasma-wall distances $R \gg v_0 \cdot \tau$, the expanding laser plasma follows adiabatic expansion, and the electron temperature T_e falls rapidly ($T_e \propto R^{-1} - R^{-2}$) [273]. The increase of T_e in the shockwave is no longer enough to excite levels from the ground state of highly charged ions. In this case recombination processes take place (the recombination rate $\propto T_e^{-9/2}$ for three-body recombination and $T_e^{-1/2}$ for photo recombination). The recombination character of the radiation is confirmed by the presence of an additional dip in the intensity at $R > 1.5$ mm. The preheating "foot" ahead of the shockwave due to electron thermal conductivity leads to a decrease of the recombination rate and hence to a decrease of the line intensities.

To specify recombination process let us consider correspondent recombination rates [271, 272]. Photo recombination rate is equal to

$$b_{pr} = 2.7 \cdot 10^{-13} \cdot Z^2 \cdot T_e^{-1/2} \quad (2)$$

Three-body recombination rate is equal to

$$b_{br} = 8.25 \cdot 10^{-27} \cdot Z^3 \cdot N_e \cdot T_e^{-9/2} \quad (3)$$

It is clearly seen that for $T_e < 10$ eV ($R > 1$ mm, see below) three body recombination exceeds photo recombination at electron densities $N_e > 6 \cdot 10^{16} \text{ cm}^{-3}$ which is always fulfilled in our experiments. Due to three body recombination, highly excited states of multiply charged ions are populated. Subsequent cascade transitions due to collision and radiative processes lead to XUV line emissions of these ions.

Let us estimate what electron temperature could be in near wall plasmas at different plasma – wall distances R . Scaling and measurements of temperature of expanding laser-produced plasmas are presented in [273]: $T_e \propto R^{-1}$. Using these data and initial plasma source size ($r_0 \sim 300 \text{ } \mu\text{m}$) and electron temperature ($T_e = 40 \pm 5$ eV) we can find for unperturbed expanded plasmas (scaling in units R/r_0):

$$\begin{aligned} R=1 \text{ mm } T_e &\sim 12 \text{ eV,} \\ R=2 \text{ mm } T_e &\sim 6 \text{ eV,} \\ R=3 \text{ mm } T_e &\sim 3 \text{ eV.} \end{aligned}$$

Due to the jump in electron temperature in a shockwave these T_e values in the near wall plasmas will be two times higher. Note that for the distance of $R \sim 10$ mm the electron temperature could be as small as $T_e \sim 1$ eV. This temperature range of $T_e \sim 1-10$ eV corresponds to the one expected in the tokamak near wall plasmas [266]. We can conclude that there is a perspective way to model such plasmas using one created in the laser plasma – wall interaction.

However, it is necessary to mention that differences in other plasma parameters have to be considered. For instance, there are large differences in electron density ($\sim 10^{14} \text{ cm}^{-3}$ for tokamak and $\sim 10^{19} \text{ cm}^{-3}$ for LPP). As it was mentioned above, this fact will lead to prevalence of three-body recombination in the case of LPP which is usually not the case for tokamak plasma. However, in case of tokamak plasmas with high density, three-body recombination can be a prevalent recombination process [274]. Another issue is related to extremely high particle fluxes ($\sim 10^{25} \text{ ion/cm}^2\text{s}$) and power loads (10^{12} W/cm^2) in case of LPWI which exceed loads in the extreme cases of ELMs [275] and plasma-wall interaction experiments in high-flux linear devices [257]. These will lead to more severe damage (melting, cracking) of the wall materials than in the case of tokamak conditions. High density of ions in the vicinity of the wall can lead to pressure-driven phenomena observed in laboratory plasma-wall interaction experiments e.g. surface boiling and liquid metal migration (see for instance [276]). Similar effects observed under tokamak conditions have different origin [11] thus making difficult a direct comparison between tokamak and laboratory

set-ups. Additionally, large discrepancy in the timescale should be mentioned (ns range for LPWI and ms range for fast phenomena in tokamaks, e.g. ELMs) which can lead to differences in heat deposition on the surface of wall materials. On a more positive note, extreme conditions of LPWI allow performing of fast ‘ultimate’ tests of first wall materials in the current configuration and by changing the parameters of interaction, e.g. laser power, it might be possible to enter regimes with lower particle fluxes, electron densities and power densities.

8.4 Conclusions.

We have studied spectral and spatial structure of XUV irradiation in a laser plasma-wall interaction (LPWI) experiment with varied target-wall distance. Laser produced plasmas were created on massive solid CF_2 and Al targets by a KrF excimer laser. Electron temperature of the laser-produced plasma was ~ 40 eV, as estimated from the slope of recombination continuum.

Intense EUV radiation was observed in the near-wall region. This phenomenon was explained by shock wave formation near the wall: at small target-wall distances radiation is caused by excitation processes, while at large target-wall distances it is caused by recombination processes. In this case, three-body recombination was identified as the dominant process responsible for ionic level population and XUV irradiation. Estimations of the electron temperatures at various target-wall distances show that $T_e \sim 1\text{-}10$ eV (close to values expected in the divertor region of ITER) can be achieved thus making the experimental scheme described in the manuscript an effective tool for creation of extreme cases of controlled plasma-surface interaction experiments relevant for fusion research.

9. Valorization

In this chapter examples of practical, real-life implementation of results and know-how from this thesis are discussed. In addition, recommendations are given on how the results could further improve the performance of multilayer systems for a variety of applications.

9.1 Scientific environment.

In general, the work of the Nanolayered Surfaces and Interfaces (nSI) department of the FOM Institute DIFFER is known to have a strong valorization potential in terms of delivering new solutions for improving performance and lifetime of optics for applications in EUV lithography equipment. The nSI department has been involved in various industrial partnership programmes [277]. For example, the author of this thesis participated in the FOM Industrial Partnership programmes XMO (eXtreme Multilayer Optics, funded by FOM and Carl Zeiss SMT AG), CP3E (Controlling Photon and Plasma induced Processes at EUV optical surfaces, with funding by FOM, Carl Zeiss SMT AG and ASML), and the EXEPT (Extreme uv lithography Entry Point Technology development) component of the European programme CATRENE (cluster for Application and Technology Research in Europe on Nanoelectronics), funded in part by the AgentschapNL. All three programmes pursued, or are still explicitly pursuing, industrial applications to varying degrees.

These participations serve as good examples of the general relevance of the work of the nSI department for industry, including the specific work described in the current thesis. This relevance led, for instance, to the establishment of a permanent FOM EUV lab at ASML in Veldhoven, giving the nSI department direct access to high-power EUV sources and other state-of-the art experimental facilities as well as daily contact and direct collaboration with the company research staff. The relevance of valorization at the nSI department is further illustrated by the awarding of two FOM valorization prizes to nSI members, namely to Dr. Tim Tsarfati (Valorization Chapter Prize, 2009) and to Prof. Dr. Fred Bijkerk (FOM Valorization Prize, 2010). In addition, the recent transformation of the nSI department into an ‘Industrial Focus Group XUV Optics’ [278] at the University of Twente shows the enhanced interest of many industrial parties in innovative solutions based on control of properties of ML samples and thin films at the nano-level.

9.2 Suppression of blister growth in multilayered samples.

As has been discussed in this thesis, exposure to hydrogen fluxes can lead to the formation of blisters in ML structures under laboratory conditions. This fact will lead to a deterioration of their performance, as illustrated by Pelizzo et al. [87] in relation to ML optics intended for space research missions (drop of XUV reflectivity). In the case of ML implementation as EUV optical elements for lithography equipment, any performance loss by the optics should be minimized in order to extend their lifetime and hence that of the production apparatus. As such, the current research may be of particular relevance for future generations of EUV lithography equipment in which much higher photon fluxes are planned.

An increased flux of EUV photons will result in an increase of secondary plasma density and, as a consequence, to higher fluxes of hydrogen particles towards and into the collector surface. This can be explained as follows:

- It was shown by van der Velden [279] that the density of an EUV-induced plasma in front of the collector optics is proportional to the radiation energy per pulse per unit area.
- It has been shown that hydrogen diffusion can be enhanced by light emission (in the visible range) [280] and a similar effect might be expected in the EUV range, thus potentially enhancing H-induced processes in ML optics, especially in the collector region.

Thus, our results must be translated to strategies that prolong the lifetime of multilayer optics even further. Such mitigation strategies must meet industry-defined boundary conditions in terms of not unduly affecting the performance of the ML sample (e.g. in terms of XUV/EUV reflectivity).

As part of the research described in this thesis, various mitigation strategies, based on altering the processes of ML preparation, have been tested. It became possible to achieve significant suppression of blister growth, in some cases without any decrease of ML performance. The main conclusion from this work was that blistering behavior of Mo/Si stacks can be controlled by tuning the properties of interface layers and/or changing the stresses of individual layers in the stack. It was shown by [281] that interface stresses can be reduced by, for example, annealing of the samples thereby transforming a sharp interface to a diffuse one.

As annealing of the whole stack might lead to significant EUV losses, a strategy to modify only the few outermost periods of Mo/Si stack was proposed. For instance, the last few bilayers of an otherwise conventional Mo/Si stack (prepared by e-beam deposition with additional ion polishing of the Si layers)

Valorization

were deposited without the ion polishing step. This results in rough interfaces and lower compressive stress values in the Si layers. Figure 9.1 shows a comparison of the effects of exposures of a standard uncapped Mo/Si ML sample and an uncapped “advanced” sample prepared without an ion polishing step to a similar hydrogen flux.

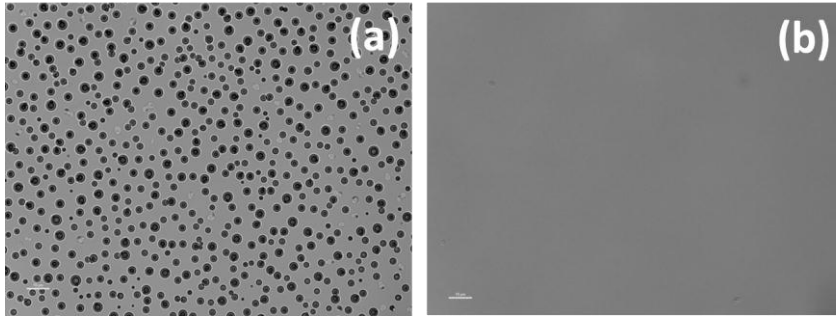


Figure 9.1: Optical microscopy images of ML samples exposed to H flux from a capillary cracker source (1.0 SCCM gas flow, $T_{\text{exp}}=100$ °C). (a) standard sample, 5 hours of exposure. (b) sample with improved composition, 48 hours of exposure.

It is clear that the standard sample is already severely affected by blistering after 5 hours of exposure while the sample with improved composition showed no signs of blister formation after 48 hours of exposure. EUV reflectivity measurements confirmed that in this case no drop in EUV reflectivity was found for this sample with respect to a standard sample in as-deposited state.

Other examples of mitigation strategies proposed by the author are in implementation of ion polishing step with higher energies (~ 1000 eV) or non-standard sputter gases, as these factors influence the interface properties of ML mirrors and might reduce the formation of blisters [128, 282]. Another example of a modified stack is usage of barrier layers (e.g. B4C) that has been proven to be effective in blistering mitigation under low-energy H bombardment. Changing the stress of the layers is also possible via changing the so-called gamma ratio (Mo/Mo+Si) of the topmost periods of the stack [161]. This was also demonstrated to have a positive effect as compared to a standard Mo/Si stack. However, those methods will lead to EUV losses in order from 1% to $\sim 10\%$ depending on the exact preparation method. Eventual choice of an appropriate mitigation strategy should be based on the particular environment conditions of the system where the ML sample is used, as well as the balance between the ML performance (e.g. XUV reflectivity) and the desired lifetime.

Decreased H concentration and absence of blistering in samples exposed at elevated temperatures (> 250 °C) provides support for a concept of a ‘hot’ EUV

collector optics assembly, such as proposed by Feigl et al. [283]. This concept, intended to eliminate any possibility of tin contamination build-up at the collector optics at an elevated temperature, employs heating-resistant ML mirrors based on implementation of barrier layers. Based on the results presented in this thesis, this concept might also prolong optics lifetime by suppression of hydrogen trapping in a ML stack. However, this approach might be less beneficial than the other mitigation strategies described above due to the possibility of thermally-induced damage to the substrate.

Successful development of mitigation strategies led to enhanced interest from industrial parties in the work described in this thesis. As a consequence, a patent application describing possible methods to suppress blister formation on ML samples has been filed via Carl Zeiss SMT AG [284]. In addition, the author has been involved in numerous discussions, working meetings and workshops at ASML aimed at developing solutions that further increase the lifetime of EUV optics, including access to an advanced high-power LPP EUV source. The author is currently continuing his work on the EUV optics lifetime and contamination issues as an employee of ASML. Further interest from the industrial partners in this research is evident from a new PhD project continuing investigation of hydrogen-induced effects in ML samples through the FOM-Zeiss-ASML co-funded CP3E Industrial Partnership Programme. As a part of this arrangement, the exposure set-up used by the author has been transported to Veldhoven in order to strengthen the experimental capabilities of FOM EUV lab at ASML.

9.3 Enhanced hydrogen retention properties in multilayered samples.

There has been a great deal of effort recently in the development and implementation of sustainable energy sources. Incidentally, the FOM Institute for Plasma Physics Rijnhuizen was recently transformed in to FOM DIFFER, the Dutch Institute for Fundamental Energy Research [285] involving new research directions in the field of solar fuels in addition to the pre-existing research on fusion energy [286, 287]. Relevant in this context is the development of solid-state systems for hydrogen storage. Several examples exist where ML systems were chosen as potential storage media [111, 112, 288]. In this thesis it was shown that a high concentration of hydrogen can be achieved in Mo/Si ML samples, especially in Mo layers [238]. The current choice of materials is not industrially applicable in terms of high density storage (due to the high mass of Mo). However, the results from studies on the Mo/Si system may provide useful information on ways to enhance the hydrogen storage properties of ML samples in general. Figure 9.2 shows a result of a resonant NRA measurement of H depth profiles in Mo/Si ML samples exposed to atomic hydrogen (filament H source, see Chapter 2). Of the two samples shown, one was prepared with an ion polishing step for the Si layers (used

typically to enhance interface quality for application of ML as EUV optical elements [128]) and the other one was deposited without ion polishing of Si layers. One can see a significant increase of the H concentration in the Mo layer in case of having applied a polishing step. This example shows that not only careful material selection, but controlling the deposition process and knowledge of interface engineering of ML samples, are important for the development of ML-based systems for hydrogen storage.

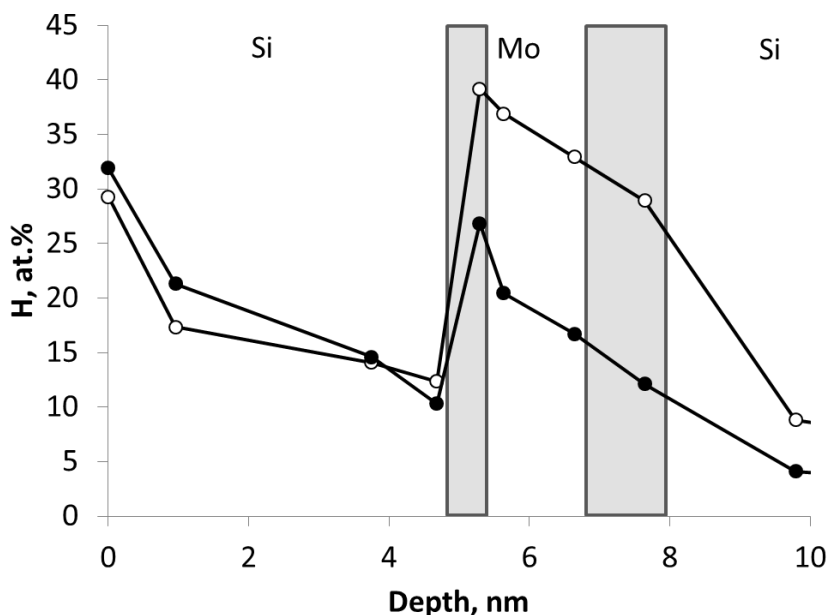


Figure 9.2: Hydrogen concentration in two Mo/Si ML samples after exposures to atomic hydrogen. Shown are a sample with ion polishing of Si layers (open circles) and a sample without ion polishing of Si layers (filled circles). Interface regions are shown in grey.

9.4 Laser plasma-wall interactions.

Apart from the already discussed in Chapter 8 application to fusion devices wall materials testing under extreme conditions, other areas can potentially benefit from laser plasma-wall interaction studies.

As was shown by Zielinski [289], interaction of plasmas produced by a pulsed plasma source intended to simulate extreme events in tokamaks with solid surfaces, can lead to deposition of nanoparticles and hardening of the surface. Such effects might be used for various industrial applications and similar effects might be possible to achieve using pulses of laser-produced plasma interaction with surfaces. The benefit of LPWI approach is, for instance, in a possibility of

metal plasma interaction with the surfaces, that will lead to a creation of a metal-doped surface layer with modified properties that might be useful to create protection of an initial metal surface in harsh environments or, alternatively, to create a reactive top layer with desired physical and chemical properties of the top layer.

A detailed proposal on how to use LPWI to simulate extreme plasma-wall interaction cases in tokamaks is currently in preparation and contacts have been established with representatives of ITER to initiate such experiments. When a dedicated set-up is in place, it will also allow thorough testing of surface treatment possibilities of the method.

9.5 Outlook.

The insight on mitigation strategies to hinder formation of blisters in ML structures, gained through the research described in this thesis, accelerated the efforts to further increase the lifetime of optics used in EUV lithography applications. Further activities need to include strategies to withstand harsh conditions in the vicinity of EUV sources having the much increased power that is necessary for high volume manufacturing of IC components. The development of those strategies should take into account possible trade-off between mitigation performance (absence of blisters/surface damage) and EUV-related performance (initial reflectivity and its change over time). Future research will need to address the resistance of novel capping layer materials to the impact of various hydrogen species in combination with effects of oxidation and interaction with contaminants (e.g. tin). A model of synergetic surface processes should be established.

Mitigation strategies must also be adopted to cases of ML exposure to high-intensity free-electron lasers, where blister-like damage has been observed [290] as well as optics intended for space research application [87] where exposures to hydrogen and helium ions with higher energies (keV range) are foreseen.

Studies relevant to hydrogen storage should focus on switching to materials that allow storage of a high weight percentage of hydrogen (e.g. Mg) and should be aimed at achieving higher retention of hydrogen as well as easy loading/unloading cycles and resistance to possible degradation during load/unload. In that respect, interface modification steps, like ion polishing, densification, interface treatment with chemically active ions should be explored in order to boost performance of ML-based systems for hydrogen storage. As a particular example, usage of cryogenically-grown multilayers should be explored as the system that has different interface layer properties.

Valorization

The process of valorization at DIFFER and at XUV focus group will further benefit from the tight collaboration of PhD students and researches with industrial partners. Apart from study of hydrogen-induced effects, topics of deposition of and processes in ML mirrors intended for next-generation EUV lithography ('Beyond EUV') [291], temperature-induced processes in complex ML samples [78] as well as surface photochemistry induced by EUV radiation [292] are to be explored. In such environment students are directly involved in solving complex and fascinating scientific problems at the cutting-edge of modern industry. As a practical example, the relocation of the HTC chamber (used by the author for the most of experiments) to FOM EUV lab at Veldhoven will allow its usage for research aimed at increasing EUV optics lifetime, with emphasis on non-linear processes near sputter thresholds [77] and synergetic effects of ionic and neutral bombarding species, e.g. ion-enhanced processes of hydrogen trapping [16]. This will further increase interaction of scientists and students from FOM with their colleagues at ASML. Additional benefits for students, in terms of direct contact with possible future employers, and for ASML (and their partners), in terms of preparation of dedicated specialists with focused knowledge ideally fitting their requirements and wishes, will naturally flow from this collaboration.

10. Summary

Being of a versatile and diverse nature, the field of particle-material interaction physics has traditionally been driven by applications. Two important current drivers are materials research for thermonuclear reactors and photolithography at Extreme UV wavelength. These topics have in common that they both represent extreme conditions: high photon, particle and plasma fluxes lead to non-linear processes and complex interaction phenomena. Both focus on unravelling the material damage mechanisms involving the lightest atom, hydrogen, as the active particle. The use of a nano-scale layered material, mimicking the lithography application, afforded an opportunity to perform depth and material sensitive studies. The challenge to identify the respective processes has been undertaken in the current thesis.

Initial experiments showed that interaction of hydrogen species with Mo/Si multilayered structures could lead to effects of top layer etching and blister formation. The latter phenomenon was related to hydrogen accumulation in the samples and had a complex dependence on irradiation conditions, namely on the hydrogen flux/fluence, the exposure temperature, and the type and mix of irradiating species.

Blistering was shown to have two pathways of different origin. The first was related to the interaction of the multilayer structure with atomic hydrogen species, leading to hydrogen accumulation and blister growth on pre-existing nucleation sites in the structure. The second pathway was ion-induced growth of hydrogen-vacancy complexes. These two processes were denoted as ‘thermal neutral’ and ‘ion-induced’ mechanisms of blistering, respectively. The presence of both processes could be seen as two types of agglomeration of blisters. Blistering was a result of delamination of one or two of the outermost bilayers in the Mo/Si structure. Consequently, this also led to the formation of complex, ‘double-blister’ structures arising from the overlap of delaminations localized at different depth locations.

The time-dependent development of blistering and its relation to the uptake of hydrogen was investigated. An increase of exposure time first led to a rise of the hydrogen concentration, followed by a saturation. The number density of both types of blisters was established before the hydrogen concentration reached the saturation level, whereas the size of blisters was more closely correlated with the H-content. In the case of ‘ion-induced’ blisters there was a direct correlation with the hydrogen uptake, whereas the size of hydrogenation blisters was also influenced by redistribution of hydrogen in the structure. Measurements of the depth profiles in the exposed samples revealed preferential hydrogen accumulation resulting in distinct maxima in the Mo layers, with a concentration up to 19 at.%.

Apart from creating ‘ion-induced’ blisters, ions were also found to modify the growth of ‘thermal neutral’ blisters. They could either assist their growth by initiating ion-stimulated uptake of hydrogen or, conversely, inhibit growth by providing competing trapping sites. The overall picture of blistering had a complex dependence on ion-to-neutral ratio in the irradiating beam. Formation of ‘double-blisters’ was observed only in the case when energetic ions were present in the beam, initiating an ion-induced transport pathway for hydrogen.

The effects of exposure temperature, as well as the influence of pre- and post-exposure annealing of samples, on the formation of blisters were also explored. Up to a certain limit (~200-250 °C) the main role of temperature was in accelerating hydrogen-induced processes in the system rather than influencing blistering by changing the multilayer structure. Below this limit, exposures at increasing temperatures led to bigger blisters with smaller number density. This behaviour was related to enhancement of lateral (within the layer) distribution of blistering precursors and could fit in a wider picture of thermally-dependent growth processes. Ions were demonstrated to be necessary to initiate both mechanisms of blister formation at lower temperatures (≤ 75 °C) confirming the presence of an ion-stimulated process of hydrogen uptake. Thus, an outline picture of blister formation in ML structures was developed, including a description of synergetic effects of exposure parameters on the formation of blisters.

This thesis also presents a study on laser plasma-wall interaction (LPWI) to mimic particle-material interaction. Processes of the interaction of low-charged ($z=5$) ions from laser-produced plasmas with a solid wall were discussed. Such interaction led to emission of X-ray radiation in the XUV region. Processes governing XUV emission were dependent on the target-wall distance. Measurements of the electron temperature showed that a similar temperature as in the boundary regions of tokamaks (1-10 eV) could be achieved. This confirmed the suitability of this approach for simulation of plasma-wall interactions in thermonuclear devices.

11. Samenvatting

Het onderzoek naar de interactie tussen deeltjes en materialen is veelzijdig en divers, waarbij toepassingen van oudsher een belangrijke motivatie vormen. Twee momenteel belangrijke thema's zijn materiaalonderzoek voor thermonucleaire reactoren en fotolithografie bij golflengtes in het extreem ultraviolet (EUV). Een overeenkomst tussen deze onderwerpen is dat beide gekenmerkt worden door extreme condities: hoge foton-, deeltjes- en plasmafluxen leiden tot niet-lineaire processen en complexe interactiefenomenen. Daarnaast ligt bij beide toepassingen de nadruk op het begrijpen van de mechanismes voor beschadiging van materialen door het lichtste atoom, waterstof, als actief deeltje. Het gebruik van een op nanoschaal gelaagd materiaal, zoals gebruikt wordt voor EUV lithografie, geeft de mogelijkheid om diepte- en materiaalafhankelijk onderzoek te verrichten. Dit proefschrift beschrijft het uitdagende onderwerp van de identificatie van deze processen.

Initiële experimenten toonden aan dat de interactie van waterstofatomen met Mo/Si multilaagfilms kan leiden tot het etsen van de toplaag en de vorming van blisters. Dit laatste fenomeen kan worden toegeschreven aan waterstofophoping in de lagen en heeft een complexe afhankelijkheid van de blootstellingscondities, zoals de waterstofflux en dosis, de temperatuur bij blootstelling en het type en verhouding van de deeltjes in de waterstofflux.

Twee mechanismes voor blistervorming zijn geïdentificeerd. Het eerste mechanisme is gerelateerd aan de interactie van de multilaag met atomair waterstof, resulterend in waterstofaccumulatie en groei van blisters vanuit reeds bestaande groeikernen in de multilaag. Het tweede mechanisme is het iongeïnduceerde groei van waterstof-leegstand complexen. Deze twee processen worden aangeduid als respectievelijk “thermisch neutraal” en “ionengeïnduceerde” blistervorming. Het optreden van beide processen kan worden waargenomen in de vorming van twee types blisters. Blistervorming treedt op door delaminatie van de bovenste of twee bovenste bilagen in de Mo/Si-structuur. Als gevolg hiervan ontstaan er ook complexe “dubbele” blisterstructuren, wanneer delaminaties op verschillende diepten elkaar lateraal overlappen.

De tijdsafhankelijkheid van blistervorming, alsmede de samenhang met de waterstofopname, werden onderzocht. Toenemende blootstellingstijd leidt in eerste instantie tot een toename van de waterstofconcentratie, gevolgd door verzadiging. Het uiteindelijke aantal van beide typen blisters per oppervlakte-eenheid wordt bereikt voordat de waterstofconcentratie verzadigt, terwijl de grootte van de blisters meer gecorreleerd is met de waterstofconcentratie. Bij

ionengeïnduceerde blisters is er een directe relatie met de hoeveelheid opgenomen waterstof, terwijl de grootte van de thermisch neutraal blisters mede bepaald wordt door de herverdeling van waterstof in de structuur. Metingen van het diepteprofiel van de blootgestelde monsters laten preferentiële opname van waterstof in de molybdeenlagen zien, met pieken van de waterstofconcentratie tot 19 at.%.

Naast de eerder vermelde vorming van ionengeïnduceerde blisters, werd vastgesteld dat ionen tevens de groei van thermisch neutraal blisters beïnvloeden. Ionen kunnen zowel de groei van blisters bevorderen door middel van ionengestimuleerde opname van waterstof, als de groei van hydrogenatie blisters stopzetten door vorming van concurrerende groeikernen voor waterstofopname. Het totaalproces van blistervorming heeft een complexe afhankelijkheid van de verhouding tussen ionen en neutralen in de inkomende bundel. Vorming van dubbele blisters is alleen waargenomen wanneer de inkomende bundel energetische ionen bevat, aangezien deze een ionengeïnduceerd transportmechanisme voor waterstof mogelijk maken. Tevens werd het effect van de blootstellingstemperatuur, alsmede de invloed van temperatuurbehandeling voorafgaand en na afloop van de waterstofblootstelling onderzocht. Tot een zekere limiet ($\sim 200\text{-}250\text{ }^{\circ}\text{C}$) versnelt een hogere temperatuur de waterstofgeïnduceerde processen, in plaats van beïnvloeding van de blistervorming door verandering van de structuur van de multilaag. Beneden deze limiet leidt waterstofblootstelling bij een hogere temperatuur tot een kleiner aantal blisters per oppervlakte-eenheid, waarbij de grootte van de blisters toeneemt. Dit gedrag hangt samen met een toename van de laterale verdeling van blisternuclei en past binnen een breder kader van temperatuurafhankelijke groeiprocessen. Bij temperaturen tot $75\text{ }^{\circ}\text{C}$ zijn ionen noodzakelijk voor het initiëren van beide mechanismes voor blistervorming, wat aantoont dat de waterstofopname gestimuleerd wordt door ionen. Op deze wijze heeft dit onderzoek naar het samenspel van blootstellingsparameters op de vorming van blisters geresulteerd in een voorlopig model voor blistervorming in multilaagstructuren.

Tot slot beschrijft dit proefschrift een onderzoek naar laserplasma-wandinteractie (LPWI) als model voor de interactie tussen deeltjes en materialen. Interactieprocessen tussen door een laserplasma geproduceerde ionen met lage lading ($z=5$) en een vaste wand worden beschreven. Deze interactie leidt tot emissie van röntgenstraling in het XUV golflengtegebied. De voor XUV-emissie bepalende processen blijken afhankelijk van de afstand tussen target en wand. Metingen van de elektrontemperatuur tonen aan dat een vergelijkbare temperatuur als in de grensregio van tokamaks (1–10 eV) bereikt kan worden. Dit bevestigt dat deze benadering geschikt is om de plasma-wandinteracties in thermonucleaire reactoren te simuleren.

12. List of publications

This thesis is based on the following publications:

Chapter 3: Kuznetsov AS, van de Kruijs RWE, Gleeson MA, Schmid K, et al. ‘Hydrogen interaction with EUVL-relevant optical materials’ *J. Surf. Investig.-X-ray Synchro.* 2010;**4**:563-6

Kuznetsov AS, Gleeson MA, van de Kruijs RWE, Bijkerk F ‘Blistering behaviour in Mo/Si multilayers’ *Proc. SPIE* 2011;**8077**:807713

Chapter 4: Kuznetsov AS, Gleeson MA, Bijkerk F ‘Hydrogen-induced blistering mechanisms in thin film coatings’ *J. Phys.: Condens Matter* 2012;**24**:052203

Chapter 5: Kuznetsov AS, Gleeson MA, Bijkerk F ‘Hydrogen-induced blistering in Mo/Si multilayers: uptake and distribution’, accepted by *Thin Solid Films*

Chapter 6: Kuznetsov AS, Gleeson MA, Bijkerk F ‘Ion effects in hydrogen-induced blistering of Mo/Si multilayers’ *J. Appl. Phys.* 2012;**114**:113507

Chapter 7: Kuznetsov AS, Gleeson MA, Bijkerk F ‘Temperature dependence of hydrogen-induced blistering of multilayered films’, submitted

Chapter 8: Kuznetsov AS, Stuik R, Bijkerk F, Shevelko AP ‘Spectral and spatial structure of extreme ultraviolet radiation in laser plasma–wall interactions’ *Plasma Phys. Control. Fusion* 2012;**54**:085019

Patent application: Kuznetsov AS, Gleeson MA, van de Kruijs R, Bijkerk F, ‘Method for producing a reflective optical element for EUV lithography’; patent WO 2012/175494 A1. Priority date 22 June 2011

Other publications

Begrambekov LB, Kuznetsov AS and Shigin PA ‘Hydrogen trapping in depositing carbon films’ *J. Nucl. Mater.* 2009; **390-391**: 685-8

13. Bibliography

1. Abramov VA, Igitkhanov YL, Pistunovich VI, Pozharov VA *J. Nucl. Mater.* 1989;**162-164**:462-6.
2. Allain JP, Brooks JN, Alman DA, Gonzalez LE *J. Nucl. Mater.* 2005;**337-339**:94-8.
3. Arnas C, Dominique C, Roubin P, Martin C, et al. *J. Nucl. Mater.* 2006;**353**:80-8.
4. Cambe A, Gauthier E, Hogan J, Layet JM *J. Nucl. Mater.* 2003;**313-316**:364-9.
5. Guo H, Zhu S, Li J *Plasma Sci. Technol.* 2006;**8**:633-8.
6. McLean AG, Stangeby PC, Bray BD, Brezinsek S, et al. *J. Nucl. Mater.* 2011;**415**:S141-S4.
7. Bauer W, Wilson KL, Bisson CL, Haggmark LG, et al. *Nucl. Fusion* 1979;**19**:93-103.
8. Liao C, Kazimi MS *Fusion Technol.* 1992;**21**:1845-51.
9. Ogawa T, Hasegawa A, Kurishita H, Nogami S *J. Nucl. Sci. Technol.* 2009;**46**:717-23.
10. Shu WM, Isobe K, Yamanishi T *Fusion Eng. Des.* 2008;**83**:1044-8.
11. Coenen JW, Bazylev B, Brezinsek S, Philipps V, et al. *J. Nucl. Mater.* 2011;**415**:S78-S82.
12. Linke JM, Hirai T, Rodig M, Singheiser LA *Fusion Sci. Technol.* 2004;**46**:142-51.
13. Sharma SK, Zushi H, Yoshida N, Watanabe H, et al. *Fusion Eng. Des.* 2012;**87**:77-86.
14. Shi Y, Miloshevsky G, Hassanein A *J. Nucl. Mater.* 2011;**412**:123-8.
15. Tokar MZ, Coenen JW, Philipps V, Ueda Y *Nucl. Fusion* 2012;**52**:013013.
16. Airapetov A, Begrambekov L, Brosset C, Gunn JP, et al. *J. Nucl. Mater.* 2009;**390-391**:589-92.
17. Alimov VK, Shu WM, Roth J, Komarov DA, et al. *Adv. Mater. Res.* 2009;**59**:42-5.
18. Porro S, Temmerman GD, Lisgo S, Rudakov DL, et al. *J. Nucl. Mater.* 2011;**415**:S161-S4.
19. Roth J, Schmid K *Phys. Scripta* 2011;**2011**:014031.
20. T'Hoën MHJ, Tyburska-Puschel B, Ertl K, Mayer M, et al. *Nucl. Fusion* 2012;**52**:023008.
21. Begrambekov LB, Kuznetsov AS, Shigin PA *J. Nucl. Mater.* 2009;**390-391**:685-8.
22. Jacob W *J. Nucl. Mater.* 2005;**337-339**:839-46.
23. Rubel M, Coad JP, Bekris N, Erents SK, et al. *J. Nucl. Mater.* 2003;**313-316**:321-6.

24. Roth J, Tsitrone E, Loarer T, Philipps V, et al. *Plasma Phys. Control. Fusion* 2008;**50**:103001.
25. Jeon KJ, Moon HR, Ruminski AM, Jiang B, et al. *Nature Mater.* 2011;**10**:286-90.
26. Reunchan P, Jhi SH *Appl. Phys. Lett.* 2011;**98**:093103.
27. Shangguan W *Sci. Technol. Adv. Mater.* 2007;**8**:76-81.
28. Vivero-Escoto JL, Chiang YD, Wu KCW, Yamauchi Y *Sci. Technol. Adv. Mater.* 2012;**13**:013003.
29. Yang Z, Ni J *Appl. Phys. Lett.* 2012;**100**:183109.
30. Yoo E, Habe T, Nakamura J *Sci. Technol. Adv. Mater.* 2005;**6**:615-9.
31. Yu XB, Wu Z, Chen QR, Li ZL, et al. *Appl. Phys. Lett.* 2007;**90**:034106
32. Okba F, Cherkashin N, Di Z, Nastasi M, et al. *Appl. Phys. Lett.* 2010;**97**:031917.
33. Shao L, Lin Y, Lee JK, Jia QX, et al. *Appl. Phys. Lett.* 2005;**87**:091902.
34. Baldi A, Borsa DM, Schreuders H, Rector JH, et al. *Int. J. Hydrogen Energ.* 2008;**33**:3188-92.
35. Kooij ES, Rector JH, Nagengast DG, Kerssemakers JWJ, et al. *Thin Solid Films* 2002;**402**:131-42.
36. Lohstroh W, Westerwaal RJ, Noheda B, Enache S, et al. *Phys. Rev. Lett.* 2004;**93**:197404.
37. Illiberi A, Kudlacek P, Smets AHM, Creatore M, et al. *Appl. Phys. Lett.* 2011;**98**:242115.
38. Lüdemann R *Mat. Sci. Eng. B Solid* 1999;**58**:86-90.
39. Natsuhara H, Ohashi T, Ogawa S, Yoshida N, et al. *Thin Solid Films* 2003;**430**:253-6.
40. Louis E, Voorma HJ, Koster NB, Bijkerk F, et al. *Microelectronic Eng.* 1995;**27**:235-8.
41. Tsarfati T. PhD thesis; University of Twente; 2009.
42. Louis E, Yakshin AE, Gorts PC, Oestreich S, et al. *Proc. SPIE* 2000;**3997**:406-11.
43. Louis E, Yakshin AE, Tsarfati T, Bijkerk F *Prog. Surf. Sci.* 2011;**86**:255-94.
44. *ASML's 2012 Q2 results.*
45. <http://www.asml.com/asml/show.do?lang=EN&ctx=28904&rid=16712>.
46. *ASML 7th Annual SEMATECH Symposium* 2011.
47. Banine VY, Benschop JPH, Werij HGC *Microelectronic Eng.* 2000;**53**:681-4.
48. Banine VY, Koshelev KN, Swinkels GHM *J. Phys. D: Appl. Phys.* 2011;**44**:253301.
49. Brandt DC, Fomenkov IV, Lercel MJ, La Fontaine BM, et al. *Proc. SPIE* 2012;**8322**:8322-53.
50. Brandt DC, Fomenkov IV, La Fontaine BM, Lercel MJ *Solid State Technol.* 2012;**55**:26-8.

Bibliography

51. Nakamura D, Tamaru K, Akiyama T, Takahashi A, et al. *Appl. Phys. A* 2008;**92**:767-72.
52. Morris O, O'Connor A, Sokell E, Dunne P *Plasma Sources Sci. Technol.* 2010;**19**:025007.
53. Allain JP, Holybee B, List M, Kacic A, et al. *Proc. SPIE* 2011;**8077**:80770I.
54. Allain JP, Nieto-Perez M, Hendricks MR, Zink P, et al. *Appl. Phys. A* 2010;**100**:231-7.
55. Nakamura D, Tamaru K, Hashimoto Y, Okada T, et al. *J. Appl. Phys.* 2007;**102**:123310.
56. Van Der Velden MHL, Brok WJM, Van Der Mullen JJAM, Banine V *J. Appl. Phys.* 2006;**100**:073303.
57. Van Der Velden MHL, Brok WJM, Van Der Mullen JJAM, Goedheer WJ, et al. *Phys. Rev. E* 2006;**73**:036406.
58. Wieggers RC, Goedheer WJ, Akdim MR, Bijkerk F, et al. *J. Appl. Phys.* 2008;**103**:013308.
59. Allain JP, Hassanein A, Allain MMC, Heuser BJ, et al. *Nucl. Instr. Meth. Phys. Res. B.* 2006;**242**:520-2.
60. Nieto M, Allain JP, Titov V, Hendricks MR, et al. *J. Appl. Phys.* 2006;**100**:053510.
61. Chen J, Louis E, Verhoeven J, Harmsen R, et al. *Appl. Surf. Sci.* 2010;**257**:354-61.
62. Heinbuch S, Dong F, Rocca JJ, Bernstein ER *J. Opt. Soc. Am. B* 2008;**25**:B85-B91.
63. Hollenshead J, Klebanoff L *J. Vac. Sci. Technol. B* 2006;**24**:64-82.
64. Koida K, Niibe M *Appl. Surf. Sci.* 2009;**256**:1171-5.
65. Benoit N, Schroder S, Yulin SY, Feigl T, et al. *Appl. Opt.* 2008;**47**:3455-62.
66. Hollenshead J, Klebanoff L *J. Vac. Sci. Technol. B* 2006;**24**:118-30.
67. Nedelcu I, Van De Kruijs RWE, Yakshin AE, Bijkerk F *Phys. Rev. B* 2007;**76**:245404.
68. Nedelcu I, Van De Kruijs RWE, Yakshin AE, Bijkerk F *J. Appl. Phys.* 2008;**103**:083549.
69. Rosen RS, Stearns DG, Viliardos MA, Kassner ME, et al. *Appl. Opt.* 1993;**32**:6975-80.
70. Bruijn S, Van De Kruijs RWE, Yakshin AE, Bijkerk F *Appl. Surf. Sci.* 2011;**257**:2707-11.
71. Bajt S, Chapman HN, Nguyen N, Alameda J, et al. *Proc. SPIE* 2003;**5037 I**:236-48.
72. Over H, He YB, Farkas A, Mellau G, et al. *J. Vac. Sci. Technol. B* 2007;**25**:1123-38.
73. Yan PY, Spiller E, Mirkarimi P *J. Vac. Sci. Technol. B* 2007;**25**:1859-66.

74. Braun S, Mai H, Moss M, Scholz R, et al. *Jpn. J. Appl. Phys.* 2002;**41**:4074-81.
75. Bruijn S, Van De Kruijs RWE, Yakshin AE, Bijkerk F *J. Appl. Phys.* 2012;**111**:064303.
76. Yulin S, Benoit N, Feigl T, Kaiser N *Microelectronic Eng.* 2006;**83**:692-4.
77. Wu SM, Van De Kruijs R, Zoethout E, Bijkerk F *J. Appl. Phys.* 2009;**106**:054902.
78. Bosgra J, Verhoeven J, van de Kruijs RWE, Yakshin AE, et al. *Thin Solid Films* 2012;**522**:228-32.
79. Braginsky OV, Kovalev AS, Lopaev DV, Malykhin EM, et al. *J. Appl. Phys.* 2012;**111**:093304.
80. Graham S, Steinhaus C, Clift M, Klebanoff L *J. Vac. Sci. Technol. B* 2002;**20**:2393-400.
81. van Herpen MMJW, Klunder DJW, Soer WA, Moors R, et al. *Chem. Phys. Lett.* 2010;**484**:197-9.
82. Motai K, Oizumi H, Miyagaki S, Nishiyama I, et al. *Thin Solid Films* 2008;**516**:839-43.
83. Tsarfati T, Zoethout E, van de Kruijs RWE, Bijkerk F *Surf. Sci.* 2009;**603**:2594-9.
84. Kuznetsov AS, van de Kruijs RWE, Gleeson MA, Schmid K, et al. *J. Surf. Investig.- X-ray Synchro.* 2010;**4**:563-6.
85. Kuznetsov AS, Gleeson MA, Bijkerk F *J. Phys.: Condens Matter* 2012;**24**:052203.
86. Kuznetsov AS, Gleeson MA, van de Kruijs RWE, Bijkerk F *Proc. SPIE* 2011;**8077**:807713.
87. Pelizzo MG, Corso AJ, Zuppella P, Windt DL, et al. *Opt. Express* 2011;**19**:14838.
88. Munbodh K, Perez FA, Lederman D *J. Appl. Phys.* 2012;**111**:123919.
89. Frigeri C, Serenyi M, Khanh NQ, Csik A, et al. *Nanoscale Res. Lett.* 2011;**6**:186.
90. Frigeri C, Serényi M, A. C, Erdélyi Z, et al. *J. Mater. Sci. Mater. Electron.* 2008;**19**:S289-S93.
91. Behrisch R *Nucl. Fusion* 1972;**12**:695-713.
92. Milacek LH, Daniels RD, Cooley JA *J. Appl. Phys.* 1968;**39**:2803-15.
93. Primak W, Luthra J *J. Appl. Phys.* 1966;**37**:2287-94.
94. Guseva MI, Martynenko YV *Sov. Phys. Usp.* 1981;**24**:966-1007.
95. Colin J, Coupeau C, Durinck J, Grilhe J *EPL* 2009;**86**:54002.
96. Colin J, Coupeau C, Grilhe J *Phys. Rev. Lett.* 2007;**99**:046101.
97. Cordill MJ, Fischer FD, Rammerstorfer FG, Dehm G *Acta Mater.* 2010;**58**:5520-31.
98. Coupeau C *Thin Solid Films* 2002;**406**:190-4.
99. Coupeau C, Goudeau P, Belliard L, George M, et al. *Thin Solid Films* 2004;**469-470**:221-6.

Bibliography

100. Coupeau C, Grilhe J, Dion E, De Morais LD, et al. *Thin Solid Films* 2010;**518**:5233-6.
101. Crosby KM, Bradley RM *Phys. Rev. E* 1999;**59**:R2542-R5.
102. Condon JB, Schober T *J. Nucl. Mater.* 1993;**207**:1-24.
103. Terreault B *Phys. Status Solidi A* 2007;**204**:2129-84.
104. Bondareva AL, Zmievskaia GI *J. Surf. Investig. - X-ray. Synchro* 2010;**4**:480-7.
105. Demkowicz MJ, Bhattacharyya D, Usov I, Wang YQ, et al. *Appl. Phys. Lett.* 2010;**97**:161903.
106. Hattar K, Demkowicz MJ, Misra A, Robertson IM, et al. *Scripta Mater.* 2008;**58**:541-4.
107. Hochbauer T, Misra A, Hattar K, Hoagland RG *J. Appl. Phys.* 2005;**98**:123516.
108. Rousseau AD, Windt DL, Winter B, Harra L, et al. *Proc. SPIE* 2005;**5900**:1-9.
109. Schlattmann R, Keppel A, Xue Y, Verhoeven J, et al. *J. Appl. Phys.* 1996;**80**:2121-6.
110. Rigato V, Patelli A, Maggioni G, Salmaso G, et al. *Surf. Coat. Technol.* 2003;**174-175**:40-8.
111. Ouyang LZ, Wang H, Chung CY, Ahn JH, et al. *J. Alloy Compd.* 2006;**422**:58-61.
112. Kalisvaart WP, Kubis A, Danaie M, Amirkhiz BS, et al. *Acta Mater.* 2011;**59**:2083-95.
113. Klose F, Rehm C, Nagengast D, Maletta H, et al. *Phys. Rev. Lett.* 1997;**78**:1150-3.
114. Munbodh K, Perez FA, Keenan C, Lederman D, et al. *Phys. Rev. B* 2011;**83**:094432.
115. Kuznetsov AS, Stuijk R, Bijkerk F, Shevelko AP *Plasma Phys. Control. Fusion* 2012;**54**:085019.
116. Hassanein A, Sizyuk T, Sizyuk V, Miloshevsky G *Fusion Eng. Des.* 2010;**85**:1331-5.
117. Linke J, Loewenhoff T, Massaut V, Pintsuk G, et al. *Nucl. Fusion* 2011;**51**:073017.
118. Coenen JW, Philipps V, Brezinsek S, Pintsuk G, et al. *Phys. Scripta* 2011;**2011**:014066.
119. Unterberg B, Jaspers R, Koch R, Massaut V, et al. *Fusion Eng. Des.* 2011;**86**:1797-800.
120. van Rooij GJ *Fusion Sci. Technol.* 2010;**57**:313-20.
121. Zielinski JJ, Al R, van der Meiden H, Melissen W, et al. *J. Nucl. Mater.* 2011;**415**:S70-3.
122. Presnyakov L, Shevelko A *JETP Lett.* 1982;**36**:44-7.
123. Kodama R, Mochizuki T *Opt. Lett.* 1987;**12**:990-2.
124. Mazing MA, Pirogovskiy PY, Shevelko AP, Presnyakov LP *Phys. Rev. B* 1985;**32**:3695-8.

125. Shevelko AP, Knight LV, Peatross JB, Wang Q *Proc. SPIE* 2001;**4505**:171-8.
126. Renner O, Pisarczyk T, Chodukowski T, Kalinowska Z, et al. *Phys. Plasmas* 2011;**18**:093503.
127. de Rooij-Lohmann VITA, Kozhevnikov IV, Peverini L, Ziegler E, et al. *Appl. Surf. Sci.* 2010;**256**:5011-4.
128. Nedelcu I, van de Kruijs RWE, Yakshin AE, Tichelaar F, et al. *Thin Solid Films* 2006;**515**:434-8.
129. Tschersich KG, von Bonin V *J. Appl. Phys.* 1998;**84**:4065-70.
130. Tschersich KG *J. Appl. Phys.* 2000;**87**:2565-73.
131. Schwarz-Selinger T, von Keudell A, Jacob W *J. Vac. Sci. Technol. A* 2000;**18**:995-1001.
132. Graham S, Steinhaus C, Clift M, Klebanoff L, et al. *Proc. SPIE* 2003;**5037 I**:460-9.
133. Arnold Bik WM, Habraken FHPM *Rep. Prog. Phys.* 1993;**56**:859.
134. Benka O. Nuclear Reaction Analysis (NRA). Surface and Thin Film Analysis: A Compendium of Principles, Instrumentation and Applications, Second Edition. Weinheim: Wiley-VCH Verlag GmbH & Co. KGaA; 2011.
135. Alimov VK, Roth J, Lindig S *J. Nucl. Mater.* 2008;**381**:267-70.
136. http://physik2.uni-goettingen.de/research/2_hofs/methods/nra.
137. Fukutani K, Wilde M, Matsumoto M *Phys. Rev. B* 2001;**64**:245411.
138. Reuter W, Baglin JEE *J. Vac. Sci. Technol.* 1981;**18**:282-8.
139. Mayer M Rutherford Backscattering Spectroscopy (RBS). Trieste: Lectures given at the Workshop on Nuclear Data for Science and Technology: Materials Analysis; 2003.
140. Louis E, Yakshin AE, Zoethout E, Van De Kruijs RWE, et al. *Proc. SPIE* 2005;**5900**:1-4.
141. Yakshin AE, Van De Kruijs RWE, Nedelcu I, Zoethout E, et al. *Proc. SPIE* 2007;**6517**:65170I.
142. Van Den Oetelaar LCA, Nooij OW, Oerlemans S, Denier Van Der Gon AW, et al. *J. Phys. Chem. B* 1998;**102**:3445-55.
143. Fukai Y, Mizutani M, Yokota S, Kanazawa M, et al. *J. Alloys Comp.* 2003;**270**:356-7.
144. Landkammer B, Von Keudell A, Jacob W *J. Nucl. Mater.* 1999;**264**:48-55.
145. Yamamura Y, Tawara H *At. Data. Nucl. Data Tables* 1996;**62**:149-253.
146. Giguere A, Terreault B *Surf. Coat. Technol.* 2007;**201**:8205-9.
147. Giguere A, Terreault B *J. Appl. Phys.* 2007;**102**:106106.
148. Tschersich KG, von Bonin V *Journal of Applied Physics* 1998;**84**:4065-70.
149. Giguere A, N D, Terreault B *Appl. Phys. Lett.* 2005;**87**:211911.
150. Goudeau P, George M, Coupeau C *Appl. Phys. Lett.* 2004;**84**:894-6.

Bibliography

151. Lee JK, Lin Y, Jia QX, Hochbauer T, et al. *Appl. Phys. Lett.* 2006;**89**:101901.
152. Usenko AY, Ulyashin AG *Jpn. J. Appl. Phys.* 2002;**41**:5021-3.
153. Chen P, Chu PK, Hochbauer T, Lee JK, et al. *Appl. Phys. Lett.* 2005;**86**:031904.
154. Ma Y, Rob J, Dungen W, Huang YL, et al. *Appl. Phys. Lett.* 2005;**86**:252109.
155. Hutchinson JW, Thoules MD, Liniger EG *Acta Metal. Mater.* 1992;**40**:295-308.
156. Jagla EA *Phys. Rev. B* 2007;**75**:085405.
157. Audoly B *Phys. Rev. Lett.* 1999;**83**:4124-7.
158. Goudeau P, Villain P, Tamura N, Padmore HA *Appl. Phys. Lett.* 2003;**83**:51-3.
159. Peyla P *Phys. Rev. E* 2000;**62**:R1501-R4.
160. Nan L, Martin MS, Anderoglu O, Misra A, et al. *J. Appl. Phys.* 2009;**105**:123522.
161. Zoethout E, Sipos G, Van de Kruijs RWE, Yakshin A, et al. *Proc. SPIE* 2003;**5037**:872.
162. Okada M, Moritani K, Kasai T *Phys. Rev. B* 2005;**71**:033408.
163. Yamakawa K, Ege M, Hirscher M, Ludescher B, et al. *J. Alloy Compd.* 2005;**393**:5-10.
164. Bruel M *Nucl. Instr. Meth. Phys. Res. B.* 1996;**108**:313-9.
165. Celler GK, Cristolovenu S *J. Appl. Phys.* 2003;**93**:4955-78.
166. Lanford WA, Trautvetter HP, Ziegler JF, Keller J *Appl. Phys. Lett.* 1976;**28**:566-8.
167. Trocellier P, Engelmann C *J. Radioanal. Nucl. Chem.* 1986;**100**:117-27.
168. Bruijn S, van de Kruijs RWE, Yakshin AE, Bijkerk F *Def. Diff. Forum* 2009;**283-286**:657-61.
169. Windt DL, Brown WL, Volkert CA, Waskiewicz WK *J. Appl. Phys.* 1995;**78**:2423-30.
170. Schneider JM, Anders A, Hjorvarsson B, Petrov I, et al. *Appl. Phys. Lett.* 1999;**74**:200-2.
171. Schneider JM, Hjorvarsson B, Wang X, Hultman L *Appl. Phys. Lett.* 1999;**75**:3476-8.
172. Schneider JM, Larsson K, Lu J, Olsson E, et al. *Appl. Phys. Lett.* 2002;**80**:1144-6.
173. Yamashita Y, Sakamoto Y, Kamiura Y, Ishiyama T *Jpn. J. Appl. Phys.* 2007;**46**:1622-4.
174. Henley FJ, Brayan MA, En WG, inventors. US patent 6,500,732. 2002.
175. Pitera AJ, Fitzgerald EA *J. Appl. Phys.* 2005;**97**:104511.
176. Fedders PA, Leopold DJ, Chan PH, Borzi R, et al. *Phys. Rev. Lett.* 2000;**85**:401-4.
177. Su YS, Pantelides ST *Phys. Rev. Lett.* 2002;**88**:165503.
178. Abteu TA, Inam F, Drabold DA *Epl* 2007;**79**:36001 (5).

179. Nemanic V, Zajec B, Dellasega D, Passoni M *J. Nucl. Mater.* 2012;**429**:92-8.
180. De Temmerman G, Doerner RP *J. Nucl. Mater.* 2009;**389**:479-83.
181. Griessen R *Phys. Rev. B* 1988;**38**:3690-8.
182. Hjorvarsson B, Ryden J, Karlsson E, Birch J, et al. *Phys. Rev. B* 1991;**43**:6440-5.
183. Hjorvarsson B, Vergnat M, Birch J, Sundgren JE, et al. *Phys. Rev. B* 1994;**50**:11223-6.
184. Miceli PF, Zabel H, Cunningham JE *Phys. Rev. Lett.* 1985;**54**:917-9.
185. Wolff M, Palsson GK, Korelis PT, Dura JA, et al. *J. Phys.: Condens. Matter* 2012;**24**:255306 (6).
186. Freitag JM, Clemens BM *Appl. Phys. Lett.* 1998;**73**:43-5.
187. Mirkarimi PB *Opt. Eng.* 1999;**38**:1246-59.
188. Windt DL *J. Vac. Sci. Technol. A* 2000;**18**:980-91.
189. Bajt S, Stearns DG, Kearney PA *J. Appl. Phys.* 2001;**90**:1017-25.
190. De Rooij-Lohmann VITA, Yakshin AE, Van De Kruijs RWE, Zoethout E, et al. *J. Appl. Phys.* 2010;**108**:014314.
191. Gleiter H *Mater. Trans.* 2003;**44**:1057-67.
192. Kola RR, Windt DL, Waskiewicz WK, Weir BE, et al. *Appl. Phys. Lett.* 1992;**60**:3120-2.
193. Zubarev EN, Kondratenko VV, Pershyn YP, Sevryukova VA *Thin Solid Films* 2011;**520**:314-9.
194. van de Kruijs RWE, Zoethout E, Yakshin AE, Nedelcu I, et al. *Thin Solid Films* 2006;**515**:430-3.
195. Yulin S, Feigl T, Kuhlmann T, Kaiser N, et al. *J. Appl. Phys.* 2002;**92**:1216-20.
196. Pinegyn VI, Zubarev EN, Kondratenko VV, Sevryukova VA, et al. *Thin Solid Films* 2008;**516**:2973-80.
197. Grisolia J, Ben Assyag G, Claverie A, Aspar B, et al. *Appl. Phys. Lett.* 2000;**76**:125606.
198. Romani S, Evans JH *Nucl. Instr. Meth. Phys. Res. B.* 1990;**44**:313-7.
199. Nastasi M, Hochbauer T, Lee J-K, Misra A, et al. *Appl. Phys. Lett.* 2005;**86**:154102-3.
200. Fillon A, Abadias G, Michel A, Jaouen C *Thin Solid Films* 2010;**519**:1655-61.
201. Fillon A, Abadias G, Michel A, Jaouen C, et al. *Phys. Rev. Lett.* 2010;**104**:096101 (4).
202. Braley C, Mazen F, Tauzin A, Rieutord F, et al. *Nucl. Instr. Meth. Phys. Res. B.* 2012;**277**:93-7.
203. Dungen W, Job R, Mueller T, Ma Y, et al. *J. Appl. Phys.* 2006;**100**:124906.
204. Balden M, Lindig, S., Manhard, A., You, J.H. *J. Nucl. Mater.* 2011;**414**:69-72.

Bibliography

205. Bardamid AF, Vukolov KY, Konovalov VG, Naidenkova DI, et al. *Plasma Devices Oper.* 2006;**14**:159-70.
206. Lindig S, Balden M, Alimov VK, Yamanishi T, et al. *Phys. Scripta* 2009;**2009**:014040.
207. Di ZF, Wang, Y.Q., Nastasi., M., Rossi, F., Shao, L., Thompson, P.E. *Appl. Phys. Lett.* 2008;**93**:254104.
208. Ma X, Du, X., Liu, W., Chen, C., Song, Z., Lin, C. *J. Vac. Sci. Technol. B* 2009;**27**:1063-7.
209. Li N, Martin, M.S., Anderouglu, O., Misra, A., Shao, L., Wang., H, Zhang, X. *J. Appl. Phys.* 2009;**105**:123522.
210. Frigeri C, Nasi, L., Serenyi, M., Csik, A., Erdelyi,Z., Beke, D.L. *Superlattice Microst.* 2009;**45**:475-81.
211. Van de Walle CG, Neugebauer J. Hydrogen in semiconductors. Annual Review of Materials Research. Palo Alto: Annual Reviews; 2006. p. 179-98.
212. Chakraborty S, Drabold DA *Phys. Rev. B* 2009;**79**:115214 (8).
213. Hoshihira T, Otsuka T, Tanabe T *J. Nucl. Mater.* 2009;**390-91**:1029-31.
214. Fedders PA *Phys. Rev. B* 2000;**61**:15797-803.
215. Nickel NH, Brendel K *Appl. Phys. Lett.* 2003;**82**:3029-31.
216. Tuttle BR *Mod. Phys. Lett. B* 2005;**19**:683-95.
217. van de Walle CG *Phys. Rev. B* 1994;**49**:4579-85.
218. Kail F, Farjas J, Roura P, Cabarrocas PRI *Phys. Rev. B* 2009;**80**:073202 (4).
219. Borzi R, Fedders PA, Chan PH, Herberg J, et al. *J. Non-Cryst. Solids* 2002;**299**:205-9.
220. Danesh P, Pantchev B, Schmidt B, Grambole D *Jpn. J. Appl. Phys.* 2007;**46**:5050-2.
221. Danesh P, Pantchev B, Schmidt B, Grambole D *Semicond. Sci. Tech.* 2004;**19**:1422-5.
222. Sriraman S, Agarwal S, Aydil ES, Maroudas D *Nature* 2002;**418**:62-5.
223. Sriraman S, Valipa MS, Aydil ES, Maroudas D *J. Appl. Phys.* 2006;**100**:053514
224. Valipa MS, Sriraman S, Aydil ES, Maroudas D *J. Appl. Phys.* 2006;**100**:053515.
225. Sadoh T, Matsuura R, Miyao M, Ninomiya M, et al. *Appl. Phys. Lett.* 2005;**86**:211901.
226. Di ZF, Wang YQ, Nastasi M, Shao L, et al. *Appl. Phys. Lett.* 2008;**93**:104103
227. Andrievski RA *Phys. Usp.* 2007;**50**:691-704.
228. Pundt A *Adv. Eng. Mater.* 2004;**6**:11-21.
229. Gapontsev AV, Kondrat'ev VV *Phys. Usp.* 2003;**46**:1077-98.
230. Kirchheim R, Mütschele T, Kieninger W, Gleiter H, et al. *Mater. Sci. Eng.* 1988;**99**:457-62.
231. Myers SM, Besenbacher F *J. Appl. Phys.* 1986;**60**:3499-507.

232. Bottiger J, Picraux ST, Rud N, Laursen T *J. Appl. Phys.* 1977;**48**:920-6.
233. Nagata S, Tsuchiya B, Ohtsu N, Sugawara T, et al. *J. Nucl. Mater.* 2003;**313**:279-83.
234. Nagata S, Tokunaga K, Tsuchiya B, Ohtsu N, et al. *J. Alloys Comp.* 2003;**356**:326-9.
235. Ohsawa K, Eguchi K, Watanabe H, Yamaguchi M, et al. *Phys. Rev. B* 2012;**85**:094102 (8).
236. Zhou HB, Jin S, Zhang Y, Lu GH, et al. *Phys. Rev. Lett.* 2012;**109**:135502 (5).
237. <http://www.oaresearch.co.uk/oaresearch/tc50/Default.aspx>.
238. Kuznetsov AS, Gleeson MA, Bijkerk F *Submitted to Thin Solid Films*.
239. Hjorvarsson B, Andersson G, Karlsson E *J. Alloys Comp.* 1997;**253**:51-7.
240. Zhou XW, Wadley HNG *J. Appl. Phys.* 2000;**88**:5737-43.
241. Causey RA, Cowgill DF, Doerner R, Kolasinski R, et al. *J. Nucl. Mater* 2011;**415**:S672-S5.
242. Igarashi E, Nishikawa Y, Nakahata T, Yoshikawa A, et al. *J. Nucl. Mater.* 2007;**363-365**:910-4.
243. Lu N, Li J, Wang XX, Wang TC, et al. *Plasma Chem. Plasma P.* 2012;**32**:109-21.
244. Oya Y, Miyauchi H, Suda T, Nishikawa Y, et al. *Fusion Engineering and Design* 2007;**82**:2582-7.
245. Alimov VK, Shu WM, Roth J, Lindig S, et al. *J. Nucl. Mater.* 2011;**417**:572-5.
246. Alimov VK, Tyburska-Puschel B, Lindig S, Hatano Y, et al. *J. Nucl. Mater.* 2012;**420**:519-24.
247. Ferain IP, Byun KY, Colinge CA, Brightup S, et al. *J. Appl.Phys.* 2010;**107**:054315.
248. Hayashi S, Bruno D, Goorsky MS *Appl. Phys. Lett.* 2004;**85**:236-8.
249. Liang JH, Hu CH, Bai CY, Chao DS, et al. *Physica B-Condens. Matter* 2012;**407**:3020-5.
250. Shcherbachev K, Bailey MJ *Phys. Stat. Solid A* 2011;**208**:2576-81.
251. Woo HJ, Choi HW, Hong W, Park JH, et al. *Surf. Coat. Technol.* 2009;**203**:2375-9.
252. Kuznetsov AS, Gleeson MA, Bijkerk F in preparation.
253. Vergnat M, Houssaini S, Marchal G, Mangin P, et al. *Phys. Rev. B* 1993;**47**:7584.
254. Suckewer S, Skinner CH, Kim D, Valeo E, et al. *Phys. Rev. Lett.* 1986;**57**:1004-7.
255. Suckewer S, Skinner CH, Milchberg H, Keane C, et al. *Phys. Rev. Lett.* 1985;**55**:1753-6.
256. de Temmerman G, Zielinski JJ, van der Meiden H, Melissen W, et al. *Appl. Phys. Lett.* 2010;**97**:081502.

Bibliography

257. de Temmerman G, Zielinski JJ, van Diepen S, Marot L, et al. *Nucl. Fusion* 2011;**51**:073008.
258. Umstadter KR, Doerner R, Tynan GR *Nucl. Fusion* 2011;**51**:053014.
259. Allain JP, Nieto M, Hendricks M, Harilal SS, et al. *Proc. SPIE* 2007;**6586**:65860W.
260. Morris O, O'Connor A, Sokell E, Dunne P *Plasma Sources Sci. Technol.* 2010;**19**:025007.
261. Srivastava SN, Thompson KC, Antonsen EL, Qiu H, et al. *J. Appl. Phys.* 2007;**102**:023301.
262. Insepov Z, Allain JP, Hassanein A, Terasawa M *Nucl. Instr. Meth. Phys. Res. B* 2006;**242**:498-502.
263. de Groot B, Al R, Engeln R, Goedheer WJ, et al. *Fusion Eng. Des.* 2007;**82**:1861-5.
264. Rapp J, Koppers WR, Van Eck HJN, Van Rooij GJ, et al. *Fusion Eng. Des.* 2010;**85**:1455-9.
265. Allain JP, Nieto M, Hendricks MR, Plotkin P, et al. *Rev. Sci. Instrum.* 2007;**78**:113105.
266. Federici G, Skinner CH, Brooks JN, Coad JP, et al. *Nucl. Fusion* 2001;**41**:1967-2137.
267. Shevelko AP, Shmaenok LA, Churilov SS, Bastiaensen RKF, et al. *Phys. Scripta* 1998;**57**:276-82.
268. Stuik R, Scholze F, Tummler J, Bijkerk F *Nucl. Instrum. Meth. Phys. Res. A* 2002;**492**:305-16.
269. Fabbro R, Max C, Farbe E *Phys. Fluids* 1985;**28**:1463-81.
270. Shafranov VD *Sov. Phys. JETP* 1957;**5**:1183-8.
271. Zeldovich YB, Raizer YP *Physics of Shock Waves and High-Temperature Hydrodynamic Phenomena*. New York: Academic Press; 1996.
272. Sobelman II, Vainshtein LA, Yukov EA *Excitation of Atoms and Broadening of Spectral Lines*. Berlin: Springer; 1981.
273. Rumsby PT, Paul JWM *Plasma Phys.* 1974;**16**:247-60.
274. Lumma D, Terry JL, Lipschultz B *Phys. Plasmas* 1997;**4**:2555.
275. Loarte A, Saibene G, Sartori R, Riccardo V, et al. *Phys. Scripta* 2007;**2007**:222-8.
276. Bazylev B, Janeschitz G, Landman I, Pestchanyi S, et al. *Fusion Eng. Des.* 2008;**83**:1077-81.
277. <http://www.differ.nl/en/research/nsi/projects>.
278. <http://www.utnieuws.nl/nieuws/partnerschap-ut-en-bedrijfsleven>.
279. van der Velden M *PhD Thesis TU Eindhoven* 2006.
280. Greim O *Phys. Rev. B* 2004;**50**:10664-8.
281. Colin J, Junqua N, Grilhe J *Phyl. Mag. A* 1997;**75**:369-77.
282. van den Boogaard ARJ, Zoethout E, Makhotkin IA, Louis E, et al. *J. Appl. Phys.* 2012;**112**:123502.

283. Feigl T, Yulin S, Perske M, Pauer H, et al. *Proc. SPIE* 2008;**7077**:70771W.
284. Kuznetsov AS, Gleeson MA, van de Kruijs R, Bijkerk F, inventors; Method for producing a reflective optical element for EUV lithography; patent WO 2012/175494 A1. Priority date 22 June 2011.
285. http://www.fom.nl/live/english/research/institutes/energy_research.pag.
286. McDaniel ND, Bernhard S *Dalton Trans.* 2010;**39**:10021-30.
287. Nozik AJ *Nano Lett.* 2010;**10**:2735-41.
288. Ye S, Ouyang L, Zhu M *Rare Metals* 2006;**25**:295-9.
289. Zielinski JJ *PhD Thesis TU Eindhoven* 2013.
290. Sobierajski R, Bruijn S, Khorsand AR, Louis E, et al. *Opt. Express* 2011;**19**:193-205.
291. Makhotkin IA, Zoethout E, Louis E, Yakunin A, et al. *Opt. Express* 2012;**20**:11778-86.
292. Sturm JM, Lee CJ, Bijkerk F *Surf. Sci.*;**612**:42-7.

14. Acknowledgements

These almost five years of hard work would be impossible without help of many people that I would like to mention here.

First of all, I would like to thank my promotor Fred Bijkerk for giving me an opportunity to conduct my PhD research in his group. I kindly acknowledge his comments and suggestions to all of my papers and especially his help in valorizing our scientific results.

I enormously appreciate help of my daily supervisor, Michael Gleeson. He has contributed to all parts of my work, starting from assembling the experimental set-up, conducting the experiments and to proof-reading of my manuscripts and helping answering referees' comments. He has been giving a lot of practical advice regarding living in the Netherlands, that has been also a valuable contribution.

I acknowledge help and scientific discussions with other senior members of nSI group at DIFFER: Andrey, Eric, Robbert - thank you very much! Edwin requires a special acknowledgement for conducting XPS measurements described in chapter 3.

Of course, this research would not be manageable without contribution from our technical staff, either in preparing samples and conducting depositions of multilayers or in fixing problems with the experimental set-up. Arend-Jan, Kees, Peter, Santi, Frenk - your help is highly appreciated!

Chapter 3 would never appear without a contribution from Klaus Schmid of IPP Garching (Germany) in conducting the exposures and performing NRA and RBS measurements. Joachim Roth and Juergen Rapp are kindly acknowledged for making this collaboration possible. Besides that, I would like to mention my old friend Oleg Pronin for his hospitality in Garching (and for our joint trip to the Czech Republic later that year).

Alexander Shevelko and Remko Stuik require special mention for their enormous contribution to Chapter 8 and for introducing me to the world of laser plasma-wall interactions and XUV spectroscopy. Greg de Temmerman, Jakub (Kuba) Zielinski and my old friend Kirill Bystrov from PSI-E group of FOM DIFFER are acknowledged for their contribution to comparison of plasma parameters in laser plasma and tokamaks. Besides, that I would like to thank Greg in general for numerous scientific discussions on plasma-wall interactions - his great knowledge of this subject helped me a lot!

Wim Arnold Bik (former AccTec BV, currently Detect 99) arranged all ion beam-based analysis (ERD, RBS, NRA) for chapters 5,6 and 7. His deep knowledge of all those techniques that he shared with me improved my general knowledge of surface analysis a lot, thank you Wim !

Fellow PhD students, master students and post-docs contributed to making life at DIFFER or outside of it more fun. Some of them I want to thank separately. Kuba and Diego are acknowledged for their great help during moves to Utrecht and Culemborg and just for being good friends. Pim, Sebastian, Marko and

Steven - thanks for all those chats during coffee breaks; Pim also requires additional 'thank you' for his help with my Dutch examination. Kirill - thanks for those nice bike trips ! Also my roommates at DIFFER: Mike, Fujun, Hirokazu and Teo require special mention for creating nice atmosphere in our office. And, of course, thanks to all Russian guys - my old friend Igor, Alexander, Slava and Dima !

Members of the reading committee are acknowledged for their valuable comments and interesting scientific discussions.

Although not being my direct colleagues during my PhD study, people from Zeiss and ASML contributed a lot to my understanding of 'real life' physics questions in industry - thank you very much.

My former colleagues from Russia: Pavel, Arseniy, Yaroslav and Leon Bogdanovich were still supporting me remotely. Thank you for numerous discussions on plasma-wall interaction and hydrogen trapping in materials. My old friends from Russia, Pavel and Denis, - thanks for that nice trip to Prague and Vienna ! My school mate Alexey is acknowledged for visiting me in Utrecht and for being a good friend through all those years. Anna, my university friend, - thanks for all those outings in Utrecht and for becoming a friend not only for me but also for Masha. My brother Dmitry is acknowledged for his visits, I think without him we probably would never see all those touristic places like Keukenhof or Kinderdijk...

I would like to thank my parents for all their help during preparations of my move to the Netherlands and for their constant support.

My biggest thank you goes to Masha. Thank you for your love and care ! She has been always there to encourage me when things were going wrong and happy for me when they were going great. She has been always creative in how to spend our free time to relax from all those days of hard work. She introduced me to the world of mountain hiking and travelling and I realized how much fun it is. I appreciate her understanding for 'another evening/weekend staying at home to finish the thesis'. Although she works in a totally different field, she could always contribute to understanding of any questions from my research. She helped me a lot with editing of the thesis, especially with pictures of processes of blister formation. I would never manage to accomplish this work without you ! Я тебя очень сильно люблю, солнышко !

15. Curriculum vitae.

Alexey Kuznetsov was born in Moscow, Russia on 23rd of August, 1985. In 2002 he graduated (with honors) from Gymnasium 1526 in Moscow. He then studied Plasma Physics and Plasma-Wall Interactions in National Research Nuclear University 'MEPhI' (Moscow), his graduating research project was done at group of Prof. Dr. L.B. Begrambekov on peculiarities of hydrogen trapping in carbon films. He graduated in 2008 with a cum laude diploma and one referred journal paper was published as a result of this work.

From 1st October 2008 to 1st October 2012 he was a PhD student in nSI group of FOM Institute DIFFER, mainly studying hydrogen interactions with multilayered structures. This research resulted in several refereed articles, one article in conference proceedings, several contributions to conferences and workshops and one patent.

From 1st October 2012 Alexey Kuznetsov is working at ASML in Chemical Contamination Control and Materials group.